2011

Multicomponent drop vaporization modeling of petroleum and biofuel mixtures

Lei Zhang
Iowa State University

Multicomponent drop vaporization modeling of petroleum and biofuel mixtures

by

Lei Zhang

A dissertation submitted to the graduate faculty
in partial fulfillment of the requirements for the degree of
DOCTOR OF PHILOSOPHY

Major: Mechanical Engineering

Program of Study Committee:
Song-Charng Kong, Major Professor
Xinwei Wang
Song Zhang
Baskar Ganapathysubramanian
James C. Hill

Iowa State University
Ames, Iowa
2011

TABLE OF CONTENTS

LIST OF TABLES

LIST OF FIGURES

ACKNOWLEDGEMENT

First and foremost I want to thank my advisor Dr. Song-Charng Kong. Four years ago, he gave me an opportunity to come to Iowa State and pursue a Ph. D. in his engine research group. During these years, with his enthusiasm, patience, and great efforts, he has been giving me instruction in improving my abilities in scientific research, knowledge in Internal Combustion Engines, and skills in technical writing. I appreciate his contribution in time, idea, funding, computational resources, and research environment to make my Ph. D. experience productive.

I also would like to thank the current and past members of the engine research group. The group has been the place where I received precious friendship, advice, and collaboration. Especially Dr. Yuanhong Li, who is like an older brother, gave me great help in both my research and life.

During the four years in Iowa State, the high quality courses in the college of engineering greatly improved my fundamental knowledge and facilitated my research in engine area. The memorable courses include Fluid Mechanics by Dr. Michael Olsen, CFD II by Dr. Richard Pletcher, Transport Phenomena by Dr. Kurt Hebert, Turbulence by Dr. Paul Durbin, Advanced CFD by Dr. Zhijian Wang, Convection Heat Transfer by Dr. Terry Meyer, etc. I appreciate the kind instruction by the above professors in the course contents.

For this dissertation, I would like to thank my committee members including Dr. Xinwei Wang, Dr. Baskar Ganapathysubramanian, Dr. Song Zhang, and Dr. James Hill for their time and helpful comments.

Finally, I would like to thank my parents and both of my older sisters for their love, support, and encouragement. My parents gave me all they have to be supportive in my 22-year school life. In the past four years, they have been waiting in my home country and expecting me to come back with a doctoral degree. In the past years, my sisters took my responsibility to take care of my parents and let me be able to put all of my energy and attention in my research.

ABSTRACT

Drop vaporization modeling is an important stage in spray combustion simulation. To improve the overall accuracy of multidimensional engine simulation, drop vaporization models based on multicomponent strategies was developed in this study. Petroleum fuels such as diesel fuel and gasoline are the major engine fuels composed of hundreds of hydrocarbon species. Therefore, a multicomponent model based on continuous thermodynamics (CT) was used for the vaporization modeling of petroleum fuels. Using the model, the molecular weights of petroleum fuel components is described by a gamma distribution, which is a probability distribution function. The model was applied in the vaporization simulation of single petroleum fuel drops. Results show a continuous shift in the molecular weight distribution and an increase in the mean molecular weight of the drop during the vaporization process, indicating that lighter components in the liquid drop vaporize earlier. The model was validated by simulating the diesel spray combustion in a constant volume combustion chamber, and good levels of agreement with experimental results were obtained in both flame structures and soot distributions.

The application of biofuels such as biodiesel and ethanol in engines has become increasingly important for reasons of environmental sustainability. Therefore, another emphasis of the present study is on the vaporization modeling of biofuels under engine operating conditions. Since biodiesel compositions are not universal due to the uncertainty in feedstock, biodiesel vaporization (BV) model and a discrete component (DC) approach based on its five dominant fatty acid components were developed for the fuel. Methods of predicting the critical and physical properties of biodiesel components were presented. Experimentally measured vaporization results of biodiesel were used to demonstrate the validity of the vaporization models. Moreover, biofuels are often used in engines by blending with petroleum fuels, and the detailed understanding of the vaporization process is essential to designing a clean and efficient combustion system. In the present study, a hybrid drop vaporization model was developed, i.e., continuous thermodynamics is used to describe the distribution of petroleum fuel components, and a

discrete component approach was used to model biofuels. Practical fuel blends including those of diesel-biodiesel and gasoline-ethanol were studied.

Bio-oil is a bio-renewable fuel produced by fast pyrolysis of biomass and has complex composition due to the uncertainties in feedstock. The present study is further focused on the multicomponent vaporization modeling of bio-oil based on its major components selected from previous studies. A discrete component approach was developed and the physical properties of bio-oil major components were predicted. Results show a continuous variation of drop composition and indicate that levoglucosan survives other fuel components and dominates the late stage of the vaporization process. Vaporization behaviors of the mixtures of bio-oil and other practical fuels were also studied, and results show the much longer lifetime of bio-oil components than other fuels.

In addition to the consideration of fuel components, drop vaporization modeling under high-pressure conditions is also emphasized in this study. Traditional vaporization models are based on the Raoult's law, which is a phase equilibrium only true at low-pressure conditions. However, in engine operating conditions, liquid fuel drops vaporize in high-pressure environments. To extend the multicomponent vaporization models to high-pressure conditions, continuous thermodynamics was coupled general phase equilibrium which is characterized by the equality of the fugacity of each component in both phases. Correlations were developed to relate the parameters of Peng-Robinson equation of state and fugacity coefficients with molecular weight. Equations to calculate the molecular weight distribution in the vapor phase were also derived. The high-pressure vaporization model was validated using the experimental data of n-heptane drops under different ambient temperatures and pressures. Good levels of agreement between the predicted and measured drop vaporization histories were obtained. The high-pressure model was used to predict the diesel-biodiesel drop vaporization in diesel engine conditions. Results show that the drop lifetime increases with the biodiesel volume fraction in the fuel blend. Only the lighter components of diesel fuel vaporize at the beginning, and biodiesel components do not vaporize until sometime in the vaporization process. This phenomenon was further confirmed by the predicted distributions of both fuel vapors resulting from a biodiesel-diesel spray.

CHAPTER 1 INTRODUCTION

1.1 Background

Research on internal combustion (IC) engines can be classified into two categories, namely, numerical simulation and experiments. The development in computational fluid dynamics (CFD) in recent years has greatly improved the accuracy of the multidimensional engine simulation. Compared to engine experiments, multidimensional engine simulation is capable of providing detailed insights into the in-cylinder dynamics, which involves a number of complex, closely coupled physical and chemical processes. In particular, the spray and combustion processes are of great significance due to their impact on engine performance and emissions. Spray is a process characterized by fuel injection, atomization, drop collision, drop coalescence, and drop vaporization. Combustion is a process releasing the chemical energy of the fuel and is preceded by the mixing of air and fuel vapor resulting from liquid fuel drop vaporization. In multidimensional engine simulation, the detailed fuel spray and combustion processes are simulated using various numerical models. The overall accuracy of engine simulation strongly relies on the modeling of both processes. As engine simulation is required for more accurately representing engine in-cylinder dynamics and providing guide to improve engine performance, more detailed modeling strategies about spray and combustion are needed.

Drop vaporization is a crucial process connecting the spray dynamics and combustion chemistry of fuels. It determines the distribution of fuel vapor in an engine cylinder and the local air-fuel ratio, an important indicator of the combustion behavior. However, traditionally, the treatment on vaporization modeling in multidimensional engine simulation is not comprehensive. Simple vaporization models were usually used without considering the actual composition of the fuel and the realistic ambient conditions. Thus, to improve the accuracy of multidimensional engine simulation, one essential step is to develop more advanced models for drop vaporization. There are mainly two aspects of improvements that can be pursued. One aspect is to extend the applicability of the models to consider the effects of fuel components. The other aspect is to enhance the model accuracy by taking the high-

pressure effect into account. The advanced models also need to be computationally efficient to avoid adding additional cost to the engine simulation.

Even though fossil fuels are the primary energy source for most of the combustion devices, there have been concerns about the future availability and environmental impact of such fuels. For a long-term sustainability, the application of renewable fuels in traditional combustion devices needs to be investigated to replace fossil fuels. In engines, bio-renewable fuels such as biodiesel, ethanol, bio-oil, etc. have been demonstrated as the promising replacements of the nonrenewable petroleum fuels. Due to the close chemical and physical properties with diesel fuel, biodiesel, which can be produced from animal fat or vegetable oil, has been used to replace diesel fuel in diesel engines. Similarly, ethanol can be used to replace gasoline in spark-ignition engines. In practice, to achieve the optimum emission level and performance, bio-renewable fuels are blended with petroleum fuels at different ratios in engine applications. Therefore, the special characteristics of diesel-biodiesel mixtures, e.g., B20, and gasoline-ethanol mixtures, e.g., E85, compared to petroleum fuels have been especially emphasized. To study the performance of engines fueled with petroleum-biofuel blends, the vaporization characteristics of such fuel blends are of primary interest. In engine simulation, a comprehensive model, which is able to simulate the vaporization of petroleum-biofuel blends and provide the distributions of both fuel vapors in the engine cylinder, needs to be developed.

Another emerging bio-renewable fuel applicable in engines is bio-oil, which is produced by the fast pyrolysis of biomass usually in the form of cellulose, hemicellulose, and lignin. The feedstock of biomass includes various kinds of biological products such as wood or corn. Different from the gasification process that converts biomass to syngas, fast pyrolysis converts biomass into liquid fuels in the absence of oxygen. Due to its poor quality, which is characterized by high viscosity, coking, solid content, water content, and corrosiveness, bio-oil has only been used in large scale as the energy source of low-efficiency combustion devices such as boiler and furnace. Recent technologies have been developed to convert bio-oil to transportation fuels by improving the quality of the fuel and make it applicable in other high-efficiency combustion devices such as gas turbine and engine. Even though experimental studies have been conducted on the performance of engines fueled with bio-oil,

there have not been studies on the numerical modeling of bio-oil vaporization and combustion in engines. The difficulties involved in the modeling of bio-oil are introduced by the complex composition of the fuel due to the uncertainties in feedstock and pyrolysis processes. Especially for the drop vaporization simulation, which is a crucial step in spray and combustion modeling, reliable models considering the effect of the complex composition of bio-oil are not available.

1.2 Motivation and Objective

One major difficulty involved in drop vaporization modeling is that the compositions of practical fuels can be very complicated. For example, petroleum fuels are composed of 200~300 different hydrocarbon species. Traditionally, single-component vaporization models, which treat the fuel as a pure component without considering the real composition of the fuel, are commonly used. A pure component is usually selected according to the requirement that its physical and chemical properties are close to those of the practical fuel. For instance, tetradecane ($C_{14}H_{30}$) is used to represent diesel fuel, and iso-octane (i-C_8H_{18}) is used to stand for gasoline. By using the single-component model, the composition of the fuel remains unchanged during the vaporization process and has no effect on the vaporization behaviors (e.g., drop lifetime and vapor distribution). Such a simple treatment may lead to significant errors in vaporization modeling and affect the accuracy in combustion simulation. Thus, the first objective of the present work is to develop multicomponent vaporization models that consider the effect of fuel composition on its vaporization behavior. Depending on the compositions of the practical fuels, different kinds of modeling strategies are used. For petroleum fuels, which are composed of hundreds of components, an approach based on continuous thermodynamics needs to be used. For a multicomponent fuel composed of only a few components, discrete component approach is preferred.

Due to the increasing importance of biodiesel applications in diesel engines, the vaporization behavior of biodiesel in engine environment is of great interest and instructive for developing optimal injection strategies to improve engine performance. Therefore, to perform a combustion simulation of engines fueled with biodiesel, a multicomponent vaporization model for biodiesel needs to be developed. Since biodiesel is mainly composed

of a few methyl esters, one of the objectives of the present study is to develop a drop vaporization model for biodiesel using a discrete component approach considering the major components and predict the vaporization behavior of the fuel under engine environments. Moreover, bio-renewable fuels such as biodiesel and ethanol are blended with traditional petroleum fuels for use in engines. Both fuels in the blends vaporize at different rates because of the difference in volatility. The difference in vaporization rates leads to a continuous variation in the fuel composition. Thus, a vaporization model that is applicable for such fuel blends at different blending ratios is also needed. The vaporization model needs to be formulated in a hybrid way such that continuous thermodynamics is used to model petroleum fuels in the fuel blend and discrete component approach is used to model biodiesel.

Moreover, according to the introduction in the last section, bio-oil is an emerging biofuel that can be used in many combustion devices and gasification reactors. This bio-renewable fuel has become increasingly important since its capability to replace petroleum fuels and offset carbon dioxide emissions. Therefore, one of the objectives of the present study is to investigate the vaporization and gasification characteristics of bio-oil. However, due to the uncertainties in feedstock and the pyrolysis process, the composition of bio-oil can be very complex. To develop vaporization models for bio-oil, there are several essential steps, including investigating the compositions of bio-oil derived from various sources, identifying a group of its major components, and developing a vaporization model according to the discrete component approach based on its major components. Using the discrete component approach, the vaporization behavior of bio-oil will be numerically studied and the vapor distribution of its major components in the gas phase will be presented.

Finally, in addition to the concern on the multicomponent fuel composition, drop vaporization modeling with the consideration of the high-pressure effect is also important for improving engine simulation accuracy. In engine cylinders, liquid fuel drops experience high-pressure and high-temperature conditions during the vaporization process. Traditional vaporization models use Raoult’s law, which is based on the assumptions of low-pressure and ideal ambient gas, to describe the relation between the compositions of both phases at the phase interface. However, in engine conditions, such assumptions are not valid due to the high in-cylinder pressure. Using Raoult’s law at high-pressure conditions will wrongly

predict the drop lifetime and lead to unreasonable vapor distributions. Therefore, another objective of the present study is to develop vaporization models that are applicable under high-pressure conditions by implementing general phase equilibrium to replace Raoult's law. In the present study, the improvement of the model to high-pressure conditions needs to be done for the continuous thermodynamics vaporization model by considering the equilibrium of each individual component in both liquid and vapor phases.

CHAPTER 2 LITERATURE REVIEW

In the multidimensional simulation of internal combustion (IC) engines, the modeling of spray and combustion of the liquid fuel is one of the most crucial topics. Especially, in the numerical simulation of drop vaporization, there are numerous aspects, including hydrodynamics, heat transfer, and the effect of fuel components. In this study, the effect of fuel components is especially emphasized. Traditionally, single-component approach is used to model vaporization for any fuels. However, the idea of multicomponent vaporization modeling should be implemented into engine simulation, since practical fuels often have complex compositions. Depending on the composition of the multicomponent fuel, continuous thermodynamics and discrete component approaches are the major methods in the vaporization modeling of multicomponent fuels. Moreover, drop vaporization under high-pressure or supercritical conditions is another major field of study. To extend the vaporization model to high-pressure conditions, a significant improvement is to replace the Raoult's Law with the general phase equilibrium. In addition, the application of biorenewable fuel in IC engines is becoming important due to the questionable future availability of petroleum fuels. Therefore, the vaporization of biorenewable fuels including biodiesel, ethanol, and bio-oil is also of primary interest in this study. In this chapter, literature and fundamental equations involved in drop vaporization modeling will be reviewed.

2.1 Fundamental Equations

In vaporization modeling, a fuel drop is usually assumed to be purely spherical, or in other words, drop deformation is not considered. Figure 2.1 provides the schematic of a vaporizing drop without natural or forced convection from the ambient gas (Hsieh and Shuen, 1991). In this case, the only motion in the vapor phase is induced by vaporization which introduces a flow in the radial direction. The mass/mole fraction of each component in the multicomponent fuel and temperature are functions of the distance in the radial direction only. Therefore, heat and mass transfer also only happen in the radial direction. It can be seen from this figure that the temperature across the liquid-vapor interface is continuous, while

mass/mole fractions show a jump across at the drop surface. The jump is determined by the vapor-liquid phase equilibrium and will be discussed in later chapters.

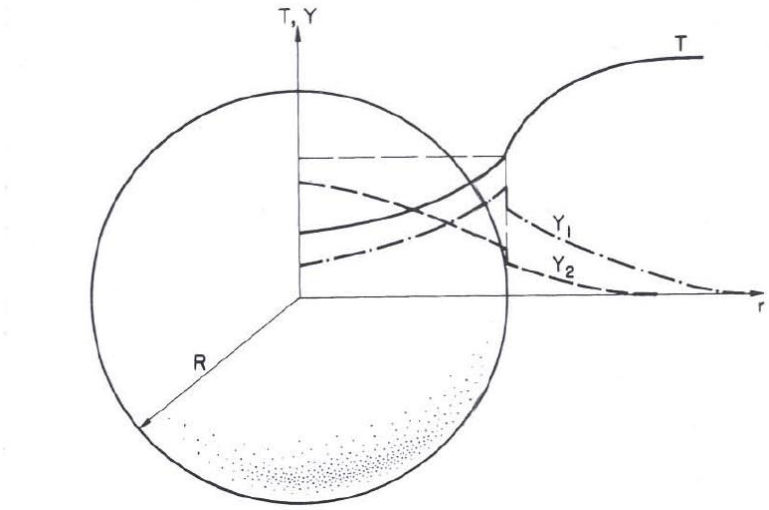

Figure 2.1 Schematic of a vaporizing multicomponent drop

The gas phase ($r>R(t)$) governing equations regarding mass, species, momentum, and energy according to the simplifications discussed above can be expressed in spherical coordinate as

mass

$$\frac{\partial\left(\rho r^2\right)}{\partial t}+\frac{\partial}{\partial r}\left(\rho r^2 v_r\right)=0, \tag{2.1}$$

species

$$\frac{\partial\left(\rho r^2 y_i\right)}{\partial t}+\frac{\partial}{\partial r}\left(\rho r^2 v_r y_i\right)=-\frac{\partial\left(r^2 j_i\right)}{\partial r}, \tag{2.2}$$

momentum

$$\frac{\partial\left(\rho r^2 v_r\right)}{\partial t}+\frac{\partial}{\partial r}\left(\rho r^2 v_r^2\right)=\frac{\partial}{\partial r}\left(r^2\left(-p+\tau_{rr}\right)\right), \tag{2.3}$$

and energy

$$\frac{\partial\left(\rho r^2 T\right)}{\partial t}+\frac{\partial\left(\rho r^2 v_r T\right)}{\partial r}=\frac{1}{c_p}\frac{\partial}{\partial r}\left(kr^2\frac{\partial T}{\partial r}+\rho\sum_{i=1}^{N}h_i j_i\right)+\frac{v_r r^2}{c_p}\frac{\partial p}{\partial r}. \tag{2.4}$$

In the above equations, viscous dissipation, thermal diffusion of species, and body force are neglected. v_r is the mass-averaged velocity in the radial direction induced by vaporization. y_i is the mole fraction of species i in the vapor phase. $j_{i,r}$ is the multicomponent diffusion flux in the radial direction defined by

$$j_i=-\sum_{k=1}^{n-1}\rho D_{ik}\frac{\partial y_i}{\partial r}, \tag{2.5}$$

where D_{ik} is the multicomponent diffusion coefficient between species i and k in a multicomponent system and is different from the binary diffusion coefficients. For a ternary system, the values of the diffusion coefficients can be calculated using the known binary diffusion coefficients as shown in Table 2.1 (Cussler, 1997).

Table 2.1 Diffusion coefficients for a ternary system with known binary values

$$D_{11}=\frac{\frac{y_1}{D_{b12}}+\frac{y_2+y_3}{D_{b23}}}{\frac{y_1}{D_{b12}D_{b13}}+\frac{y_2}{D_{b12}D_{b23}}+\frac{y_3}{D_{b13}D_{b23}}} \qquad D_{12}=\frac{y_1\left(\frac{1}{D_{b13}}-\frac{1}{D_{b12}}\right)}{\frac{y_1}{D_{b12}D_{b13}}+\frac{y_2}{D_{b12}D_{b23}}+\frac{y_3}{D_{b13}D_{b23}}}$$

$$D_{21}=\frac{y_2\left(\frac{1}{D_{b23}}-\frac{1}{D_{b12}}\right)}{\frac{y_1}{D_{b12}D_{b13}}+\frac{y_2}{D_{b12}D_{b23}}+\frac{y_3}{D_{b13}D_{b23}}} \qquad D_{22}=\frac{\frac{y_1+y_3}{D_{b13}}+\frac{y_2}{D_{b12}}}{\frac{y_1}{D_{b12}D_{b13}}+\frac{y_2}{D_{b12}D_{b23}}+\frac{y_3}{D_{b13}D_{b23}}}$$

For drop vaporization calculation, since the mass/mole fractions of the fuel components in the vapor phase are usually small, the multicomponent diffusion flux can be simplified to the binary diffusion flux between the vapor of a fuel component and ambient gas. The binary diffusion can be described using the Fick's law as

$$j_i=-\rho D_{12}\frac{\partial y_i}{\partial r}. \tag{2.6}$$

D_{12} is the binary diffusion coefficient between the fuel vapor and ambient air. τ_{rr} in Eq. (2.3) is the shear stress defined as

$$\tau_{rr} = \frac{4\mu}{3}\left(\frac{\partial v_r}{\partial r} - \frac{v_r}{r}\right). \tag{2.7}$$

On the other hand, in the liquid phase, since the bulk motion can be neglected, the governing equations can be greatly simplified to

species

$$\frac{\partial\left(\rho r^2 x_i\right)}{\partial t} = -\frac{\partial\left(r^2 j_i\right)}{\partial r}, \tag{2.8}$$

and energy

$$\frac{\partial\left(\rho r^2 T\right)}{\partial t} = \frac{1}{c_p}\frac{\partial}{\partial r}\left(kr^2\frac{\partial T}{\partial r} + \sum_{i=1}^{N} h_i j_i\right). \tag{2.9}$$

x_i is the mass fraction of component i in the liquid phase. Under low pressure conditions, the species equations in both phases can be related by the boundary conditions at the phase interface, where the phase equilibrium described by Raoult's law holds. Using Raoult's law, the mole fractions of a component in both phases at interface can be related as

$$Y_i = X_i\frac{P_{vi}\left(T_s\right)}{P}. \tag{2.10}$$

In the above equation, X_i and Y_i are the mole fractions and can be converted to mass fractions to be in consistence with the species equation. P_{vi} is the vapor pressure at the drop surface evaluated at T_s, and P is the pressure of the ambience at the drop surface. In the liquid phase, boundary conditions of the species equation can be obtained at the drop center and drop surface. At the drop center, considering the assumptions of purely spherical shape of the drop and no forced or natural convection, symmetry requires

$$\frac{\partial x_i}{\partial r} = 0. \tag{2.11}$$

At the liquid-vapor phase interface (r=R), mass conservation requires

$$\dot{m}_i'' = \dot{m}'' x_i + j_{i,l} = \dot{m}'' y_i + j_{i,v} . \tag{2.12}$$

with the vaporization mass flux ($\dot{m}''$) defined as

$$\dot{m}'' = \rho_l \dot{R} . \tag{2.13}$$

In Eq. (2.12), subscripts *l* and *v* denote the liquid and vapor phases, respectively. This equation indicates that mass transfer flux is composed of bulk motion and mass diffusion and the total mass transfer fluxes in both phases are equal at the interface. Similarly, the boundary conditions for the energy equation can also be obtained at the drop center and phase interface. At the drop center (r=0), symmetry also requires

$$\frac{\partial T}{\partial r} = 0 . \tag{2.14}$$

At phase interface (r=R), the temperature is continuous, i.e.,

$$T\big|_{r=R-0} = T\big|_{r=R+0} . \tag{2.15}$$

The heat transfer fluxes at the interface in both phases are equal, i.e.,

$$-k_l \left.\frac{\partial T}{\partial r}\right|_{r=R-0} = -k_v \left.\frac{\partial T}{\partial r}\right|_{r=R+0} . \tag{2.16}$$

2.2 Solution of the Governing Equations

To develop practical drop vaporization models, the above vapor phase governing equations can be simplified by performing a pseudo-steady analysis. The simplification can be justified by the relatively short vapor phase characteristic diffusion time (t^*=R^2/D) compared to that of the liquid phase. This usually requires that the ratio of vapor density to gas density is as least an order of magnitude smaller than unity (Tong and Sirignano, 1986). A pseudo-steady solution of the vapor phase species conservation equation (Eq. (2.2)) can be obtained by removing transient term, i.e.,

$$\rho v_r y_i - \rho D_{ig} \frac{\partial y_i}{\partial r} = \frac{\dot{m}_i}{4\pi r^2} . \tag{2.17}$$

D_{ig} is the binary diffusivity between fuel component *i* and ambient gas. $\dot{m}_i$ is the vaporization rate of component *i* and is constant in the radial direction. Define the fraction of vaporization rate ε_i as the ratio of the vaporization rate to the total vaporization rate as

$$\varepsilon_i = \frac{\dot{m}_i}{\dot{m}_{tot}}. \tag{2.18}$$

It is obvious that the summation of the vaporization rate fraction over all of the components is equal to unity, namely,

$$\sum_{i=1}^{n} \varepsilon_i = 1. \tag{2.19}$$

Using the definition of vaporization rate fraction, Eq. (2.17) can be rewritten as

$$y_i \frac{\dot{m}_{tot}}{4\pi r^2} - D_{ig}\rho \frac{dy_i}{dr} = \frac{\dot{m}_{tot}}{4\pi r^2}\varepsilon_i. \tag{2.20}$$

According to the assumption of pseudo-steady and considering the mass conservation of each component in the vapor phase, ε_i is constant along the radial direction. Assuming constant diffusivity and density, a solution of the above equation determining the vaporization rate of each component can be obtained by integrating Eq, (2.20) for *r* from the drop surface (*r*=*R*) to infinity (∞) as

$$\dot{m}_i = 4\pi R\rho\varepsilon_i D_{ig} \ln\left(1 + B_{M,i}\right), \tag{2.21}$$

where B_M is the Spalding mass transfer number defined as

$$B_{M,i} = \frac{y_{i,s} - y_{i,\infty}}{\varepsilon_i - y_{i,s}}. \tag{2.22}$$

Subscript *s* denotes the surface of the drop. From the above two equations, it can be seen that the drop vaporization rate is only determined by the fuel vapor mass fractions at drop surface and the infinite location. The equation of vaporization rate in Eq. (2.21) is computationally efficient and has been widely used in CFD applications.

On the other hand, in the liquid phase, the fully transient species and energy equations are solved. Using the vaporization rate expression (Eq. (2.21)) as the boundary condition in

Eq. (2.12), the analytical solution of the species concentration equation Eq. ((2.8)) for a binary component mixture can be written into the following form (Brenn, 2005):

$$x_i(\tau,\xi)=\sum_j(1+\alpha\tau)^{-\lambda_j}c_j\cdot M\left(\lambda_j,\frac{3}{2},-\frac{\alpha}{4G}\xi^2\right). \tag{2.23}$$

In the above equation, $\tau=t/t_1$ is the non-dimensional time defined by the time t divided by a characteristic drop life time t_1 defined by Brenn (2005). $\xi=r/R$ is the non-dimensional time and radial distance from the drop center. α, G, c_j, λ_j, and d_n are constants. M is Kummer's function defined as

$$M(a,b,x)=1+\frac{a}{b}x+\frac{a(a+1)}{b(b+1)}\frac{x^2}{2!}+\frac{a(a+1)(a+2)}{b(b+1)(b+3)}\frac{x^3}{3!}+\cdots. \tag{2.24}$$

Using the above equation, it can be seen that Eq. (2.23) can be written into the following form:

$$x_i(\tau,\xi)=\sum_j c_j\cdot(1+\alpha\tau)^{-\lambda_j}\cdot\left(1-\frac{\lambda_j\alpha}{6G}\xi^2\right)+O(\xi^4). \tag{2.25}$$

Consequently, the distribution of mass fraction in the liquid phase can be simplified to be a quadratic function of the radial distance from the drop center with fourth order accuracy. In a similar way, for the energy equation (Eq. (2.9)), Cooper (1977) obtained the analytical solution of the temperature field in the liquid phase, and the solution can also be written as a quadratic function of the distance from drop center with fourth order accuracy. The above solutions of species and energy equations suggest that the temperature and concentration in the liquid phase can be assumed to be quadratically related to the radial distance with enough accuracy. Consequently, in this study, in dealing with the cases that liquid drop is blended by two different fuels, the mass fraction of each liquid fuel in the mixture will be assumed to be quadratic functions of the distance from the drop center.

2.3 Convectional Heat and Mass Transfer

The equations of vaporization rate derived in the above section are based on the assumption of no forced or natural convection. Therefore, heat and mass transfers only in the radial direction are considered. However, in most of the situations, there is always relative

motion between drops and ambient gas, and the effect of convection on drop vaporization rate needs to be considered. To estimate the convective heating rate from the ambience to a drop, consider the following pseudo-steady energy conservation equation in the vapor phase:

$$4\pi r^2 k_g \frac{dT}{dr} = \dot{m}_{tot} c_{pv} \left(T - T_s\right) + \dot{m}_{tot} L\left(T_s\right) + \dot{q}_d \,. \tag{2.26}$$

In the above equation, c_{pv} is the mass averaged specific heat of the fuel vapor, and k_g is gas phase thermal conductivity. The left hand side of the above equation accounts for the heat conduction toward the drop. On the right hand side, the first term is the amount of heat used for heating the fuel vapor from drop surface temperature to the ambient temperature. The second term accounts for the amount of heat used for vaporization latent heat. The last term is the drop heating rate, which can be related with the variation rate of drop temperature as

$$\dot{q}_d = \frac{4}{3}\pi R^3 \rho_L c_v \frac{dT_d}{dt} \,. \tag{2.27}$$

Eq. (2.26) shows that the amount heat conducted toward the drop will be used for heating up the vapor, overcoming vaporization latent heat, and increasing drop temperature.

By integrating Eq. (2.26) from the drop surface (r=R) to infinity (∞), an alternative expression for the drop vaporization rate can be obtained as

$$\dot{m}_{tot} = \frac{4\pi R k_g}{c_{pv}} \ln\left(1 + B_T\right). \tag{2.28}$$

B_T in the above equation is the Spalding heat transfer number defined by

$$B_T = \frac{c_{pv}\left(T_g - T_s\right)}{L\left(T_s\right) + \dot{q}_d / \dot{m}_{tot}} \,. \tag{2.29}$$

Eq. (2.28) and Eq. (2.21) are two equivalent ways in calculating the drop vaporization rate. Thus, the heat transfer number (B_T) can be related to the mass transfer number (B_M) as

$$1 + B_T = \left(1 + B_M\right)^{\varphi}, \tag{2.30}$$

where φ is defined by

$$\varphi = \frac{c_{pv}}{c_{pg}} \frac{1}{Le} . \tag{2.31}$$

c_{pg} is the specific heat of the ambient gas. *Le* in the above equation is the Lewis number, which is defined as

$$Le = \frac{k_g}{c_{pg} \rho D_{i,g}} . \tag{2.32}$$

According to the energy conservation equation Eq. (2.26) at $r=R$, the amount of heat transferred to the liquid drop surface is the summation of the last two terms, i.e.,

$$\dot{q}_s = \dot{m}_{tot} L + \dot{q}_d . \tag{2.33}$$

On the other hand, if the drop is not vaporizing, the amount of heat transfer to the drop surface can be calculated with the convection heat transfer coefficient, which can be obtained according to the definition of Nusselt number. For non-convection situations, Nusselt number is equal to 2. Thus, the amount of heat transferred to drop surface without vaporization can be expressed as

$$\dot{q}_{s,non-vap} = 4\pi R^2 \frac{k_g}{R} \left(T_g - T_s \right) . \tag{2.34}$$

Using Eqs. (2.28) and (2.29), the amount of heat transferred to the drop surface with or without vaporization can be related by

$$\dot{q}_s = \dot{q}_{s,non-vap} \frac{z}{e^z - 1} , \tag{2.35}$$

where *z* is defined as

$$z = \frac{\dot{m}_{tot} c_{pv}}{4\pi k_g R} . \tag{2.36}$$

Eq. (2.35) provides the difference of the heat transfer rate to the drop surface between a vaporizing drop and a non-vaporizing drop. The difference is due to the amount heat used for heating up the vapor. Therefore, this relation implies that for the situations with forced

convection the Nusselt number for a vaporizing drop can be related to the Nusselt number for a non-vaporizing drop as

$$Nu = Nu_\circ \frac{z}{e^z - 1} = Nu_\circ \frac{\ln\left(1 + B_T\right)}{B_T}. \tag{2.37}$$

$Nu_\circ$ is the Nusselt number for a non-vaporizing drop, and there are correlations available for $Nu_\circ$ under different situations. In this study, the following classical correlation is used:

$$Nu_\circ = 2 + 0.6 Re^{1/2} Pr^{1/3}. \tag{2.38}$$

In the above equation, *Re* is the Reynolds number defined with the drop radius and *Pr* is the Prandtl number. Therefore, if there is forced convection between the drop and ambient gas, the vaporization rate based on heat transfer number can be obtained as

$$\dot{m}_{tot} = \frac{2\pi R k_g}{c_{pv}} Nu B_T = \frac{2\pi R k_g Nu_\circ}{c_{pv}} \ln\left(1 + B_T\right). \tag{2.39}$$

On the other hand, the convective mass transfer for a vaporizing drop can be estimated in a similar way. If a stationary drop is not vaporizing, the mass transfer rate at the drop surface is

$$\dot{m}_{i,nonvap} = 4\pi R \rho D_{i,g} \left(y_{i,s} - y_{i,\infty}\right). \tag{2.40}$$

For a vaporizing drop, the mass transfer rate at the drop surface can be calculated according to Fick's law and Eq. (2.12) as

$$\dot{m}_{i,vap} = 4\pi R^2 \left(-\rho D \left. \frac{\partial y_i}{\partial r} \right|_R \right) = \dot{m}_{tot} \left(\varepsilon_i - y_{i,s}\right). \tag{2.41}$$

Therefore, using the above two equations, the mass transfer rates for both vaporizing and non-vaporizing conditions can be related as

$$\dot{m}_{i,nonvap} = \dot{m}_{i,vap} \frac{B_{M,i}}{\ln\left(1 + B_{M,i}\right)}. \tag{2.42}$$

Similar to Eq. (2.35) for heat transfer, Eq. (2.42) provides an implication of the relationship between the convective mass transfer coefficients for vaporizing and non-vaporizing drops. Therefore, the Sherwood numbers for both situations can be related as

$$Sh_{i,\circ} = Sh_i \frac{B_{M,i}}{\ln\left(1+B_{M,i}\right)}. \tag{2.43}$$

In the above equation, Sh_i is the Sherwood number of species i for a vaporizing drop, and $Sh_{i,\circ}$ is the Sherwood number for a non-vaporizing drop. Consequently, the vaporization rate of a drop, which has relative motion with the ambient gas, can be calculated as

$$\dot{m}_i = 2\pi R\rho Sh_{i,\circ}\varepsilon_i D_{ig} \ln\left(1+B_{M,i}\right). \tag{2.44}$$

In analogy with the Nusselt number, a similar classical correlation of the Sherwood number for a non-vaporizing sphere is given by

$$Sh_{i,\circ} = 2 + 0.6Re^{1/2}Sc_i^{1/3}. \tag{2.45}$$

Sc_i is the Schmidt number for species i defined as the ratio of viscosity to mass diffusivity, namely,

$$Sc_i = \frac{\nu}{D_{i,g}}. \tag{2.46}$$

In multidimensional engine simulation, liquid drops are injected with a high injection pressure and move at high speeds. Therefore, the Nusselt number and Sherwood number need to be used to correct the vaporization rates according to Eqs. (2.39) and (2.44).

2.4 Multicomponent Drop Vaporization Modeling

The vaporization process of liquid fuel drops and the distribution of fuel vapor have a significant effect on combustion and exhaust emissions in internal combustion engines. As petroleum fuels such as gasoline and diesel fuel are complex mixtures of approximately 200 ~ 300 hydrocarbon species, using the single-component approach may not be accurate enough to simulate their vaporization processes. Despite that the single component approach has been used in engine modeling with success in numerous applications, a more comprehensive vaporization model is required to improve the accuracy of numerical

simulation for future applications. Therefore, instead of using single-component models, a promising way to predict the vaporization behavior more accurately is to use the multicomponent vaporization approaches to model the complex fuel composition and vaporization process (Sirignano, 1983; Megaridis and Sirignano, 1990; Harstad et al., 2003). Particularly, future engines are likely to be operated under low-temperature combustion conditions for emissions reduction (Musculus et al., 2002; Pickett and Siebers, 2004). Under these conditions, lighter fuel components with will vaporize earlier and have a determining effect on the ignition and combustion process. Heavier components on the other hand will vaporize later and affect the emissions formation process, particularly in the presence of wall-film (Wang and Lee, 2005; Kong, 2007). In addition, the single-component vaporization models will not be applicable to simulate the vaporization of the blend of petroleum fuels and biofuels. Consequently, multicomponent vaporization models are required for more accurate engine simulations and a comprehensive review of multicomponent vaporization models can be found in Sazhin (2006).

Discrete component approach is one of the major multicomponent vaporization strategies. Using this approach, a multicomponent fuel is assumed to be composed of a finite number of components that have different properties. One such typical approach uses six components for diesel fuel and seven components for gasoline for vaporization modeling (Ra and Reitz, 2008). Abraham and Magi (1998) treated a multicomponent drop by a combination of several drops which had only one component in each drop, and the size of each drop was the same with the original multicomponent fuel drop. As a result, the vaporization flux of each component can be calculated using traditional single-component strategies. Aggarwal and Mongia (2002) performed multicomponent vaporization calculations using high-pressure phase equilibrium at the drop surface to study the vaporization behavior of a two-component fuel drop at different conditions. Discrete component approach can also be used in the multicomponent modeling of wall-film vaporization. Zeng and Lee (2000) obtained the vaporization flux for each component in the vapor phase by boundary integration and quasi-one-dimensional transport equations or the liquid phase. They used third-order polynomials for temperature and mass fraction profiles in the normal direction of the film to simplify the calculation. Wang et al. (2003) applied the

same vaporization model by assuming gasoline to be composed of four components to study air-fuel mixing in gasoline direct-injection engines. Torres et al. (2003) used a space discretization with several discrete points in the interior of the fuel drop to solve the transport equation for each component and the evolution of composition of the multicomponent drop. Since the transport equations were linear, the computational cost was not high in solving the spatial and temporal variations of temperature and mass fractions.

To use the continuous thermodynamics approach, a continuous function is used to model the distribution of the fuel components. As a result, the number of variables can be greatly reduced compared to the discrete component approach. Tamim and Hallett (1995) developed a continuous thermodynamics vaporization model using a gamma distribution, which is a probability density function (PDF), to describe the molecular weight distribution in a complex multicomponent fuel. In order to correlate the vapor pressure of the components with their molecular weight, a linear correlation between the component molecular weight and the normal boiling point was proposed. The vapor-liquid equilibrium and vapor phase transport equations were also derived. Hallett (2000) further simplified the vapor phase transport by neglecting gas-phase transients and assuming spherical symmetry and constant properties around the drop in the gas phase. Lippert and Reitz (1997) applied the same continuous thermodynamics model, converted the original vapor phase transport equations of the moments to be on mass basis, and implemented the model into an engine simulation code for engine spray modeling. Ra and Reitz (2004) further improved the vaporization model by considering the finite thermal diffusivity in the liquid phase and introduced the drop surface temperature to calculate the heat transfer rate. In order to achieve a more accurate modeling of the compositions of kerosene fuels such as JP-8, Harstad and Bellan (2004) linearly combined two gamma distributions and used the square root of molecular weight as the variable in the combined distribution function. In addition to applications in modeling fuel drops, Wang and Lee (2005) developed a multicomponent model for wall-film vaporization using a gamma distribution as the PDF and also derived the diffusion equation for liquid composition. Other than the gamma distribution, other types of functions such as truncated spectral expansion was also used to model the continuous mixture of a large number of components (Arias-Zugasti and Rosner, 2003).

2.5 Vaporization Modeling under High-Pressure Conditions

In addition to the composition of practical fuels, vaporization modeling also needs to consider the effects of high pressure since liquid fuel drops frequently experience high-pressure conditions in practical combustion devices such as diesel engines and gas turbines. Traditionally, for computational efficiency, drop vaporization models are mostly based on the Raoult's law which is a low-pressure simplification of the general vapor-liquid phase equilibrium. Based on the assumptions of ideal gas and no gas dissolving in the liquid phase, Raoult's law provides a simple relation of the mole fractions of the components in both phases at the phase interface. Since such assumptions are not entirely true under high-pressure conditions, errors will be introduced in the prediction of drop vaporization rate and vapor distribution. To improve the accuracy of multidimensional engine simulation, general phase equilibrium, which is characterized by the equality of fugacity of each component in both phases at the phase interface, need to be used to replace the Raoult's law to provide the boundary conditions of the species equations in both phases. This improvement requires the consideration of real gas behaviors which can be modeled using various types of equations of state such as the virial, Lee-Kesler, and two-parameter cubic equations of state. Of these equations, the two-parameter cubic equations of state, e.g., van der Waals, Redlich-Kwong (RK), Redlich-Kwong-Soave (RKS), and Peng-Robinson (PR), are more frequently used.

Researchers have performed the analysis on the high-pressure drop vaporization behavior without forced or natural convection by solving the governing equations shown in Sec. 2.1. Hsieh et al. (1991) conducted the analysis of high-pressure drop vaporization modeling using conservation equations based on a moving coordinate system and solved equations numerically in both liquid and vapor phases to obtain the drop vaporization rate. The RK equation of state was used to model the real gas behavior in systems composed of single-component drops such as n-pentane and nitrogen. Jia and Gogos (1993) applied similar numerical approaches in the vaporization modeling of n-hexane in a high-pressure nitrogen environment and showed the advantage of PR equation of state compared to RK equation of state. Curtis and Farrell (1992) simulated the high-pressure drop vaporization at diesel engine conditions and discussed the effects of coupled diffusion process and anomalies on drop vaporization. Similar research was also performed by Zhu and Aggarwal (2000) who

used the Arbitrary Lagrangian-Eulerian method with a dynamically adaptive mesh moving with the receding drop surface in solving the governing equations.

High-pressure drop vaporization modeling can also be performed without solving the transient governing equations in the vapor phase. For simplicity, pseudo-steady solutions of the governing equations, which have a solution expressed by the Spalding mass transfer number, are used to evaluate drop vaporization rate. This approach is suitable for the cases with forced convection and can be applied efficiently to the simulation of diesel fuel spray. The pseudo-steady vaporization rate determined by Spalding mass transfer number is derived from the one-dimensional species concentration equation with the assumption that ambient gas does not diffuse into the liquid phase. Even though the amount of ambient gas that dissolves onto the surface of the drop is not negligible under high-pressure conditions, the small diffusion coefficient in the liquid phase may validate such an assumption. Therefore, it is still reasonable to use the pseudo-steady vaporization rate formula at high-pressure conditions. Aggarwal and Mongia (2002) used such a pseudo-steady solution for vaporization rate under high-pressure conditions and PR equation of state to calculate phase equilibrium in modeling the vaporization of binary-component drops. The vaporization results of binary component drops were compared with equivalent single-component drops in the gas turbine environment to study the multicomponent effect. Zeng and Lee (2002) emphasized on the thermal and mass diffusion models (e.g. infinite diffusivity and finite diffusivity models considering the effect of drop recession) for modeling the vaporization of multicomponent fuels based on the pseudo-steady vaporization rate equation and used PR equation of state to consider the non-ideality of ambient gas to calculate phase equilibrium under high-pressure conditions.

In addition to the above studies using discrete component approaches, research on the high-pressure vaporization was extended to multicomponent vaporization models based on continuous thermodynamics. The general phase equilibrium of a semi-continuous system including the continuous distributed components and discrete components was considered (Zhu and Reitz, 2002). The formulas for calculating the parameters of the equation of state based on continuous thermodynamics were also provided.

The multicomponent vaporization model using continuous thermodynamics approach discussed in Sec. 2.4 is based on Raoult's law and Clausius–Clapeyron relation. Under high-pressure conditions, to model the vaporization of complex fuels, an extension of the model by replacing Raoult's law with general phase equilibrium is necessary. Even though Zhu and Reitz (2002) modeled the high-pressure vaporization of multicomponent drops using continuous thermodynamics, a complete multicomponent vaporization model based on the combination of continuous thermodynamics and general phase equilibrium has not been fully developed. Moreover, the vaporization behaviors of biodiesel and its mixture with diesel fuel under high-pressure conditions have not been studied.

2.6 Biodiesel as a Renewable Replacement of Diesel Fuel

The questionable future availability of petroleum fuels and the concern on environmental carbon emissions require more research and applications of renewable fuels. As the promising renewable substitutions of petroleum fuels, biofuels have been used in many combustion devices. With comparable physical and chemical properties, for instance, biodiesel can be used as the partial replacement for diesel fuel, and ethanol can be used together with gasoline. Previous experimental studies showed that comparable engine performance and improved emissions of carbon monoxide, unburned hydrocarbon and soot can be obtained by using biodiesel. A practical way of utilizing biodiesel in a diesel engine is to blend the fuel with diesel fuel by their high miscibility. In this way, significant modifications to the engines are not required. Experimental studies have been conducted on engine performance for using the blends of various kinds of biodiesel and diesel fuel with different blend ratios. It is found that the volume fraction of biodiesel can be up to 20% around which optimum engine thermal efficiency can be obtained without a significant increase in NOx emission (Agarwal and Das, 2001; Lapuerta et al. 2008; Ramadhas et al. 2005; Chio et al., 1997). Despite the extensive experimental studies, there are only limited studies on the vaporization of the mixture of biofuels and petroleum fuels at a fundamental level, as will be discussed in later chapters.

One challenge in modeling biodiesel vaporization is the uncertainties in the fuel composition and properties. Vegetable oils, such as rapeseed methyl ester, soybean methyl

ester, and sunflower methyl ester, are commonly used to produce biodiesel. Different feedstock will lead to different compositions of biodiesel. Therefore, the physical properties of biodiesel can be relatively uncertain. However, despite the difference in feedstock, most of biodiesel derived from vegetable oils are mainly composed of five C16 to C18 fatty acids (Ramadhas et al., 2005; Ramos et al., 2009), i.e., palmitic ($C_{16}H_{32}O_2$), stearic ($C_{18}H_{36}O_2$), oleic ($C_{18}H_{34}O_2$), linoleic ($C_{18}H_{32}O_2$), and linolenic ($C_{18}H_{30}O_2$). Ramos et al. (2009) studied the effect of the raw material composition on biodiesel properties. Wu et al. (2009) tested the effect of feedstock of biodiesel on diesel engine emissions using five different methyl esters. Yuan et al. (2003) also provided methods to predict the physical properties of biodiesel using these five pure fatty acids using an ideal mixing rule. Based on the mixing rule, the critical and physical properties of biodiesel can be predicted according to the mass/mole fractions of its major components.

To achieve a better understanding of biodiesel combustion in engines, the drop vaporization characteristics of biodiesel need to be studied. The vaporization of biodiesel drops was studied experimentally and numerically only recently. Morin et al. (2000, 2004) performed experiments on the single, stagnant drop vaporization of rapeseed methyl ester and sunflower methyl ester and obtained the experimental data on drop vaporization histories. Barata (2008) numerically simulated the dispersion and vaporization of rapeseed methyl ester drops that were injected into a turbulent cross-stream and compared the results with those using conventional fuels. Modeling of diesel-biodiesel drop vaporization has been based on well-defined properties of the two fuels and is essentially a binary-component approach (McCrady et al., 2007; Ra et al., 2008). In the above approaches, both diesel fuel and biodiesel are treated as single-component fuels. Despite the increasing importance of biofuel-petroleum fuel blends application, a comprehensive vaporization model for the fuel blend and considers the complex components of both fuels is not currently available.

2.7 Bio-oil Utilization

Bio-oil, which is also called pyrolysis oil, is a liquid fuel produced through the vapor condensation during the fast pyrolysis process of wood, corn, or other vegetable biomass at a moderate temperature around 500 ˚C (Shihadeh and Hochgreb, 2000). Bio-oil is usually in

black-brownish color containing significant amount of moisture (15-25 wt%), particles, nitrogen, alkali, and tar. The fuel has a heating value about half of that of No. 2 diesel fuel and is more dense and viscous than No. 2 diesel fuel. The energy density of bio-oil is high and the cost of bio-oil production is relatively low compared with other biofuels, so the application of bio-oil is potentially profitable. Therefore, bio-oil can be used in large-scale in many combustion devices. Since the application of bio-oil provides significant advantages by offsetting the carbon dioxide emission of fuel combustion (Mohan et al., 2006), a great deal of research has also shown that bio-oil can be possibly used in the existing combustion devices (Chiaramonti et al., 2007; Czernik and Bridgwater, 2004).

The application of bio-oil in diesel engines has been studied experimentally. Engine testing results showed that high thermal efficiency, which can be up to 44.9%, can be obtained by using bio-oil in a diesel engine (Solantausta et al., 1993; Solantausta et al., 1995; Jay et al., 1995). Shihadeh and Hochgreb (2000) experimentally compared the performance of a high-speed diesel engine fueled with bio-oil and diesel fuel, respectively. Results of their experiments show that the thermal efficiency of bio-oil is equal to that of diesel fuel. Bio-oil leads to longer ignition delay which is due to not only the poor vaporization and atomization of the liquid fuel but also the chemical composition of the fuel. They further concluded that the water content and thermal cracking are the most important parameters in affecting the ignition and combustion performance. Lower water content and greater cracking will yield better performance, and other physical properties do not have significant effects on the performance. The water content, which can be up to 20-30% on mass basis, in bio-oil can reduce the local combustion temperature and therefore be beneficial in reducing the emission of NOx. Combustion experiments performed by Osamaa et al. (2008) showed that NOx emission was reduced while increased emissions of particulate matter were obtained using bio-oil. It was also observed that pilot injection is needed and the heat release rate can be very high.

Moreover, research has been conducted on the single-drop combustion of bio-oil. Shaddix and Tennision (1998) performed experimental study on single bio-oil drop combustion with a focus on the micro-explosion phenomenon. Results show that micro-explosion happens very early in the combustion process and the presence of char particles

accelerates the occurrence of micro-explosion. Methanol and other low-volatility compounds can be used to accelerate the micro-explosion, while adding water will delays the micro-explosion. Wornat et al. (1994) experimentally compared the single drop combustion behavior of different multicomponent fuels such as No. 2 diesel fuel, pine oil, and oak oil. The difference in the burning behavior such as flame color and soot emissions of such fuel was observed. In contrast, the similarity in drop burning time among these fuel drops was also found.

Even though bio-oil has been experimentally tested in diesel engines, the detailed spray and vaporization behaviors of bio-oil have not been studied in detail. Since the feedstock and pyrolysis process are usually different for different producers, the composition of bio-oil can vary significantly. As a major feedstock of bio-oil, wood is mainly composed of five chemical constituents including cellulose, hemicellulose, lignin, organic extractives, and inorganic minerals. The pyrolysis of the first three constituents produces the components of bio-oil, and it is found out that bio-oil is a complex mixture of water, guaiacols, catecols, syringols, vanillins, furancarboxaldehydes, isoeugenol, pyrones, acetic acid, formic acid and other carboxylic acids (Mohan et al. 2006). Goos (1954) reported 231 compounds in the liquid product from the destructive distillation of wood. Evans and Milne (1987) used experimental approaches such as molecular-beam and mass spectrometric sampling to identify the components reported by previous studies. Branca et al. (2003) used gas chromatographic/mass spectrometry (GC/MS) technique and experimentally studied the compositions of bio-oil produced from wood by different fast pyrolysis processes. Results showed that despite the uncertainties in the fast pyrolysis processes, the components of bio-oil produced using wood can be grouped into the following categories, i.e., water, minor and major carbohydrates, furans, phenols, guaiacos, and syringols. Different from petroleum fuels which are mainly composed of hydrocarbon species, the components of bio-oil are more various. Therefore, a discrete component approach will be appropriate for the vaporization modeling of bio-oil by selecting some representative components from each category reported by Branca et al (2003).

CHAPTER 3 MODEL FORMULATION

This chapter describes the numerical models developed/used in this study. In engine simulation, multicomponent vaporization modeling accounts for the effect of fuel composition on drop vaporization behavior. Depending on the characters of the multicomponent fuel, different modeling strategies were used. To perform multicomponent vaporization modeling, it is necessary to consider the difference in vaporization rates of different components and track the mass/mole fraction of each component during the vaporization process. If there are only a limited number of components in the drop, the vaporization of individual components can be simulated and drop vaporization is a collective result of the vaporization of all the components. Such an approach is called a discrete component model. However, if the number of components in the fuel is large, e.g., hundreds of components, it is inconvenient to track the mass/mole fractions of all of the components. Vaporization modeling of this kind of fuels stimulates the development of continuous thermodynamics model that uses a probability density function to describe the molecular weight distribution of the components in the fuel. Using continuous thermodynamics, the number of variables during the vaporization calculation will be greatly reduced, while the information of fuel composition can be monitored. Due to the need to model the vaporization of petroleum and biofuels, which have complex fuel components, both continuous thermodynamics and discrete component models were developed in this study.

In this chapter, effects of high pressure on drop vaporization were also considered, and a high-pressure multicomponent vaporization model will also be described. The above models were implemented into the baseline CFD code, KIVA-3V (Amsden, 1999). Several spray and combustion-related submodels will be also described briefly.

3.1 Continuous Thermodynamics

Continuous thermodynamics is one of the most important multicomponent vaporization approaches. In contrary to the discrete component method, continuous thermodynamics is a method preferred for complex fuels such as diesel fuel and gasoline which are composed of 200~300 hydrocarbon species. By using continuous thermodynamics, the molecular weights of the components of the fuel are described by a probability density function. In this study, a

gamma distribution is used to model the molecular weight distribution of petroleum fuel components.

The gamma distribution used in this study is a probability distribution function based on gamma function, i.e.,

$$f(I) = \frac{(I-\gamma)^{\alpha-1}}{\beta^{\alpha}\Gamma(\alpha)} \exp\left[-\left(\frac{I-\gamma}{\beta}\right)\right]. \tag{3.1}$$

$\Gamma(\alpha)$ is the gamma function. In the gamma distribution, γ can be regarded as the origin of the distribution and is usually assumed constant during the vaporization process. α and β are the two parameters determining the shape of the distribution and will change during the vaporization process. A gamma distribution for diesel fuel with α=23, β=8.15, and γ=0 is plotted as shown in Figure 3.1.

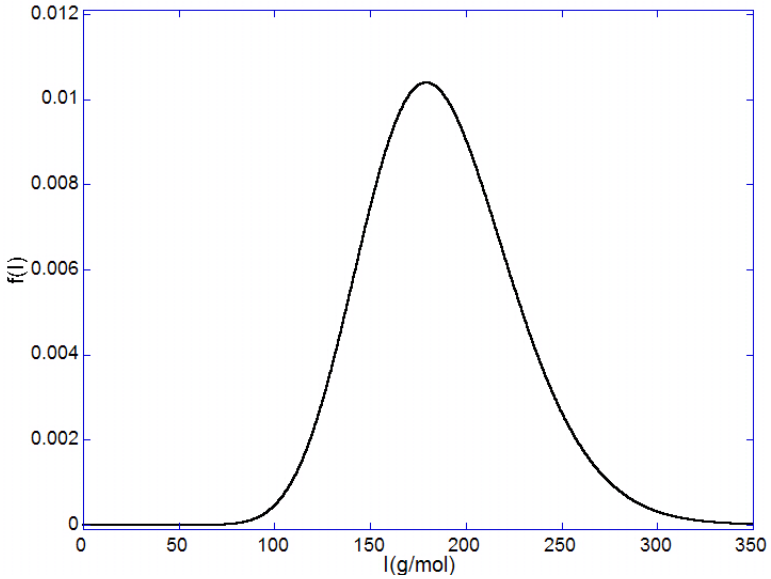

Figure 3.1 Gamma distribution for diesel fuel with α=23, β=8.15, and γ=0

Using the above molecular weight distribution, the mole fraction of species in the range ΔI can be described as

$$Y_i = f(I)_i \, \Delta I_i \,. \tag{3.2}$$

The integration of the above equation for I from γ to infinity (∞) will be equal to unity, i.e.,

$$\int_{\gamma}^{\infty} f(I)dI = 1. \tag{3.3}$$

It is expected that the distribution parameters will change during the drop vaporization process. However, in practice, it is not convenient to calculate the variations of α and β directly. Instead, the moments of the distribution are selected as the variables controlling the composition during the vaporization process. Since the origin, γ, is usually kept constant during the entire vaporization process, the first and second moments of the distribution are enough to describe the distribution. The first moment is obtained by weighing the molecular weight (I) with the distribution, namely,

$$\theta = \int_{\gamma}^{\infty} f\left(I\right) IdI \,. \tag{3.4}$$

The first moment of the distribution is also the mean molecular weight of the multicomponent fuel. Using a gamma distribution, the mean molecular weight can be obtained as a function of distribution parameters as

$$\theta = \alpha \times \beta + \gamma \,. \tag{3.5}$$

The second moment of the distribution can be obtained by weighing I^2 with the distribution function as

$$\Psi = \int_{\gamma}^{\infty} f\left(I\right) I^2 dI \,. \tag{3.6}$$

Similarly, putting in the gamma distribution in the above integration, the second moment can also be related to the distribution parameters as

$$\Psi = \theta^2 + \sigma^2 = \left(\alpha\beta + \gamma\right)^2 + \alpha\beta^2 \,, \tag{3.7}$$

where σ^2 is the variance of the distribution.

For a multicomponent fuel modeled by such a molecular weight distribution, the vaporization rates of the continuously distributed components will be different. Therefore, the composition of the fuel will change during the vaporization. To obtain the variations of

the above two moments, consider a liquid drop mixed by multiple fuels one of which can be modeled using continuous thermodynamics. The species concentration equation (Eq. (2.8)) is true for the continuously distributed components. Integrate the equation from drop center (r=0) to drop surface (r=R), i.e.,

$$\int_0^R \frac{\partial\left(c_l r^2 X_I\right)}{\partial t} dr = -\int_0^R \frac{\partial\left(r^2 J_I\right)}{\partial r} dr\,, \tag{3.8}$$

where c_l is the molar density and X_I is the mole fraction of the continuous fuel component in the liquid phase, namely,

$$X_I = X_F\, f\left(I\right) dI\,. \tag{3.9}$$

Subscript F denotes the multicomponent fuel. Note that Eq. (3.8) is on molar basis different from Eq. (2.8) which is on mass basis. In this study, the distribution function is assumed to be invariant in the radial direction in the liquid phase, while the mole fraction of the multicomponent fuel (X_F) can be a function of radius. Define the average mole fraction of a fuel in the liquid phase as

$$\bar{X}_F = \frac{1}{\frac{4}{3}\pi R^3}\int_0^R 4\pi r^2 X_F dr\,. \tag{3.10}$$

Note that the diffusion flux at drop center is zero due to symmetry. Assuming that the molar density does not change along radial direction in the liquid phase, the integration of Eq. (3.8) leads to

$$\frac{R}{3}\frac{d\left(c_l \bar{X}_I\right)}{dt} = -J_{I,R}\,, \tag{3.11}$$

where

$$\bar{X}_I = \bar{X}_F\, f\left(I\right) dI\,. \tag{3.12}$$

Using Eq. (3.11), the boundary condition at the drop surface described by Eq. (2.12) can be rewritten as

$$\dot{N}''X_{I,R} - \frac{R}{3}\frac{d\left(c_l \bar{X}_I\right)}{dt} = \left(\dot{N}''Y_I + J_{I,v}\right)\Big|_R . \tag{3.13}$$

Y_I is the mole fraction of continuous species in the vapor phase defined based on the vapor distribution function as

$$Y_I = Y_F f_v(I) dI . \tag{3.14}$$

$J_{I,v}$ in Eq. (3.13) is the diffusion flux of continuous components in the vapor phase. For a binary diffusion system, which is composed of the fuel and ambient gas, $J_{I,v}$ can be described using the Fick's law as

$$J_{I,v} = -c_v D_I \frac{dY_I}{dr} . \tag{3.15}$$

D_I is the binary mass diffusivity between the continuous components and ambient gas. Using Eqs. (3.9) and (3.14), the integration of Eq. (3.13) for I from γ to ∞ leads to

$$\frac{d\left(c_l \bar{X}_F\right)}{dt} = \frac{3}{R}\left\{\dot{N}''\left(X_{F,R} - Y_{F,R}\right) + c_v \int_\gamma^\infty D_I \left\{\frac{d}{dr}\left[Y_F f_v(I)\right]\right\}_R dI\right\}. \tag{3.16}$$

Multiplying with I and I^2 on both sides of Eq. (3.13) respectively, the integration for I from γ to ∞ leads to the variation rate of the first and second moments of the liquid phase as

$$\begin{aligned}\frac{d\left(c_l \bar{X}_F \theta_l\right)}{dt} &= c_l \bar{X}_F \frac{d\theta_l}{dt} + \theta_l \frac{d\left(c_l \bar{X}_F\right)}{dt} \\ &= \frac{3\dot{N}''}{R}\left\{\theta_l X_{F,R} - Y_{F,R}\theta_{v,R} + \frac{c_v}{\dot{N}''}\int_\gamma^\infty D_I I \left\{\frac{d}{dr}\left[Y_F f_v(I)\right]\right\}_R dI\right\}\end{aligned} \tag{3.17}$$

and

$$\begin{aligned}\frac{d\left(c_l \bar{X}_F \Psi_l\right)}{dt} &= c_l \bar{X}_F \frac{d\Psi_l}{dt} + \Psi_l \frac{d\left(c_l \bar{X}_F\right)}{dt} \\ &= \frac{3\dot{N}''}{R}\left\{\Psi_l X_{F,R} - Y_F \Psi_{v,R} + \frac{c_v}{\dot{N}''}\int_\gamma^\infty D_I I^2 \left\{\frac{d}{dr}\left[Y_F f_v(I)\right]\right\}_R dI\right\}.\end{aligned} \tag{3.18}$$

In the above two equations, it can be seen that the derivatives of the liquid phase moments with respect to time can be obtained. Therefore, the change of molecular weight distribution during the vaporization process can be calculated. Using Eq. (3.16) to replace the second term on the right hand side of the above equations, the both equations can be simplified to

$$\frac{d\theta_l}{dt}=\frac{3\dot{N}''}{c_l\bar{X}_F R}\left\{\theta_l Y_{F,R}-\theta_{v,R}Y_{F,R}+\frac{c_v}{\dot{N}''}\int_\gamma^\infty D_I\left(I-\theta_l\right)\left\{\frac{d}{dr}\left[Y_F f_v\left(I\right)\right]\right\}_R dI\right\}, \tag{3.19}$$

and

$$\frac{d\Psi_l}{dt}=\frac{3\dot{N}''}{c_l\bar{X}_F R}\left\{\Psi_l Y_{F,R}-\Psi_{v,R}Y_{F,R}+\frac{c_v}{\dot{N}''}\int_\gamma^\infty D_I\left(I^2-\Psi_l\right)\left\{\frac{d}{dr}\left[Y_F f_v\left(I\right)\right]\right\}_R dI\right\}. \tag{3.20}$$

$\theta_{v,R}$ and $\Psi_{v,R}$ are the first and second moments of the distribution of fuel vapor at drop surface, respectively, and are defined similarly to those for liquid phase as

$$\theta_v=\int_\gamma^\infty f_v\left(I\right)IdI, \psi_v=\int_\gamma^\infty f_v\left(I\right)I^2dI\ . \tag{3.21}$$

It can be seen that Eqs. (3.19) and (3.20) involve the derivative of vapor phase molecular weight distribution with respect to *r*. The integration in Eq. (3.19) can be expanded as

$$\begin{aligned}&\int_\gamma^\infty D_I\left(I-\theta_l\right)\left\{\frac{d}{dr}\left[Y_F f_v\left(I\right)\right]\right\}_R dI\\&=\left(\tilde{D}\theta_v-\bar{D}\theta_l\right)\frac{dY_F}{dr}+Y_F\frac{d}{dr}\left(\tilde{D}\theta_v-\bar{D}\theta_l\right)-Y_F\left\{\int_\gamma^\infty f_v\left(I\right)\frac{d}{dr}\left[D_I\left(I-\theta_l\right)\right]dI\right\},\end{aligned} \tag{3.22}$$

where $\bar{D}$ and $\tilde{D}$ are the mean diffusivities defined by

$$\bar{D}=\int_\gamma^\infty f_v\left(I\right)D\left(I\right)dI, \tilde{D}=\frac{1}{\theta_v}\int_\gamma^\infty f_v\left(I\right)D\left(I\right)IdI\ . \tag{3.23}$$

In Eq. (3.22), neglect the variation of diffusivity in the radial direction. Thus, Eq. (3.19) can be further simplified to

$$\frac{d\theta_l}{dt}=\frac{3}{c_l\bar{X}_F R}\left\{\dot{N}''Y_{F,R}\left(\theta_l-\theta_{v,R}\right)+c_v\left[\frac{d\left(\tilde{D}\theta_v Y_F\right)}{dr}-\theta_l\frac{d\left(\bar{D}Y_F\right)}{dr}\right]_R\right\}. \tag{3.24}$$

In a similar way, Eq. (3.20) can also be simplified to

$$\frac{d\Psi_l}{dt}=\frac{3}{c_l\bar{X}_F R}\left\{\dot{N}''Y_{F,R}\left(\Psi_l-\Psi_{v,R}\right)+c_v\left[\frac{d\left(\hat{D}\Psi_v Y_F\right)}{dr}-\Psi_l\frac{d\left(\bar{D}Y_F\right)}{dr}\right]_R\right\}, \tag{3.25}$$

where $\hat{D}$ is the second moment averaged diffusivity defined by

$$\hat{D}=\frac{1}{\Psi_v}\int_\gamma^\infty f_v(I)D(I)I^2dI\,. \tag{3.26}$$

It can be seen from Eqs. (3.24) and (3.25) that to estimate the partial derivatives of both liquid phase moments, the partial derivatives in both equations need to be evaluated at drop surface. In this study, the pseudo-steady species equation for the continuously distributed components is used, i.e.,

$$\frac{d}{dr}\left(c_v r^2 v_r Y_I\right)=-\frac{d\left(r^2 J_I\right)}{dr}. \tag{3.27}$$

Integrating the above equation from γ to ∞ for molecular weight I, the result is

$$\frac{d}{dr}\left(c_v r^2 v_r Y_F\right)=\frac{d}{dr}\left(r^2 c_v\int_\gamma^\infty D_I\frac{dY_F f_v(I)}{dr}dI\right). \tag{3.28}$$

Assuming that the diffusivity D_I is not a function of r, the above equation can be written as

$$\frac{d}{dr}\left(c_v r^2 v_r Y_F\right)=c_v\frac{d}{dr}\left(r^2\frac{dY_F\bar{D}}{dr}\right). \tag{3.29}$$

v_r in the above equations is the molar-averaged velocity defined by

$$v_r=\frac{\dot{N}}{4\pi r^2 c_v}, \tag{3.30}$$

where $\dot{N}$ is the molar vaporization rate. Therefore, Eq. (3.29) can be further rewritten as

$$\dot{N}\frac{dY_F}{dr} = 4\pi c_v \frac{d}{dr}\left(r^2 \frac{dY_F \bar{D}}{dr}\right). \tag{3.31}$$

The above equation can be simplified by neglecting the variation of the averaged diffusivity in the radial direction. Integrating the above differential equation from drop surface (r=R) to arbitrary location r, the resulting equation is

$$\frac{dY_F}{dr} = \frac{R^2}{r^2}\frac{dY_F}{dr}\bigg|_R \exp\left[\frac{\dot{N}}{4\pi\bar{D}c_v}\left(\frac{1}{R}-\frac{1}{r}\right)\right]. \tag{3.32}$$

Further integrate the above equation from r=R to infinity, and the derivative of fuel mole fraction with respect to r at drop surface can be obtained as

$$\frac{dY_F}{dr}\bigg|_R = \frac{\dot{N}\left(Y_{F,\infty}-Y_{F,R}\right)}{4\pi R^2 \bar{D}c_v\left[\exp\left(\dfrac{\dot{N}}{4\pi R\bar{D}c_v}\right)-1\right]}. \tag{3.33}$$

To obtain the derivative involving the first moment, multiply molecular weight I on both sides of Eq. (3.27) and integrate for I from γ to ∞, and the result is

$$c_v \frac{d}{dr}\left(r^2 v_r Y_F \theta_v\right) = \frac{d}{dr}\left(r^2 c_v \frac{dY_F \tilde{D}\theta_v}{dr}\right). \tag{3.34}$$

Integrate the above equation for r from drop surface (r=R) to arbitrary location r, and the integration lead to

$$\frac{d\left(Y_F\theta_v\right)}{dr} = \frac{R^2}{r^2}\frac{d\left(Y_F\theta_v\right)}{dr}\bigg|_R \exp\left[\frac{\dot{N}}{4\pi\tilde{D}c_v}\left(\frac{1}{R}-\frac{1}{r}\right)\right]. \tag{3.35}$$

Further integrate the above equation for r from drop surface (r=R) to infinity, and the derivative involving first moment at drop surface can be obtained as

$$\frac{d\left(Y_F\theta_v\right)}{dr}\bigg|_R = \frac{\dot{N}\left(Y_{F,\infty}\theta_{v,\infty}-Y_{F,R}\theta_{v,R}\right)}{4\pi R^2 \tilde{D}c_v\left[\exp\left(\dfrac{\dot{N}}{4\pi R\tilde{D}c_v}\right)-1\right]}. \tag{3.36}$$

Similarly, for the second moment, the derivative at drop surface can be derived as

$$\left.\frac{d\left(Y_F\Psi_v\right)}{dr}\right|_R = \frac{\dot{N}\left(Y_{F,\infty}\Psi_{v,\infty} - Y_{F,R}\Psi_{v,R}\right)}{4\pi R^2\hat{D}c_v\left[\exp\left(\frac{\dot{N}}{4\pi R\hat{D}c_v}\right)-1\right]}. \tag{3.37}$$

Using the resulting equations of the above analysis, i.e., Eqs. (3.33), (3.36), and (3.37), the variation rates of both moments of the liquid phase can be calculated using Eqs. (3.24) and (3.25), and the variation of the liquid phase composition during vaporization can be estimated.

It can be seen that the molecular weight distribution in the vapor phase, i.e., $f_v(I)$ must be determined to calculate the variation rates of both moments as described in Eqs. (3.24) and (3.25). Under low pressure conditions, the vapor phase molecular weight distribution can be related to the distribution in the liquid phase using the Raoult's law described in Eq. (2.10). By using continuous thermodynamics, the vapor pressure of the continuous components is a function of the molecular weight. Therefore, using Raoult's law, the vapor phase distribution function at drop surface can be described as

$$f_v(I) = \frac{X_{F,R}P_{sat}(I)}{Y_{F,R}P}\, f_L(I). \tag{3.38}$$

In the above equation, $P_{sat}(I)$ is the vapor pressure of the continuous components evaluated at drop surface temperature, and P is the actual ambient pressure at the drop surface. To obtain vapor pressure as a function of molecular weight, its relation with temperature using Clausius-Clapeyron equation can be used. Atmospheric pressure and normal boiling point can be used as reference in the equation. In continuous thermodynamics model, normal boiling point is approximately linearly correlated with molecular weight as

$$T_b = a_b + b_b I\,, \tag{3.39}$$

where a_b and b_b are constants determined by the type of the fuel. Tamin and Hallett (1995) suggested 241.4 and 1.45 as the values of a_b and b_b, respectively for petroleum fuels. Using the normal boiling point, vapor pressure can then be calculated using Clausius-Clapeyron equation as

$$P_{sat}(I) = p_{atm} \exp\left[A(1-BI)\right]. \tag{3.40}$$

A and B in the above equation are related to a_b and b_b as

$$A = \frac{s_{fg}}{\bar{R}}\left(1-\frac{a_b}{T}\right), B = \frac{b_b}{T-a_b}. \tag{3.41}$$

s_{fg} is the entropy of vaporization.

Using the above two equations, the vapor phase mole fraction of the fuel at drop surface can be integrated according to Eq. (3.38) as

$$Y_{F,R} = X_{F,R}\int_{\gamma}^{\infty} \frac{P_{sat}(I)}{P} f_L(I)\, dI = \frac{X_{F,R}P_{atm}}{P} \frac{\exp\left[A(1-\gamma B)\right]}{\left(1+AB\beta_L\right)^{\alpha_L}}. \tag{3.42}$$

Similarly, the integrations in Eq. (3.21) result in the first and second moments in the vapor phase at drop surface, i.e.,

$$\theta_v = (\theta_l - \gamma)\left[1+\frac{AB\sigma_l^2}{(\theta_l-\gamma)}\right]^{-1} + \gamma \tag{3.43}$$

and

$$\Psi_v = \theta_v^2 + \sigma_v^2 = \theta_v^2 + \sigma_l^2\left(\frac{\theta_v-\gamma}{\theta_l-\gamma}\right)^2. \tag{3.44}$$

3.2 Discrete Component Approach

Different from the continuous thermodynamics approach, if the fuel is composed of only a few components, it is desirable to track the mass/mole fraction of each component during the vaporization process. Using this approach, the binary diffusion equation in the vapor phase for each component as shown in Eq. (2.17) needs to be considered, and Eq. (2.21) provides the vaporization rates of each component. The difficulty is how to calculate the vaporization rate fraction of each component if there are more than two components in the fuel. To calculate the vaporization rate fraction, the total vaporization rate of the drop can be obtained from Eq. (2.21) as

$$\dot{m}_{tot} = 4\pi R\rho D_{i,g} \ln\left(1 + B_{M,i}\right). \tag{3.45}$$

The above equation shows that the total vaporization rate can be obtained from the diffusivity and mass transfer number of each individual component. Therefore, for any two arbitrary components in the fuel, the following equation must be true:

$$D_{i,g} \ln\left(1 + B_{M,i}\right) = D_{j,g} \ln\left(1 + B_{M,j}\right). \tag{3.46}$$

The above equation provides *n*-1 equations for vaporization rate fraction ε, if there are *n* components in the multicomponent fuel. Together with Eq. (2.19), there will be a total of *n* equations, and the vaporization rate fraction for each component can be calculated with numerical iteration methods. If the diffusivities of all of the components are assumed identical, Eq. (3.46) reduces to the following relation for any two components:

$$\frac{y_{i,s} - y_{i,\infty}}{\varepsilon_i - y_{i,s}} = \frac{y_{j,s} - y_{j,\infty}}{\varepsilon_j - y_{j,s}}. \tag{3.47}$$

To calculate the drop vaporization rate using the discrete component approach, the mass fraction of each component at drop surface and infinity must be known to calculate the mass transfer number shown in Eq. (2.21). For drop vaporization calculation under low-pressure conditions, according to Raoult's law, the mole fraction of fuel vapor at drop surface must be calculated using the vapor pressure. However, for some biofuels such as biodiesel and bio-oil, vapor pressure data are not available and need to be estimated with correlations. In this study, the vapor pressure is estimated using the following Pitzer's expansion,

$$\ln\left(P_{vpr}\right) = f^{(0)}\left(T_r\right) + \omega f^{(1)}\left(T_r\right), \tag{3.48}$$

where $f^{(0)}$ and $f^{(1)}$ are correlations in Lee and Kesler's form (Reid et al., 1987) expressed as

$$f^{(0)} = 5.92714 - \frac{6.09648}{T_r} - 1.28862\ln\left(T_r\right) + 0.169347T_r^6 \tag{3.49}$$

and

$$f^{(1)} = 15.2518 - \frac{15.6875}{T_r} - 13.4721\ln\left(T_r\right) + 0.43577T_r^6. \tag{3.50}$$

In Eq. (3.48), ω is the acentric factor which is the value of the following equation at T_r=0.7:

$$\omega = -\log\left(P_{vpr}\right) - 1. \tag{3.51}$$

In the above equations, T_r is the reduced temperature which is defined as the ratio of temperature to critical temperature, i.e. $T_r=T/T_c$. P_{vpr} is the reduced vapor pressure based on critical pressure. The latent heat of the fuel must be known for the calculation of drop heating rate as described by Eq. (2.26). In this study, the latent heat is estimated using Fish and Lielmezs' method (Reid et al., 1987):

$$L = L_b \frac{T_r}{T_{br}} \frac{X + X^q}{1 + X^p}, \tag{3.52}$$

where X is determined by reduced temperature and reduced boiling point, namely,

$$X = \frac{T_{br}}{T_r} \frac{1 - T_r}{1 - T_{br}}. \tag{3.53}$$

Subscript b denotes normal boiling point. The above equations use the latent heat at normal boiling point and evaluate the departure from the value at normal boiling point to the value at arbitrary temperature. The latent heat at normal boiling point can be estimated using Riedel method (Reid et al., 1987), i.e.,

$$L_b = 1.093 R T_c \left[T_{br} \frac{\ln P_c - 1.013}{0.930 - T_{br}} \right]. \tag{3.54}$$

In this study, Fuller's correlation is used to estimate the binary diffusion coefficient. This correlation shows that binary diffusion coefficient is determined by temperature and pressure, i.e.,

$$D_{12} = \frac{0.000143 T^{1.75}}{\sqrt{2} P \left[1/M_1 + 1/M_2\right]^{-1/2} \left[\left(\Sigma_v\right)_1^{1/3} + \left(\Sigma_v\right)_2^{1/3} \right]^2}. \tag{3.55}$$

In the above equation, M stands for molecular weight, and Σ_v is the summation of diffusion volumes of the atoms in the molecular structure of a component. Detailed information about atom diffusion volumes can be found in Reid et al., (1987).

Additionally, drop expansion, indicating a decrease in drop density usually, happens at the beginning of the vaporization process when the drop vaporization rate is slow such that most of the heat is used for increasing drop temperature but not vaporization latent heat. To achieve a more accurate prediction of drop vaporization history, the variation of density with changing drop temperature needs to be evaluated. In this study, the Rackett technique, which is further modified by Spencer and Danner (Reid et al., 1987; Yuan et al., 2003), is used to model the density as a function of drop temperature, namely,

$$\rho = \frac{\rho_R}{Z_{RA}^{\phi}}. \tag{3.56}$$

In the above equation, ρ_R is the density at reference temperature, which is taken as 273 K in this study. Z_{RA} is a constant determined by

$$Z_{RA} = 0.29056 - 0.08775\omega. \tag{3.57}$$

The exponent ϕ of Z_{RA} in Eq. (3.56)is defined as

$$\phi = \left(1 - T_r\right)^{2/7} - \left(1 - T_{rR}\right)^{2/7}. \tag{3.58}$$

In the above equation, T_{rR} is the reduced reference temperature.

It can be seen that to use the above correlations, critical properties of the components need to be known. In this study, Ambrose and Joback group contribution techniques (Reid et al., 1987) are mainly used to estimate the critical properties of each component. For instance, Ambrose's method calculates critical temperature using normal boiling temperature which can be obtained from available data source, namely,

$$T_c = T_b\left[1 + \left(1.242 + \Sigma\Delta_T\right)^{-1}\right]. \tag{3.59}$$

Δ_T is a constant of an atom or a group of atoms which build up the component, and the values of Δ_T can be found in Reid et al. (1987). Critical volumes of individual components can also be estimated with Ambrose's group contribution method as

$$V_c = 40 + \Sigma\Delta_V. \tag{3.60}$$

The values of Δ_V of atoms or group of atoms, which build up the component, can also be found in Reid et al. (1987). In a similar way, critical pressure can be obtained by

$$P_c = M\left(0.339 + \sum \Delta_P\right)^{-2}. \tag{3.61}$$

In contrast to Eq. (3.45), an alternative discrete component vaporization modeling strategy is to assume the multicomponent fuel to be a pure component, and the vaporization calculation can be greatly simplified. The critical properties of the pure component are obtained as the mean values of the critical properties of individual actual components. The mean values are calculated according to the mole fractions of individual components. Thus, the effect of fuel composition on its vaporization behavior is still considered. In this study, the mixing rule for Lee-Kesler equation of state (Reid et al., 1987) is used to calculate the mean critical properties. Using the mixing rule, the mean critical temperature of the modeled pure component can be calculated as

$$T_{cm} = \frac{1}{V_{cm}^{1/4}} \sum_i \sum_j y_i y_j V_{cij}^{1/4} T_{cij} \ . \tag{3.62}$$

In the above equation, y is the mole fraction of the actual fuel component. T_{cij} is calculated with the critical temperatures of component i and j as

$$T_{cij} = (T_{ci} T_{cj})^{1/2} k'_{ij}, \tag{3.63}$$

where k'_{ij} is a binary constant. For the some binary pairs without known values, k'_{ij} is set to unity. The mean critical volume of the fuel can be calculated using the following relation:

$$V_{cm} = \sum_i \sum_j y_i y_j V_{cij} \ , \tag{3.64}$$

where V_{cij} is calculated by

$$V_{cij} = \frac{1}{8}\left(V_{ci}^{1/3} + V_{cj}^{1/3}\right). \tag{3.65}$$

T_{ci} and V_{ci} are respectively the critical temperature and volume of individual components. Using the mean critical temperature and volume, the mean critical pressure can be estimated as

$$P_{cm} = \left(0.2905 - 0.085\omega_m\right) RT_{cm} / V_{cm} . \tag{3.66}$$

ω_m is the mole-averaged acentric factor. Using Eqs. (3.62), (3.64), and (3.66), the original multicomponent fuel can be model as a single-component fuel with the mean critical properties which can be used in the correlations for the estimation of physical properties needed for vaporization calculation.

This strategy is best applicable for multicomponent fuels composed of components with close properties. For this kind of fuels, discrete component approach does not show a significant advantage in the accuracy compared to this strategy. A good example of this kind of fuel is biodiesel which is composed of five components with similar chemical formulas. Therefore, in this study, this approach is named as biodiesel vaporization (BV) model and vaporization simulation of biodiesel drops is performed mostly using this approach. Comparison between the discrete component approach and the biodiesel vaporization model will be shown in Sec. 4.4.

3.3 Phase Equilibrium under High-Pressure Conditions

Liquid-vapor phase equilibrium provides the boundary conditions for the governing equations in both phases. The Raoult's law mentioned in above sections is the simplified phase equilibrium which is only true at low-pressure conditions. Under high-pressure conditions, rather than Raoult's law, the general phase equilibrium, which is applicable for all of the conditions, needs to be used. For a liquid-vapor system at constant temperature and pressure, phase equilibrium requires minimum total Gibbs free energy, namely,

$$d\bar{G} = 0 . \tag{3.67}$$

Define chemical potential, which is the partial molar Gibbs free energy, i.e.,

$$\mu_i = \frac{\partial \bar{G}}{\partial N_i} . \tag{3.68}$$

It can be shown that for a liquid-vapor system at constant temperature and pressure, phase equilibrium leads to the equality of chemical potential of each species in both phases, i.e.,

$$\mu_{i,l} = \mu_{i,v} . \tag{3.69}$$

Subscripts *l* and *v* denotes liquid and vapor phases, respectively. In practice, it is not convenient to estimate chemical potential directly. Therefore, the phase equilibrium is further deduced by introducing fugacity, namely,

$$RTd\left(\ln \hat{f}_i\right) = d\mu_i . \tag{3.70}$$

In the above equation, ^ indicates denotes the property of a component in a mixture. Thus, Eq. (3.69) can be described as the equality of fugacity in both phases, namely,

$$\hat{f}_{i,l} = \hat{f}_{i,v} . \tag{3.71}$$

Fugacity has the same unit as pressure and is equal to pressure for an ideal gas. In general, fugacity can be related with pressure by the definition of fugacity coefficient, which is the ratio of fugacity to the product of pressure and mole fraction, i.e.,

$$\hat{\phi}_i = \frac{\hat{f}_i}{Y_i P} . \tag{3.72}$$

Using the concept of fugacity coefficient, the mole fractions of a component in both liquid and vapor phases can be related using the general phase equilibrium as

$$Y_i = X_i \frac{\hat{\phi}_{i,l}}{\hat{\phi}_{i,v}} , \tag{3.73}$$

where x_i and y_i are the mole fractions in liquid and vapor phases, respectively.

It can be seen from the above equation that the mole fractions of a component in both phases are related by the ratio of fugacity coefficients of the component in both phases. The fugacity coefficient for a component in a mixture can be calculated considering the departure function of Helmoltz energy (Reid et al., 1987):

$$\mu_i - \mu_i^{\circ} = \frac{\partial}{\partial n_i}\left(\bar{A} - \bar{A}^{\circ}\right)_{T,\bar{V},n_{j\neq i}} . \tag{3.74}$$

In the above equation, superscript ° denotes a reference state, and *A* is the Helmoltz energy. Therefore, using Eq. (3.70) and the definition of fugacity coefficient, the above equation leads to

$$RT\ln\hat{\phi}_i = \int_{\bar{V}}^{\infty}\left[\left(\frac{\partial P}{\partial n_i}\right)_{T,\bar{V},n_{j\neq i}} - \frac{RT}{\bar{V}}\right]d\bar{V} - RT\ln Z\,, \tag{3.75}$$

where Z is the compressibility factor defined as

$$Z = \frac{PV}{RT}\,. \tag{3.76}$$

It can be seen from Eq. (3.75) that, to obtain the fugacity coefficient, the partial derivative of pressure with respect to the number of moles of each component needs to be calculated. This partial derivative can only be calculated by using an equation of state which provides the relation between the number of moles of the components and pressure. In this study, two-parameter cubic equations of state are used. Two-parameter cubic equations of state can be written in a general form as

$$P = \frac{NRT}{\bar{V} - Nb} - \frac{N^2 a}{\bar{V}^2 + ubN\bar{V} + wN^2 b^2}\,. \tag{3.77}$$

In the above equation, u and w are the unique constants of each equation of state. a and b are parameters determined both by temperature and critical properties. The values of the constants and formulations of the parameters for four different two-parameter cubic equations of state are listed in Table 3.1. Using the definition of compressibility factor, the above equation can be converted to a cubic function of compressibility factor as

$$Z^3 - \left(1 + B^* - uB^*\right)Z^2 + \left(A^* + wB^{*2} - uB^* - uB^{*2}\right)Z - A^*B^* - wB^{*2} - wB^{*3} = 0\,, \tag{3.78}$$

where $A^*=aP/R^2T^2$ and $B^*=bP/RT$. The above cubic function of compressibility factor usually has three real roots. The smallest root is the compressibility factor of the liquid phase, and the largest root serves as the compressibility factor for the vapor phase.

Table 3.1 Parameters of cubic equations of state

Equation	*u*	*w*	*b*	*a*
van der Waals	0	0	$\frac{RT_c}{P_c}$	$\frac{27}{64}\frac{R^2T_c^2}{P_c}$
Redlich-Kwang	1	0	$\frac{0.08664RT_c}{P_c}$	$\frac{0.4278R^2T_c^2}{P_cT^{1/2}}$
Soave	1	0	$\frac{0.08664RT_c}{P_c}$	$\frac{0.42748R^2T_c^2}{P_c}\left[1+f_\omega\left(1-T_r^{1/2}\right)\right]^2$ $f_\omega = 0.48+1.574\omega-0.176\omega^2$
Peng-Robinson	2	-1	$\frac{0.07780RT_c}{P_c}$	$\frac{0.45724R^2T_c^2}{P_c}\left[1+f_\omega\left(1-T_r^{1/2}\right)\right]^2$ $f_\omega = 0.3764+1.54226\omega-0.26992\omega^2$

Previous studies (Curtis and Farrell, 1992; Jia and Gogos, 1993; Zhu and Aggarwal, 2000) show that Peng-Robinson Equation of state can achieve the best accuracy in predicting the compressibility factor compared to other two-parameter equations of state. Therefore, it will mainly be used in this study. The calculation of fugacity of species in a mixture involves the assumption of one-fluid theory that the cubic equations of state are applicable to a mixture in the same way as to a pure component. Thus, to apply the cubic equations of state for a mixture, the mean values of *a* and *b* for the mixture must be known beforehand. In this study, the following mixing rule is used, namely,

$$a_m = \sum_i \sum_j Y_i Y_j (a_i a_j)^{1/2} \left(1-\bar{k}_{ij}\right) \tag{3.79}$$

and

$$b_m = \sum_i Y_i b_i \ . \tag{3.80}$$

In Eq. (3.79), $\bar{k}_{ij}$ is the binary interaction coefficient between *i* and *j*, and the values can be found for some component pairs, and for some hydrocarbon pairs without known values, it is

taken to be zero. Using the above two mixing rules and the equation of state, the fugacity coefficient can be calculated according to Eq. (3.75) as

$$\ln\hat{\phi}_i = \frac{b_i}{b}(Z-1) - \ln\left(Z - \frac{bP}{RT}\right) + \frac{a}{bRT\sqrt{u^2-4w}}\left(\frac{b_i}{b} - \delta_i\right)\ln\frac{2v+b\left(u+\sqrt{u^2-4w}\right)}{2v+b\left(u-\sqrt{u^2-4w}\right)}, \tag{3.81}$$

where δ_i is defined as

$$\delta_i = \frac{2a_i^{1/2}}{a}\sum_j X_j a_j^{1/2}\left(1-\bar{k}_{ij}\right). \tag{3.82}$$

Note that since the equation of state is applicable for both liquid and vapor phases, Eq. (3.81) is valid for calculating the fugacity coefficient of a component in a mixture for both phases. The value of compressibility factor used in Eq. (3.81) is selected as the root of the cubic function Eq. (3.78) corresponding to each phase as discussed above.

To model the drop vaporization of petroleum fuels under high-pressure conditions, the multicomponent vaporization model using continuous thermodynamics based on Raoult's law, which is discussed in Section 3.1, needs to be extended to high-pressure conditions by combining the general phase equilibrium with continuous thermodynamics. If the molecular weight distribution of the multicomponent fuel is described by a distribution function $f(I)$, phase equilibrium holds for the continuous distributed components. Using Eq. (3.14), for every component, the phase equilibrium described by Eq. (3.73) can be written as

$$Y_F f^v(I)\hat{\phi}_F^v(I) = X_F f^l(I)\hat{\phi}_F^l(I). \tag{3.83}$$

Therefore, the mole fraction of the multicomponent fuel at the phase interface can be calculated using the following integration:

$$Y_F = \int_\gamma^\infty Y_F f^v(I)dI = \int_\gamma^\infty X_F \frac{\hat{\phi}_F^l(I)}{\hat{\phi}_F^v(I)} f^l(I)dI. \tag{3.84}$$

The first moment of the fuel vapor at the phase interface can be calculated by multiplying molecular weight on both sides of Eq. (3.83) and integrating, i.e.,

$$Y_F \theta_v = \int_\gamma^\infty Y_F f^v(I) I dI = \int_\gamma^\infty X_F \frac{\hat{\phi}_F^l(I)}{\hat{\phi}_F^v(I)} f^l(I) I dI \,. \tag{3.85}$$

Similarly, the second moment can be calculated as

$$Y_F \Psi_v = \int_\gamma^\infty Y_F f^v(I) I^2 dI = \int_\gamma^\infty X_F \frac{\hat{\phi}_F^l(I)}{\hat{\phi}_F^v(I)} f^l(I) I^2 dI \,. \tag{3.86}$$

The above three equations are required for the calculation of drop vaporization rate for a multicomponent fuel modeled based on continuous thermodynamics. It can be seen from the above equations that the fugacity coefficient as a function of molecular weight must be known. In this study, the methods for calculating fugacity coefficient using the cubic equations of state are still used. The equation of state is applicable for the multicomponent fuel with the mean values of parameters *a* and *b*. In this study, the mean values are calculated using the following equations which are similar with the mixing rules described by Eqs. (3.79) and (3.80), namely,

$$a_m = \left(\int_\gamma^\infty a^{1/2}(I) f(I) dI \right)^2 \tag{3.87}$$

and

$$b_m = \int_\gamma^\infty b(I) f(I) dI \,. \tag{3.88}$$

It can be seen from the above two equations that *a* and *b* need to be correlated with molecular weight. In this study, the square root of *a* and *b* for Peng-Robinson equation of state are linearly correlated with molecular weight using the critical properties of C2-C20 alkanes according to Table 3.1 as

$$a^{1/2}(I,T) = \left(115.65559 - 2.54784 T^{1/2}\right) \times I - 363.60516 + 24.04255 \times T^{1/2} \tag{3.89}$$

and

$$b(I) = 1.62213 \times I - 25.52276 \,. \tag{3.90}$$

Using the continuous mixing rule described by Eqs. (3.87) and (3.88) to obtain the mean parameters for the equation of state, the logarithmic fugacity coefficient as a function of molecular weight is finally derived according to Eq. (3.75) as

$$\ln\hat{\phi}(I)=\ln\left(\frac{v}{v-b}\right)+\frac{a}{RTb\sqrt{u^2-4w}}\left(\frac{b(I)}{b}-\frac{2a^{1/2}(I)}{a^{1/2}}\right)\ln\frac{2v+b\left(u+\sqrt{u^2-4w}\right)}{2v+b\left(u-\sqrt{u^2-4w}\right)}. \\ +\frac{b(I)}{b}(Z-1)-\ln Z \tag{3.91}$$

It can be seen from the above equation that the logarithmic fugacity coefficient is a linear function of the molecular weight and can be written into the following generalized form:

$$\ln\hat{\phi}(I)=AI+B, \tag{3.92}$$

where A and B are determined by temperature, pressure, and composition but not related to molecular weight. If the molecular weight distribution of the multicomponent fuel is described by a gamma distribution as shown in Eq. (3.1), with the fugacity coefficient as a function of molecular weight generalized in the above equation, the integration in Eq. (3.84) will lead to the mole fraction of fuel vapor at drop surface as

$$Y_p=\frac{X_p\exp\left[\gamma\left(A_l-A_v\right)+\left(B_l-B_v\right)\right]}{\left[1-\beta_l\left(A_l-A_v\right)\right]^{\alpha_l}}. \tag{3.93}$$

Similarly, the first and second moments of the molecular weight distribution of fuel vapor at drop surface and be calculated with integrations defined in Eqs. (3.85) and (3.86) as

$$\theta_{v,R}=\gamma-\frac{\beta_l\Gamma\left(\alpha_l+1\right)}{\left[\beta_l\left(A_l-A_v\right)-1\right]\Gamma\left(\alpha_l\right)} \tag{3.94}$$

and

$$\Psi_{v,R}=2\theta_{v,R}\gamma-\gamma^2+\frac{\beta_l^2\Gamma\left(\alpha_l+2\right)}{\left[\beta_l\left(A_l-A_v\right)-1\right]^2\Gamma\left(\alpha_l\right)}. \tag{3.95}$$

Note that the above expressions for the first and second moments are actually implicit. Since the compressibility factor involved in A_v and B_v is also determined by the fuel vapor

molecular weight distribution. Therefore, additional iterations are necessary in the calculation of the moments of fuel vapor at drop surface.

Moreover, enthalpy of vaporization determines the amount of heat required for the vaporizing liquid fuel mass and therefore has a significant effect on the drop heating rate. In a liquid-vapor system composed of multiple components, the enthalpy of vaporization for a component is the difference of partial molar enthalpy in both phases as

$$\Delta h_{vap,i} = h_{i,v}\left(T,P,Y_i\right) - h_{i,l}\left(T,P,X_i\right). \tag{3.96}$$

Under low pressure conditions, the enthalpy of vaporization of a component in a mixture can be approximated by the latent heat which is the enthalpy difference in liquid and vapor phases in an environment composed of the pure component. However, under high-pressure conditions, the error of such an approximation cannot be neglected since the assumption of ideal mixture is not valid. Therefore, the deviation of the behavior of a real fluid mixture from an ideal mixture needs to be considered. To estimate the partial molar enthalpy of component *i*, the chemical potential determined by the following relation is used, i.e.,

$$\mu_i = h_i - Ts_i. \tag{3.97}$$

In the above equation, h_i and s_i are the partial molar enthalpy and entropy, respectively, at constant temperature and pressure. With the definition of fugacity (Eq. (3.70)), it can be shown that the partial molar enthalpy for species *i* in a mixture can be obtained using a departure function as (Zhu and Aggarwal, 2000)

$$h_i - h_i^{\circ} = -RT^2\left(\frac{\partial\left(\ln\hat{\phi}_i\right)}{\partial T}\right)_{P,Y_i}, \tag{3.98}$$

where ° denotes an ideal state with very low pressure at the same temperature. At this ideal state, the partial molar enthalpy is equal to the molar enthalpy of that pure component. Finally, the enthalpy of vaporization of a species in a mixture under high-pressure conditions can be concluded as

$$\Delta h_{vap,i} = RT^2 \left(\frac{\partial \left(\ln \hat{\phi}_{i,l} \right)}{\partial T} \right)_{P,X_i} - RT^2 \left(\frac{\partial \left(\ln \hat{\phi}_{i,v} \right)}{\partial T} \right)_{P,Y_i} . \tag{3.99}$$

It can be seen from the above equation that the enthalpy of vaporization of a component will be dependent on all the components that make up the two-phase system. At the critical mixing point discussed in the previous section, the enthalpy of vaporization will be zero since there is no phase difference in the system at this point.

Under high-pressure conditions, the estimation of some of the physical properties needs to consider the effect of high pressure. In this study, rather than using an equation of state to predict the liquid phase density, the Hankinson-Brobst-Thomson (HBT) technique, which is a two-step correlation, is used to calculate liquid density at elevated pressures. To consider the effect of pressure on liquid density using HBT technique, the first step is to estimate the saturated liquid density as

$$\frac{V_s}{V^*} = V_R^{(0)} \left[1 - \omega_{SRK} V_R^{(\delta)} \right]. \tag{3.100}$$

where

$$V_R^{(0)} = 1 + a\left(1 - T_r\right)^{1/3} + b\left(1 - T_r\right)^{2/3} + c\left(1 - T_r\right) + d\left(1 - T_r\right)^{4/3}, 0.25 < T_r < 0.95 \tag{3.101}$$

and

$$V_R^{(\delta)} = e + fT_r + gT_r^2 + hT_r^2, 0.25 < T_r < 1.0 . \tag{3.102}$$

In Eq. (3.100), ω_{SRK} is the acentric factor which forces the Soave equation to give a best fit of existing vapor pressure data (Reid et al., 1987). V^* is a pure component characteristic volume generally within 1 to 4 percent of the critical volume, and a~h are constants. The second step further corrects the density of saturated liquid to the compressed values with the technique by Thomson et al. (1982), i.e.,

$$V = V_s \left(1 - c \ln \frac{\beta + P}{\beta + P_{vp}} \right). \tag{3.103}$$

In the above equation, β is a function of temperature, and c is a constant determined by ω_{SRK}. In addition, the gas phase mass diffusion coefficient is first estimated using Fuller's equation (Reid et al., 1989) which is only applicable for low pressure conditions and further corrected with Takahashi's correlation for high-pressure conditions (Takahashi, 1974). For the liquid phase, the mass diffusivity can be first estimated as the value at infinite dilution using Tyn and Calus' method and corrected using the infinite dilution values according to the composition of the binary mixture (Reid et al., 1989).

3.4 Baseline CFD Code

The above high-pressure vaporization model were implemented into a baseline CFD code. In this study, KIVA-3v Release 2, which is a transient, three-dimensional, multiphase code for the analysis of chemically reacting flows with sprays, is used as the baseline code. The multicomponent vaporization models in the above sections were implemented into the code to replace the original single-component vaporization model. Drop vaporization calculation is coupled with species conservation equation by the strategy that the vaporizing fuel component contributes to the cell average mass of the component in the computational cell where the drop is located. The turbulent flow was modeled using the RNG k-ε turbulence model. Fuel spray was simulated by an updated spray model considering the instability of the surface wave leading to drop breakup (Kong et al., 1999).

KIVA uses three phases of calculations, i.e., Phases A, B, and C. The fuel spray calculation including drop motion and vaporization, which provides the source terms of the governing equations, is performed in phase A. Phase B calculates the governing equation based on finite volume approach to obtain the time-accurate solution with a method similar to the SIMPLE scheme. Phase C is a rezone phase evaluating the convective transport associated with the motion of the mesh relative to the fluid. Quasi-second-order upwind (QSOU) and partial donor cell (PDC) methods are used as the convection schemes. In phase A, the velocity of drops is described by the implicit scheme, i.e.,

$$\frac{v_p^t - v_p'}{\Delta t} = D_p \cdot \left(u_{ijk}^n + u_p' - v_p^t \right). \tag{3.104}$$

In the above equation, v_p is the drop velocity with superscript t indicating the velocity updated with drag effect, and the prime indicating the velocity before updating the effect of drag force. D_p is the drag function defined with the relative velocity between the drop and its ambient gas, namely,

$$D_p = \frac{3}{8}\frac{\rho_{ijk}^n}{\rho_d}\frac{\left|u_{ijk}^n + u_p' - v_p^t\right|}{r_p^A}C_D . \tag{3.105}$$

Subscript ijk indicates the computational cell where the drop is currently located. u_p' is the gas turbulent velocity. C_D is the drag coefficient as a function of Reynolds number, i.e.,

$$C_D = \begin{cases} \dfrac{24}{Re_d}\left(1+\dfrac{1}{6}Re_d^{2/3}\right), & Re_d < 1000 \\ 0.424, & Re_d > 1000 \end{cases} . \tag{3.106}$$

Re_d is the Reynolds number defined with relative velocity between the drop and its ambient gas:

$$Re_d = \frac{2\rho\left|u + u' - v\right| r}{\mu_{air}\left(\hat{T}\right)} . \tag{3.107}$$

The Reynolds number is also used in Eqs. (2.38) and (2.45) for the calculations of Nusselt and Sherwood numbers. The viscosity in the above qeuation is evaluated at a temperature determined by the one-third law using ambient temperature and drop (surface) temperature, i.e.,

$$\hat{T} = \frac{T + 2T_d}{3} . \tag{3.108}$$

Despite that the multicomponent effect was considered in modeling vaporization, all the fuel vapor was lumped into the “fuel species” in the combustion simulation. Since n-heptane and diesel fuel have similar ignition and combustion characteristics, n-heptane mechanisms are widely used to simulate diesel fuel oxidation (Flynn et al., 1999; Hasse and Peters, 2004; Zhang et al., 2004). This study also used an n-heptane reaction mechanism consisting of 30 species and 65 reactions that are appropriate for integration with three-dimensional engine

modeling (Patel et al., 2004). In the present study, the chemical reactions were solved by the CHEMKIN chemistry solver that was integrated into the KIVA code.

Consistent with the finite volume numerical scheme of KIVA, the reactive mixture in each grid cell is treated as a closed system, and the rate of change of species mass fraction is calculated as

$$\frac{dy_k}{dt} = v\dot{\omega}_k W_k , \tag{3.109}$$

where v is the specific volume, $\dot{\omega}_k$ and W_k are the production rate and the molecular weight of species k, respectively. The energy equation to determine the gas phase temperature is formulated on the constant-volume basis, i.e.,

$$C_v \frac{dT}{dt} + v\sum_{k=1}^{K} e_k \omega_k W_k = 0 , \tag{3.110}$$

where C_v is the mean specific heat of the mixture and e_k is the internal energy of species k.

In addition, soot emissions were simulated using a phenomenological soot model which considers both soot formation and oxidation processes as shown in Eq. (3.111) (Han et al., 1996). In this equation, the net soot emission rate is the difference between the formation rate, which is calculated using an Arrhenius expression shown in Eq. (3.112), and the oxidation rate. In calculating the soot formation rate, acetylene (C_2H_2) was selected as the inception species due to its strong relevance to soot formation. The soot oxidation rate was determined using the Nagle-Strickland-Constable model that considers carbon oxidation by two different reaction pathways as shown in Eq. (3.113).

$$\dot{M}_s = \dot{M}_{sf} - \dot{M}_{so} \tag{3.111}$$

$$\dot{M}_{sf} = A_{sf} M_{C_2H_2} p^n \exp\left(-\frac{E_{sf}}{RT}\right) \tag{3.112}$$

$$\dot{M}_{so} = \frac{6Mw_c}{\rho_s D_s} M_s R_{Total} \tag{3.113}$$

CHAPTER 4 VAPORIZATION MODELING OF PETROLEUM FUEL AND BIOFUEL MIXTURE

Continuous thermodynamics is a vaporization approach ideal for complex fuels such as diesel fuel and gasoline which are composed of hundreds of hydrocarbon species. Using this approach, the composition of the fuel is modeled by a continuous function which determines the distributions of the molecular weights of the species in the fuel. In this chapter, continuous thermodynamics based on a gamma distribution is used to simulate the vaporization of diesel fuel and gasoline. The vaporization model was also used in a combustion simulation in a constant-volume chamber. Soot distribution was predicted and compared with experimental data for model validation.

On the other hand, biodiesel is a bio-renewable fuel, which has close physical and chemical properties with diesel fuel, and can be used in diesel engines without significant modification to the engine. In contrary to diesel fuel, which is composed of hundreds hydrocarbons, biodiesel is a multicomponent fuel composed of only a few components. Therefore, in this chapter, the vaporization of biodiesel drops was modeled using the biodiesel vaporization model and a discrete component approach. Both approaches are based on its major components. The physical properties of biodiesel components will be predicted using the methods in Sec. 3.2. Since in practical application, biodiesel is blended with diesel fuel and ethanol is blended with gasoline, the vaporization results of the petroleum-biofuel mixture will also be presented.

4.1 Validation of Vaporization Model

In this study, the vaporization model derived from pseudo-steady vapor phase species conservation equation was first applied to simulate single component fuels and binary fuel mixtures. The experimental vaporization histories of n-heptane (n-C_7H_{16}) drops by Nomura et al. (1996) were used for model validation. In the experiment, a stagnant pure n-heptane drop was generated and suspended in pure nitrogen environments of different temperatures. Cases with ambient pressure 1 bar and ambient temperatures 471 K, 555 K, and 648 K were simulated to compare with experimental data. Simulation results in the drop size history are plotted with experimental data as shown in Figure 4.1. It can be seen that good levels of

agreement are obtained for different ambient conditions. The good agreement indicates that the present vaporization model performs well for single-component drops. Figure 4.2 shows the corresponding drop temperature histories of the above three cases. It can be seen that for all the three cases, drop temperature increases quickly at the beginning and the drop start to vaporize at a constant temperature after a period of time. The constant drop temperature indicates zero drop heating rate described in the heat balance equation Eq. (2.26). Or in other words, the amount of heat transferred to the drop surface is all used for the vaporization latent heat. It can also be seen from the figure that for higher ambient temperature, the balance drop temperature will be higher.

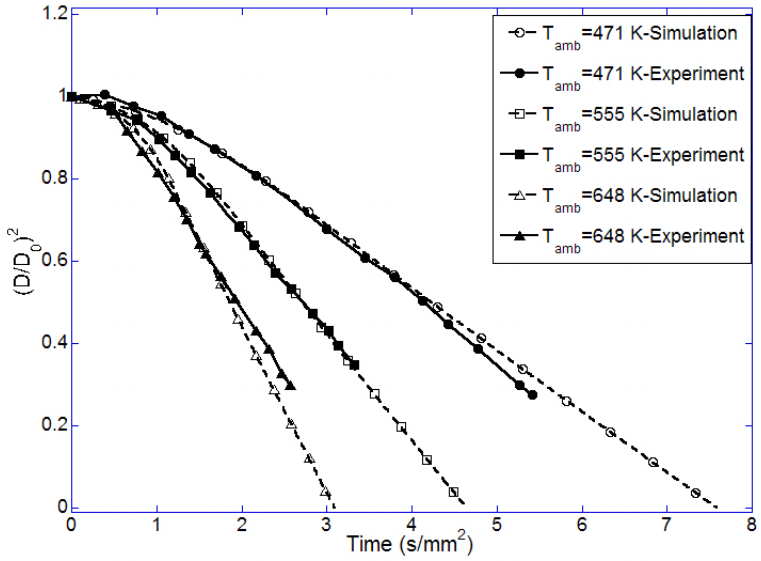

Figure 4.1 Vaporization histories of single n-heptane drops under different ambient temperatures at P_{amb}=1 bar

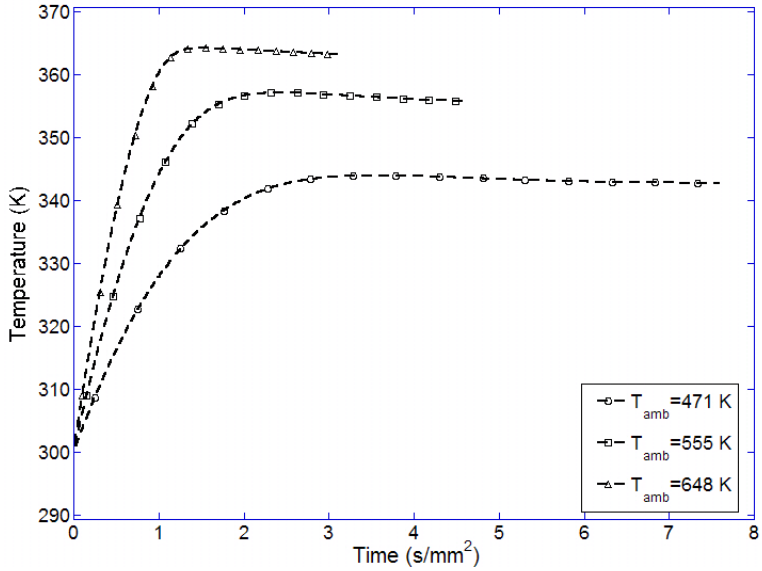

Figure 4.2 Temperature histories of single n-heptane drops under different ambient temperatures at P_{amb}=1 bar

The discrete vaporization model (Eq. (3.45)) was further applied to drops blended by two different fuels. Modeling the vaporization of drops that are blends of two different fuels involves the vaporization rate calculation of each fuel, and is therefore more complicated than vaporization modeling of single-component drops. According to the discussion in Sec. 2.2, the temperature and concentration distributions are assumed to be quadratic functions of the distance from drop center. To further validate the present vaporization model, vaporization experiments of n-heptane/n-decane (n-C_7H_{16}/n-$C_{10}H_{22}$) mixtures by Gökalp et al. (1994) were simulated. In the experiment, a drop was introduced into an environment that had a heated air inflow at 1.45 m/s, 372 K and 1 bar. Two different drop compositions were used, including 20% n-heptane/80% n-decane and 80% n-heptane/20% n-decane by volume. Since n-heptane has a lower boiling temperature than n-decane, it is expected that a drop with more n-heptane will have a shorter lifetime. The predicted drop size histories are compared with experimental data as shown in Figure 4.3. It can be seen that the model is able to predict the effects of composition on vaporization history and drop lifetime. The predicted drop size history has the same trend as the experiments, i.e., similar shapes of the curves, for both conditions despite that there are noticeable differences in the overall lifetimes. It should be noted that the liquid and vapor properties are those described in Reid et al. (1987), and the same model constants and formulation are used for all the cases in this study, including those

in the later sections. It is also worth noting that Ra and Reitz (2009) also predicted shorter drop lifetimes for the same cases. Thus, the level of agreement in Figure 4.3 is thought to be reasonable.

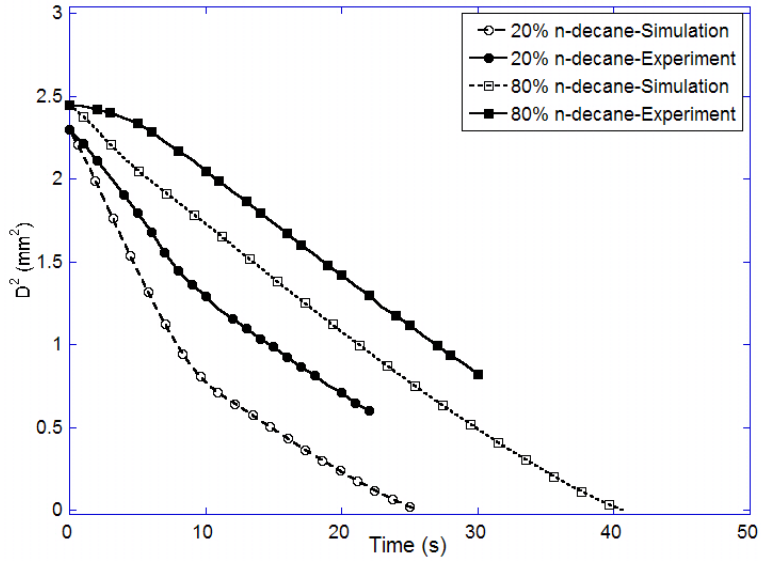

Figure 4.3 Vaporization histories of binary-component drops of n-heptane and n-decane with different compositions at T_{amb}=372 K , P_{amb}=1 bar, and V_{amb}=1.45 m/s

For the case of 20% n-decane, the drop size D^2-curve bends at a point in time during the vaporization process. The D_2-curve initially has a steeper shape, and after 10 seconds, the slope decreases noticeably. The second part of the curve has a slope similar to that of the 80% n-decane curve. The bending of the D^2-curve indicates an evident decrease in the drop vaporization rate due to the significant variation in composition during the vaporization process. It is believed that n-heptane vaporizes earlier during the process due to its higher volatility while most of n-decane remains in the liquid phase. The above observation is supported by the volume fraction history of n-decane shown in Figure 4.4. It can be seen that the volume fraction of n-decane increases at the beginning and reaches unity at some point in time. For instance, in the case of 20% n-decane, the volume fraction of n-decane increases rapidly and reaches unity after 11 seconds, after which only n-decane is left in the drop. On the other hand, in the case of 80% n-decane, all the n-heptane in the drop has vaporized in about 6 seconds.

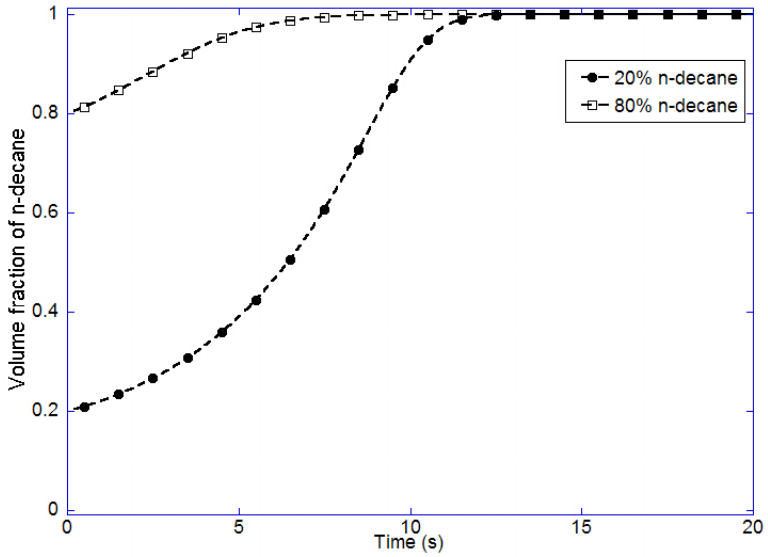

Figure 4.4 Histories for the volume fraction of n-decane in the liquid phase for both initial compositions at T_{amb}=372 K, P_{amb}=1 bar, V_{amb}=1.45 m/s

4.2 Petroleum Fuel Vaporization Modeling

To study the vaporization behavior of petroleum fuels, the present multicomponent model based on continuous thermodynamics described in Sec. 3.1 was applied to simulate the vaporization of a single drop in quiescent conditions. The traditional single-component model was also applied to the same cases for comparison. The drop has an initial size of 100 micron in diameter with an initial temperature of 300 K. Both diesel and gasoline drops were simulated to test the applicability of the model for different fuels. The initial ambient temperature and pressure are 973 K and 1 atm, respectively, and combustion model is disabled in KIVA. For the diesel drop, the parameters in the gamma distribution function (Eq. (3.1)) are α=23, β=8.15 and γ=0 initially, and for the gasoline drop, α=5.7, β=15 and γ=0. Those parameters were selected to match the distillation curves of specific fuels (Tamim and Hallett, 1995). Results of the drop size and mean molecular weight evolutions are shown in Figure 4.5 and Figure 4.6. It can be seen that during vaporization, the mean molecular weight of the liquid drop keeps increasing during the vaporization process. This phenomenon indicates a vaporization sequence of components according to their molecular weights, i.e., lighter components vaporize earlier. In addition, it is worth noting that the rate of increase of

the mean molecular weight becomes very large near the end of vaporization when the drop is very small.

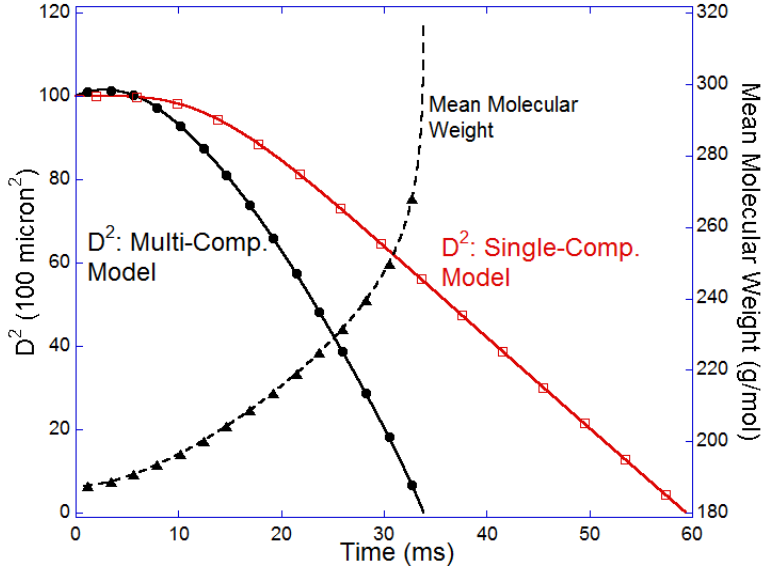

Figure 4.5 Histories of the drop size and the mean molecular weight of a single diesel drop for T_{amb}=973 K at atmospheric pressure

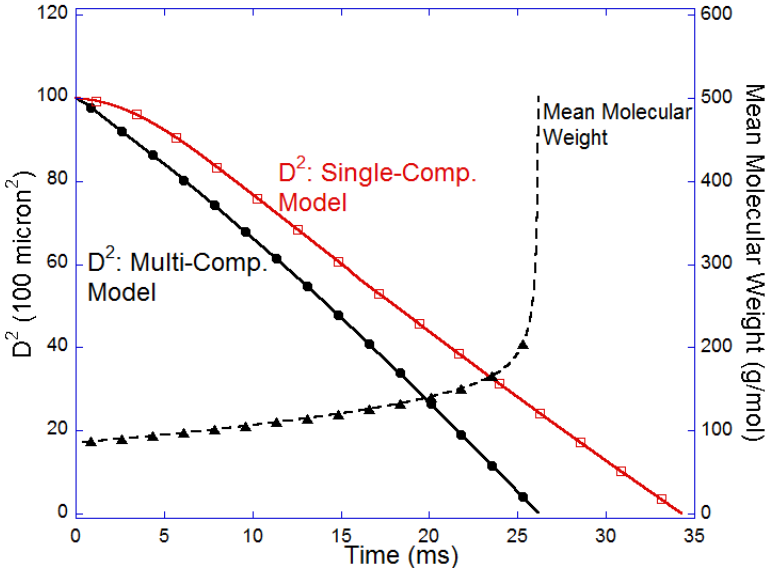

Figure 4.6 Histories of the drop size and the mean molecular weight of a single gasoline drop for T_{amb}=973 K at atmospheric pressure

As can be seen from the drop surface recession curves in the above two figures, the present multicomponent model predicts different vaporization behaviors for both fuels. For the diesel drop, due to the high concentration of heavy components, the mole fraction of

diesel fuel at drop surface is relatively low at low temperatures. This leads to the small vaporization mass flux at the beginning and a slight expansion due to ambient heating. The vaporization rate of the drop becomes large because of the increasing drop temperature. In the contrary, gasoline fuel has a relatively higher volatility which makes the drop have a large vaporization rate as soon as the drop is exposed to high temperature. Therefore, the gasoline drop size decreases monotonically without a heating and dilation effect at the beginning.

For comparison, drop vaporization in the same condition was also simulated using a single-component approach, in which diesel was modeled using tetradecane ($C_{14}H_{30}$) and gasoline using iso-octane (i-C_8H_{18}). Compared to the single-component approach, the multicomponent model predicts shorter drop lifetime for the same case. This is due to the vaporization sequence of components determined by their molecular weights. Low molecular weight components vaporize earlier because of their relatively higher vapor pressure. Therefore, the multicomponent drop is more liable to vaporize than single component drop and consequently has relatively larger vaporization mass flux. It is noted that experimental data are not available for validation. Nonetheless, the numerical results indicate that different modeling approaches clearly lead to different vaporization histories.

Figure 4.7 and Figure 4.8 show the evolutions of the molecular weight distributions for both diesel and gasoline drops during vaporization. It can be seen that the molecular weight distribution curves move toward the high molecular weight direction during the vaporization process, indicating that the lighter components vaporize earlier in the process and thus the mole fractions of heavy components increase. The results of the predicted molecular weight distribution evolutions are consistent with the mean molecular weight history shown in Figure 4.5 and Figure 4.6.

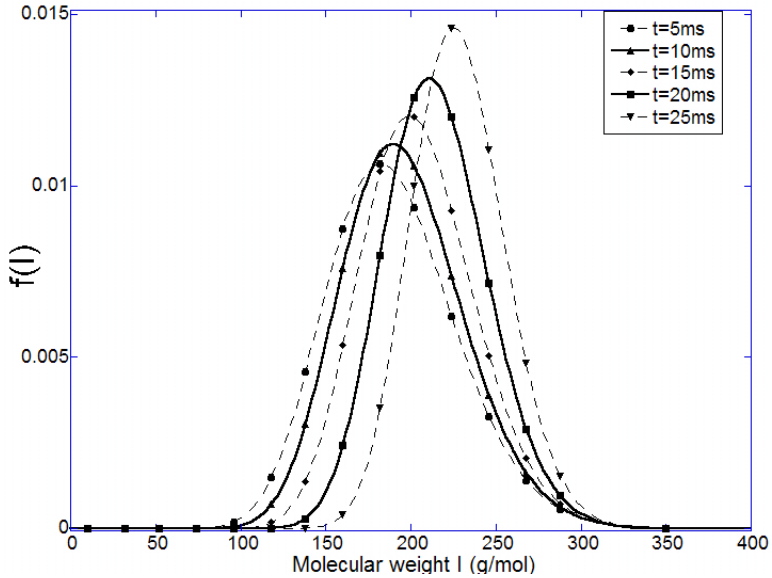

Figure 4.7 Distribution curves for the diesel drop at different times

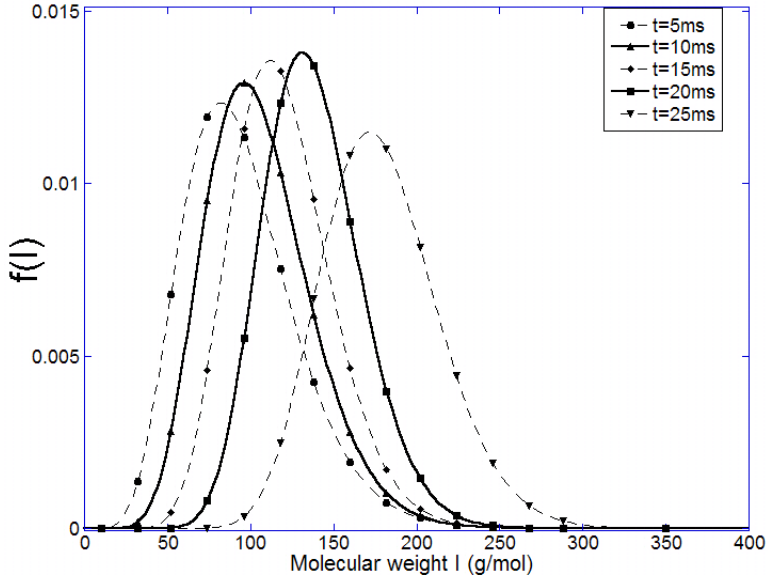

Figure 4.8 Distribution curves for the gasoline drop at different times

The present on continuous thermodynamics vaporization model was also applied to simulate diesel spray combustion and soot emissions in a constant-volume combustion chamber. Experimental results by Pickett and Siebers (2004) were used for model validation. The combustion chamber was modeled using a cylindrical mesh with a height of 10 cm and a diameter of 12.5 cm. The mesh has 32 cells in the radial direction and 50 cells in the axial direction. The injector orifice is located at the center of the top surface with an injection

pressure of 138 MPa. Experimental cases using the 100 μm diameter injector were simulated. The ambient air density is 14.8 kg/m^3, but pressure and temperature vary for different cases.

The computational code was first used to simulate diesel spray dynamics and vaporization without activating the chemistry model. The purpose was to investigate the diesel spray structure and liquid molecular weight distribution predicted by the present multicomponent vaporization model. Figure 4.9 shows the liquid drop distribution with the drops colored by their mean molecular weights at two different times. It can be seen that the drops in the outer region and the tip of the spray have relatively large molecular weights than those in the center region. This phenomenon is due to the fact that the lighter components vaporize earlier in the process and surviving drops have heavier components as they penetrate to the outer region of the spray. Additionally, there are more drops with larger mean molecular weight at a later time (e.g., 3.2 ms after start of injection (ASI)). Figure 4.9 qualitatively illustrates the spatial and temporal distributions of the high-velocity diesel spray predicted by the present model. The predicted results are thought to be reasonable despite that experimental data are not available at the same conditions for validation.

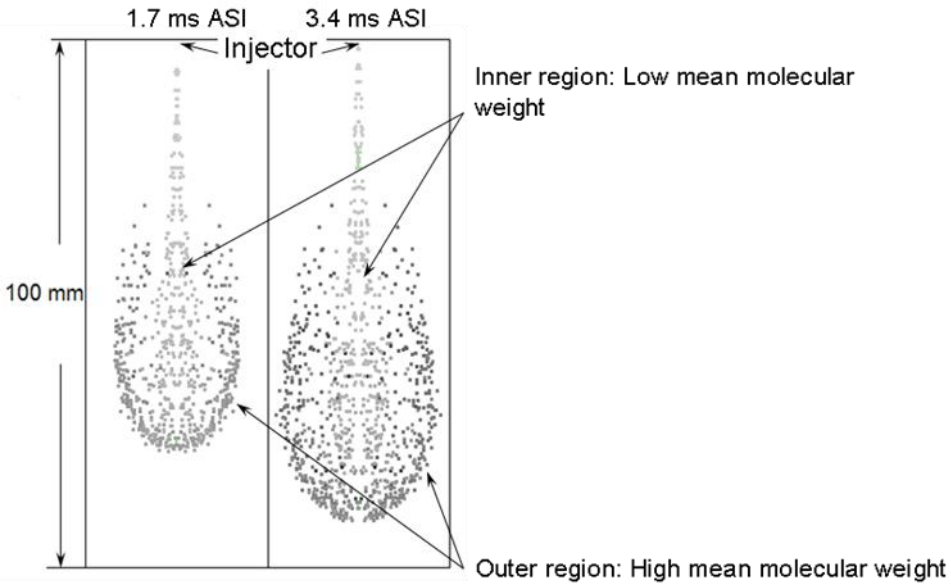

Figure 4.9 Distribution of drops and their mean molecular weight, T_{amb}=900 K, ρ_{amb}=14.8 kg/m^3

Combustion and emissions models were then activated in KIVA to simulate the spray combustion and soot distribution in the diesel spray. Predicted spray and temperature distributions are shown in Figure 4.10 at two different times. The ambient temperature and density are 900 K and 14.8 kg/m^3, respectively. Notice that a majority of liquid drops have vaporized in this case, which is a situation different from Figure 4.9. Models predicted that ignition occurred at the leading edge of the spray. In fact, gas temperature continues to rises prior to the ignition site indicating mild heat release resulting from pre-ignition chemical reactions in this region. The combusting spray developed into a standing diffusion flame with the lift-off location indicated by a dotted line in the figure. The predicted flame structure is similar to that described by experimental results (Dec, 1997). It is of interest to note that the liquid penetration in the combustion case is much shorter than that in Figure 4.9 where the combustion model is not activated. It is believed that the high combustion temperature has a significant effect in enhancing vaporization.

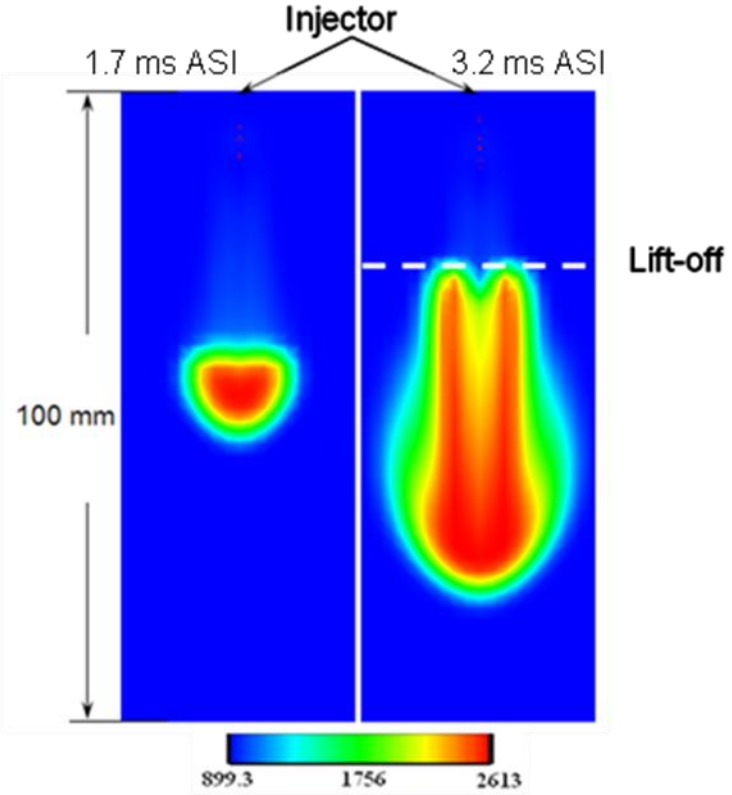

Figure 4.10 Temperature distributions of combusting diesel spray, T_{amb}=900K, ρ_{amb}=14.8kg/m^3

Predicted soot distributions were also compared with experimental results as shown in Figure 4.11. Experimental results shown in Figure 4.11 (a) are planar laser-induced incandescence (PLII) images of soot on a thin plane along the spray axis. The images mainly indicate the instantaneous areas where soot is present. Numerical results in Figure 4.11 (b) are predicted soot mass fraction distributions. Both experimental and numerical results shown in Figure 4.11 are those at 3.2 ms after start of injection for ambient density of 14.8 kg/m^3. Three different initial ambient temperatures were simulated. The dotted white lines also indicate the lift-off locations obtained from experiments and simulation. Notice that the color scheme for numerical results was adjusted such that predicted soot emissions were negligible for soot mass fraction less that 10^{-5}. The same criterion has been used to determine the predicted sooting limit using a single-component vaporization model (Kong, et al., 2007).

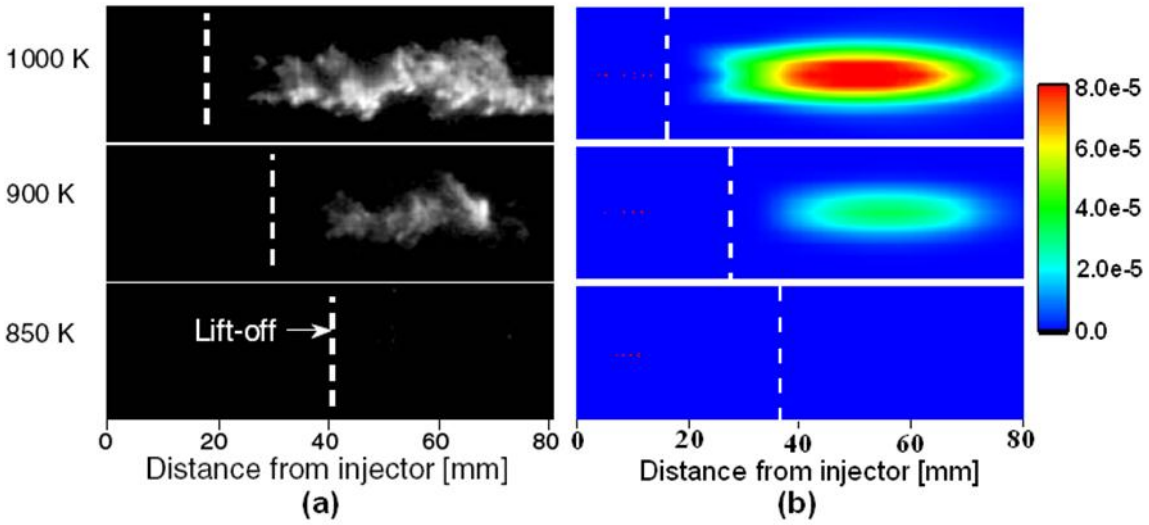

Figure 4.11 Comparisons of experimental soot images and predicted soot mass fraction distributions at the central plane of the fuel jet at 3.2 ms after injection for different ambient temperatures with the same ambient density

It can be seen from the comparison that the predicted lift-off lengths are close to the experimental results and the predicted soot areas agree with those captured by PLII images. The model predicts the correct trend in soot emissions with respect to ambient temperatures. The soot emission history curves in Figure 4.12 indicate that the amount of soot in the combustion chamber reduces as the ambient temperature decreases from 1000 K to 850 K.

For the 850 K ambient temperature case, soot emissions were not observed in the experiment, and the model also predicted negligible soot emissions.

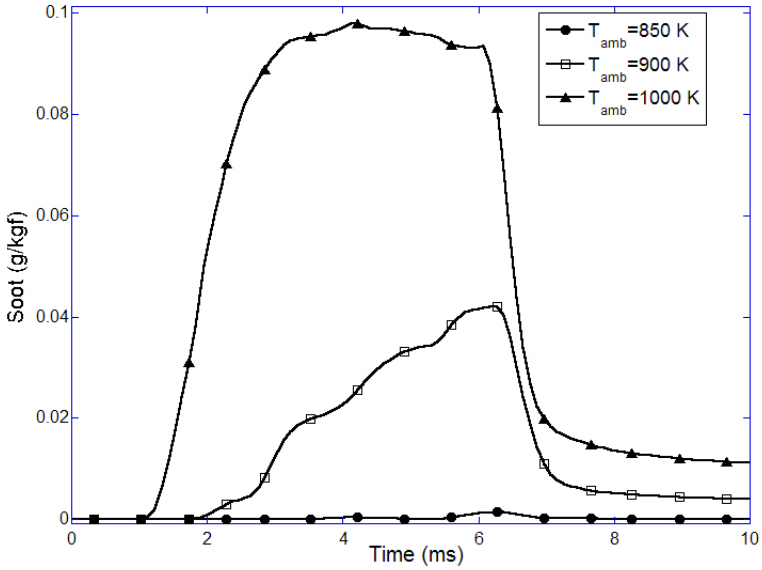

Figure 4.12 Soot history for different initial ambient temperatures at ρ_{amb}=14.8kg/m^3

For more detailed model validation, soot concentration distributions along the spray axis were also compared between experimental and numerical results. Experimental results were obtained using laser techniques to measure the optical thickness of soot (KL factor) in the radial direction of the spray. The optical thickness of soot is proportional to the total amount of soot along the line of sight in the radial direction. On the other hand, the predicted soot mass along the radial direction was obtained by adding soot mass of each computational cell together. In order to compare with the experimental results of the optical thickness of soot, the cumulated soot mass was normalized by the maximum value along the spray axis. Similarly, the experimental KL factors were also normalized for qualitative comparison. Cases with initial temperatures of 950 K, 1000 K, 1100 K, and 1200 K were calculated, and the numerical and experimental results are shown in Figure 4.13. It can be seen that the predicted soot distributions agree with experimental results reasonably well. As can be seen in the soot distribution curves, soot is not observed in regions near the injector. Beyond the flame lift-off location, soot increased downstream and reached a peak where the mixture is rich and little oxygen is available. Then soot decreased toward the leading edge of the flame as soot is oxidized by ambient air that is diffused into the flame.

This study differs from previous work of Kong et al. (2007) by using a multicomponent vaporization model with detailed chemistry for diesel spray combustion modeling. The predicted flame structures and soot distributions agree with experimental results reasonably well. Results indicate that the present model is able to simulate the diesel spray vaporization process by considering the multicomponent effect. Despite that single-component vaporization models have also been used with success in various applications, it is anticipated that the present multicomponent vaporization model can provide more comprehensive simulation for conditions in which the fuel multicomponent effects are significant such as blends of petroleum fuels and biofuels. Additionally, more comprehensive integration of multicomponent vaporization model and detailed chemistry can be explored in future study to consider effects of fuel components on chemical reactions.

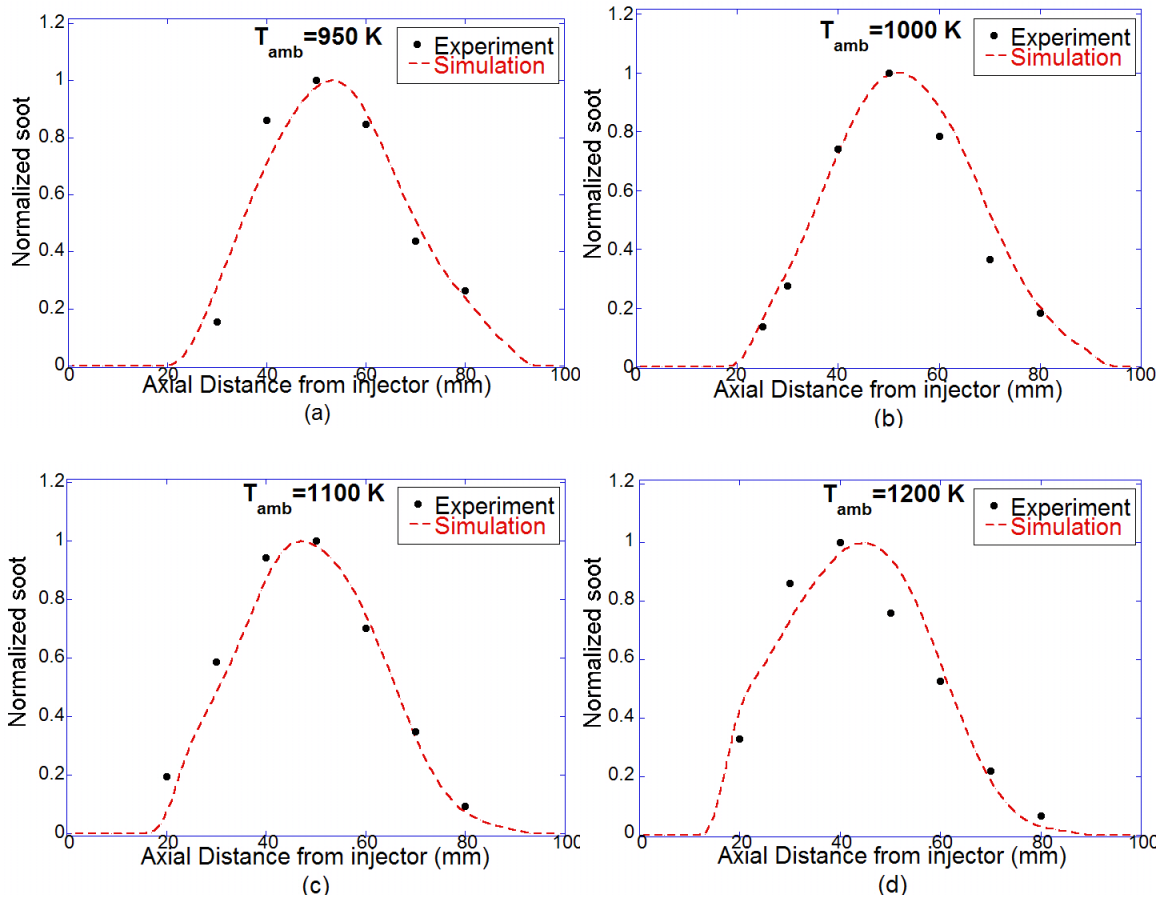

Figure 4.13 Comparisons of measured time-averaged *KL* factors and predicted soot mass for various ambient temperatures. Both measured and predicted data were normalized to allow qualitative comparison

4.3 Biodiesel Composition and Properties

Biodiesel is a renewable fuel that can be produced from vegetable oils, animal fat, or other biomass feedstock. Previous studies show that biodiesel derived from vegetable oils are mainly composed of five C16 to C18 fatty acids. Table 4.1 shows the mass fractions of components for biodiesel derived from rapeseed methyl ester (Ramadhas et al., 2005). It can be seen that more than 90% of biodiesel on mass basis is composed of the five components listed in the table. Therefore, in this study, biodiesel was modeled as an ideal mixture of the five components, and other minor components are neglected.

Table 4.1 Typical composition of biodiesel derived from rapeseed methyl ester

Component	Palmitic ($C_{16}H_{32}O_2$)	Stearic ($C_{18}H_{36}O_2$)	Oleic ($C_{18}H_{34}O_2$)	Linoleic ($C_{18}H_{32}O_2$)	Linolenic ($C_{18}H_{30}O_2$)	Others
y_{mass}	3.49%	0.85%	64.4%	22.3%	8.23%	0.73%

To model the vaporization of biodiesel, its physical properties such as vapor pressure and latent heat need to be estimated with correlations since no experimental data about its properties are available. The physical properties of biodiesel can be estimated with the correlations shown in Sec. 3.2 using its critical properties. The critical properties of biodiesel components are usually not known and can be estimated using atom group contribution methods with the normal boiling points of the five dominant components shown in Table 4.2.

Table 4.2 Normal boiling points of biodiesel components

Component	Palmitic ($C_{16}H_{32}O_2$)	Stearic ($C_{18}H_{36}O_2$)	Oleic ($C_{18}H_{34}O_2$)	Linoleic ($C_{18}H_{32}O_2$)	Linolenic ($C_{18}H_{30}O_2$)
T_b (K)	624.5	634.0	633.0	639.0	643.0

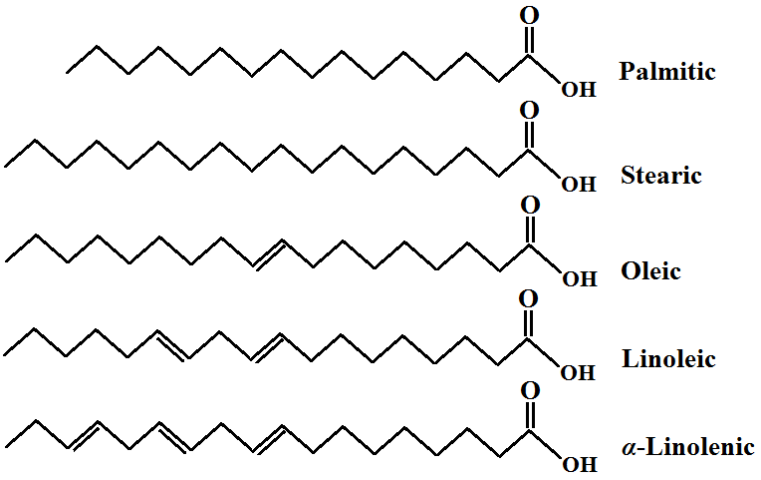

Figure 4.14 Molecular structures of biodiesel components

Using the Ambrose's atom group contribution method shown in Eqs. (3.59) and (3.60), the critical temperatures and volumes of biodiesel components can be estimated according to the molecular structures as shown in Figure 4.14. The resulting critical temperatures and volumes of biodiesel components are shown in Table 4.3. It can be seen that the components

of biodiesel have close critical properties due to the fact that the molecular structures of the components are similar as shown in Figure 4.14. The calculated vapor pressures of biodiesel components in the temperature range of 300~750 K are plotted in Figure 4.15. The curves show that the vapor pressures of biodiesel components are almost 0 below 500 K indicating the low volatility of these components. The calculated latent heat of biodiesel components in the range of 300~750 K are shown in Figure 4.16. It can be seen from both figures that vapor pressure and latent heat curves are close among the biodiesel components.

Table 4.3 Critical temperatures and volume of biodiesel components

Component	Palmitic ($C_{16}H_{32}O_2$)	Stearic ($C_{18}H_{36}O_2$)	Oleic ($C_{18}H_{34}O_2$)	Linoleic ($C_{18}H_{32}O_2$)	Linolenic ($C_{18}H_{30}O_2$)
T_c (K)	767.1	774.2	772.3	795.3	797.2
V_c (cm^3/mol)	946.5	1056.7	1036.7	1016.7	996.7

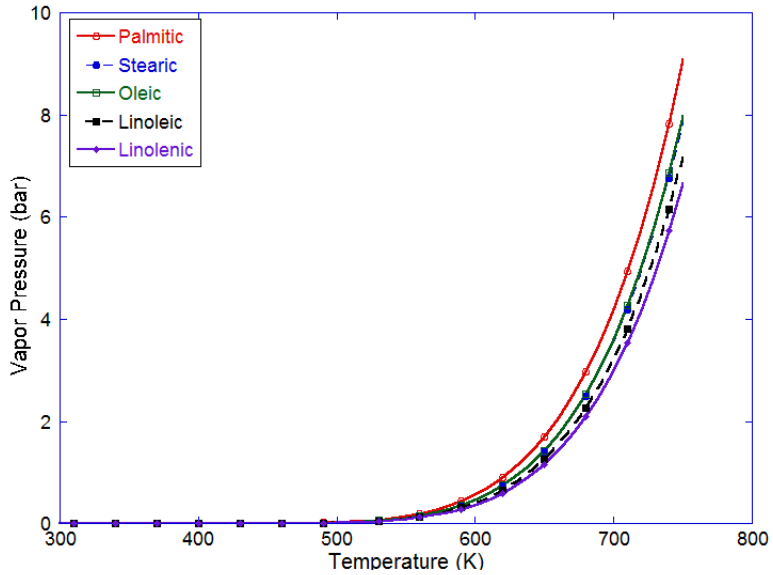

Figure 4.15 Vapor pressure of biodiesel components in the temperature range of 300~750 K

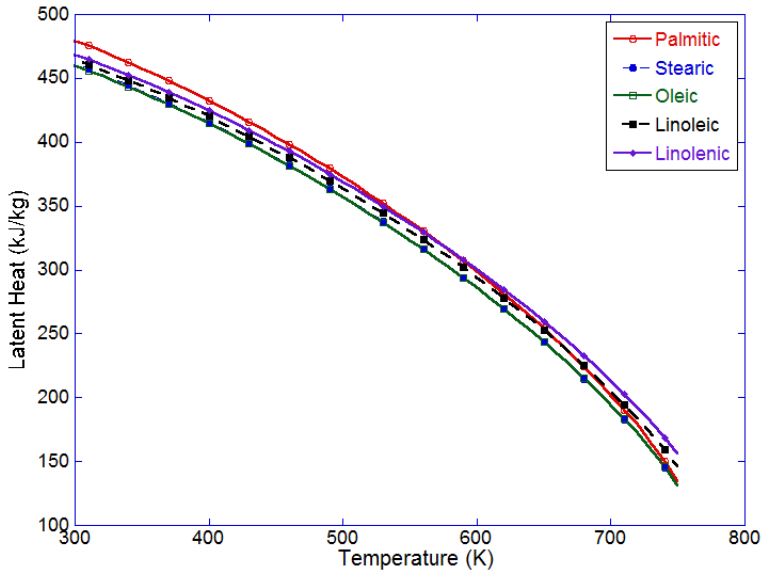

Figure 4.16 Latent heat of biodiesel components in the temperature range of 300~750 K

4.4 Biodiesel Vaporization Modeling Using a Discrete Component Approach

It is known from Sec. 3.2 that there are two different strategies in the vaporization model of biodiesel fuel which is composed of five components with close properties. The biodiesel vaporization model assumed biodiesel fuel as a single component fuel, and the physical properties of the fuel are calculated using the mean critical properties determined by its composition using mixing rules. On the other hand, the vaporization of biodiesel can also be modeled using the discrete component approach by tracking the mass/mole fractions of all of the components. In this study, using both modeling strategies, the vaporization process of biodiesel drops at different ambient conditions is simulated. The resulting histories of drop size and temperature of biodiesel drops at different ambient temperatures using both strategies are compared in Figure 4.17 and Figure 4.18, respectively. It can be seen from both figures that the results calculated using both strategies are close to each other for all of the three selected ambient conditions except the fact that the biodiesel vaporization model predicts more drop expansion at the beginning. Also, the predicted drop lifetime using both strategies is identical.

Using the discrete component approach, the histories of vaporization rate fractions and liquid phase volume fractions can be calculated. The resulting values for both variables at

T_{amb}=800 K are plotted with time in Figure 4.19 and Figure 4.20, respectively. It can be seen from both figures that both variables almost keep constant during the vaporization processes expect at the end when the drop size is very small. Using the discrete component approach, the composition of the fuel does not vary significantly. Consequently, from these figures, it can be concluded that the biodiesel vaporization model and the discrete component approach perform similarly in predicting biodiesel drop vaporization. This observation demonstrates the validity of the biodiesel vaporization model which is computationally efficient. Therefore, in this study, biodiesel vaporization model is used to model biodiesel drop vaporization in practical conditions which will be discussed in the next section.

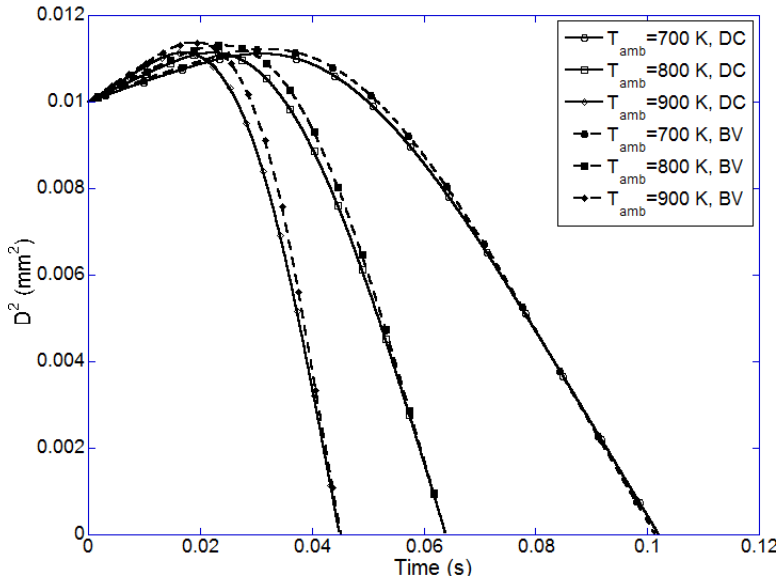

Figure 4.17 Comparison between discrete component (DC) approach and biodiesel vaporization (BV) model in predicting the drop size histories

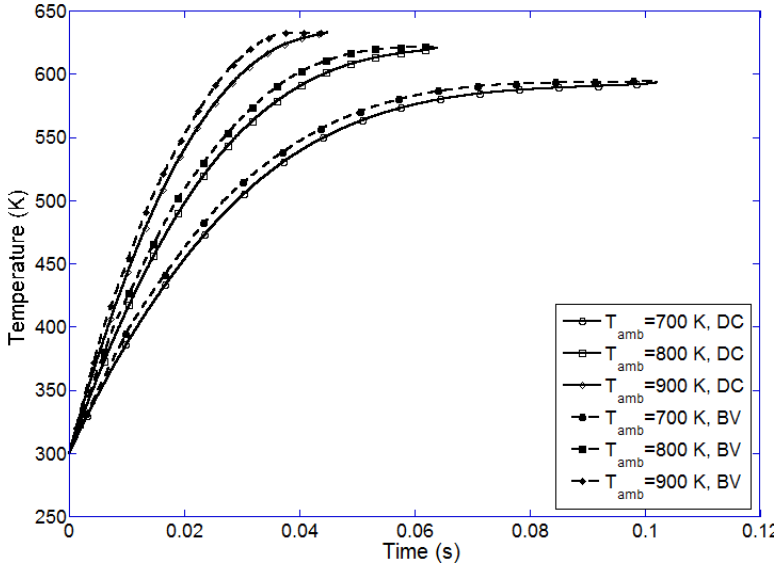

Figure 4.18 Comparison between discrete component (DC) approach and biodiesel vaporization (BV) model in predicting the drop temperature histories

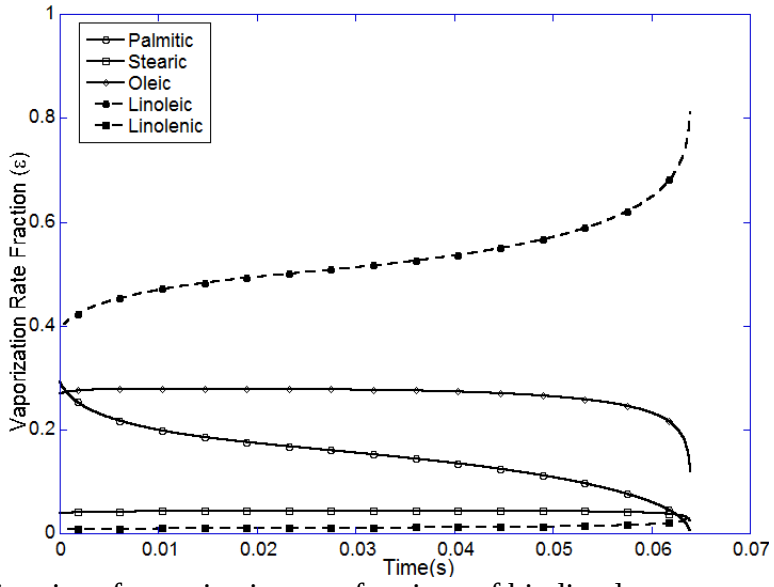

Figure 4.19 Histories of vaporization rate fractions of biodiesel components, T_{amb}=800 K

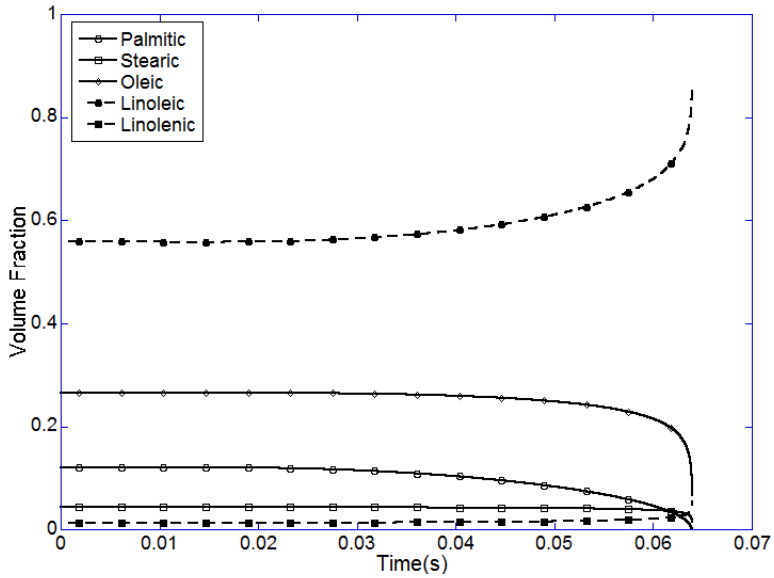

Figure 4.20 Liquid phase volume fraction histories of biodiesel components, T_{amb}=800 K

4.5 Vaporization of Biodiesel and Its Blend with Diesel Fuel

In this section, the biodiesel vaporization model was applied to simulate the experimental results of rapeseed methyl ester by Morin et al. (2000) for validation. In the experiment, biodiesel drops were generated at the tip of a quartz fiber inserted in a cylindrical chamber under various pressure and temperature conditions. In this study, the model was used to simulate six cases from the experiment with the ambient pressure equal to 1 bar and the ambient temperatures ranging from 748 to 1019 K. The selected temperatures are within the operating range of a diesel engine.

The vaporization of biodiesel drops was modeled using the biodiesel vaporization model described in Sec. 3.2. Biodiesel was assumed to consist of the five dominant components listed in Table 4.1. The physical properties of biodiesel were evaluated using the methods described in Sec. 3.2 except the critical temperature and pressure, because the critical temperature and pressure of the fuel used in experiments are provided in the original literature (i.e., T_c=692 K, P_c=15.5 bar). Comparisons of experimental and numerical drop size histories are shown in Figure 4.21 and Figure 4.22 for different ambient temperatures. It can be seen that the calculated vaporization histories agree with the experimental data very well. The good agreement indicates that the biodiesel vaporization model is able to simulate biodiesel drop vaporization reasonably well. Close examinations of the size history also

reveal that the drop dilates significantly at the beginning of the vaporization process due to ambient heating before the mass transfer process actually occurs due to the low vaporization rate. This phenomenon is more evident at low ambient temperatures conditions in which longer heating time is required.

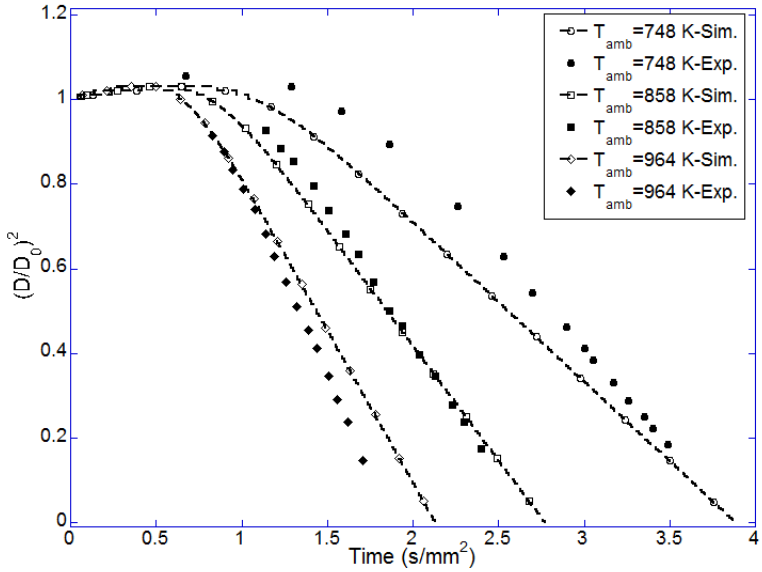

Figure 4.21 Vaporization histories of biodiesel drops under different ambient temperatures at P_{amb}=1 bar

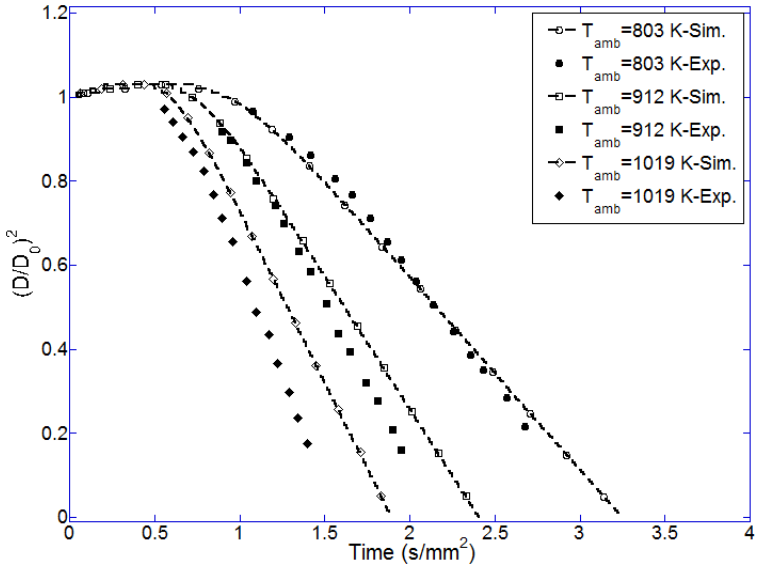

Figure 4.22 Vaporization histories of biodiesel drops under different ambient temperatures at P_{amb}=1 bar

In practice, biodiesel has been used in many applications by blending with diesel fuel. Therefore, it is interesting to study the vaporization behaviors of such a fuel blend. Since experimental data on single drop vaporization of such fuel blend are not available, only the model results of diesel-biodiesel blend will be shown in this study. For the diesel-biodiesel blends, since petroleum fuels are composed of hundreds of hydrocarbon species, drop vaporization will be modeled using the continuous thermodynamics approach described by Sec. 3.1. According to the discussion in the above sections, biodiesel derived from vegetable oil also consists of many oxygenated hydrocarbon species but mostly contains five major components. Thus, biodiesel will be modeled as the mixture of its five discrete components, and the biodiesel vaporization model will be used. Therefore, diesel-biodiesel drops will be described by a combination of continuous distribution and discrete components, and so is the gasoline-ethanol drop which will be discussed in the next section. As a result, the present vaporization model for petroleum-biofuel blends can be regarded as a hybrid model. The gamma distribution curve mentioned in the previous section for diesel fuel (α=23.0, β=8.15, γ=0) is shown in Figure 4.23, in which the range of the molecular weights of biodiesel major components is also shown. From the relative molecular weight ranges of both multicomponent fuels, it can be seen that biodiesel has a relatively higher average molecular weight than diesel fuel.

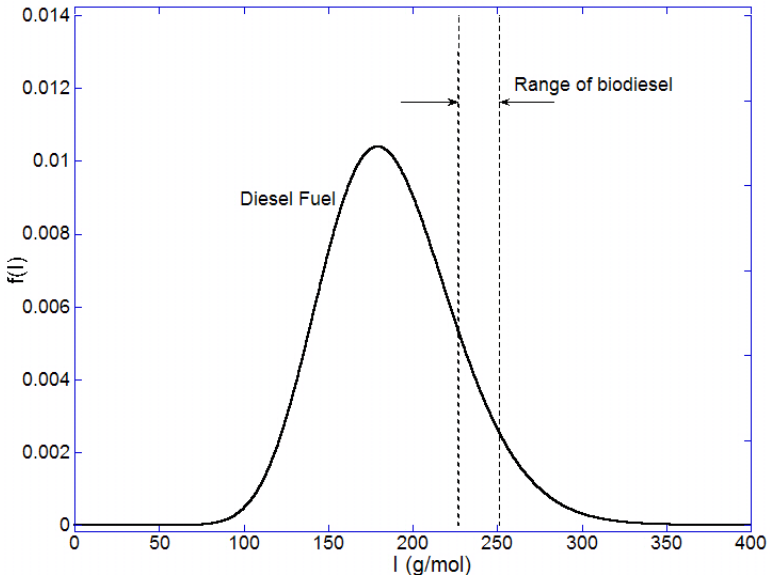

Figure 4.23 Molecular weight distribution of diesel fuel and the approximate range of the molecular weight of biodiesel

In this study, four different fuel blends were selected for modeling, including B0 (diesel fuel), B5, B20 and B100 (biodiesel). B20 means that there is 20% biodiesel in the blend on a volume basis. The biodiesel properties were evaluated based on those of soybean methyl ester (Ramadhas et al., 2005). As mentioned earlier, biodiesel properties could vary noticeably due to the variation in feedstock. The properties used in this study were calculated by data from various literatures and most commonly used values. During the course of this study, it was found that the critical temperature has a significant effect on the vaporization prediction because it determines the highest temperature a liquid drop will survive, thus influencing the lifetime prediction. It should also be noticed that the critical temperature in Table 4.3 is generally higher than that reported by Morin et al. (2000), i.e., 692 K, which was directly used in the biodiesel vaporization model validation in the previous section. Therefore, the predicted vaporization result of B100 in this section will be different from that reported in Figure 4.21 and Figure 4.22. Moreover, the modeling of B0, B5, B20, and B100 in this section is meant to verify the validity of the present model in predicting the vaporization of drops of different compositions.

Figure 4.24 shows the size histories of drops blended by diesel fuel and biodiesel at 1 bar and 912 K predicted by the hybrid vaporization model. Based on the molecular weight distribution in Figure 4.23 and the volatility of fuel components, it is expected that a majority of diesel components will have vaporized before biodiesel components start to vaporize. Results shown in Figure 4.24 are consistent with such expectations. It is shown that the drop lifetime increases as the percentage of biodiesel in the blend increases. For the B100 drop, a longer heating time is required, and thus dilation is more evident compared with other drops. The slopes of the D^2 curves are similar for all the four fuel blends, indicating similar vaporization rates once the heating process is completed and the drop has reached a certain temperature. The corresponding drop temperature histories are shown in Figure 4.25. These curves show that the average drop temperature is higher as the biodiesel volume fraction increases, indicting higher heating rate and decreased overall vaporization rate. The temperature required for B100 drop vaporization is clearly higher than others. Predicted drop lifetime data for various ambient temperatures are listed in Table 4.4. It can be seen that the

size histories and lifetimes of B5 and B20 drops are close to those of the pure diesel fuel drops and drop lifetime increases as the percentage of biodiesel increases.

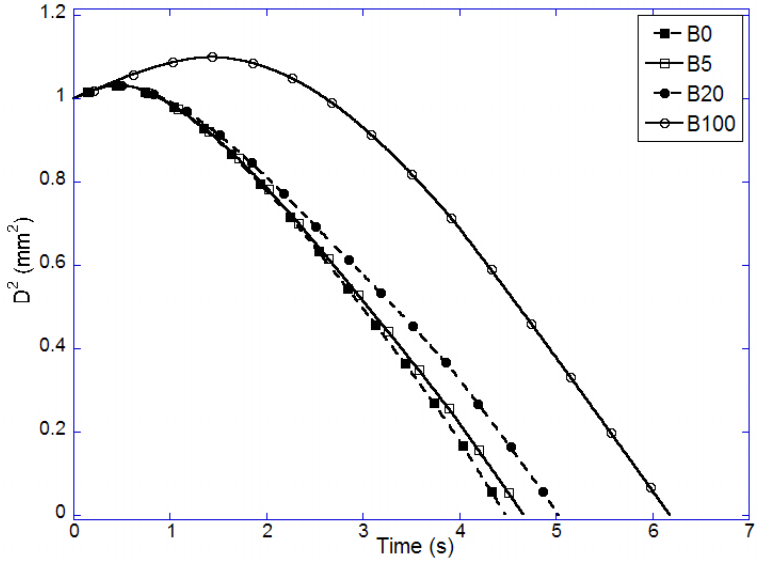

Figure 4.24 Vaporization histories of diesel-biodiesel blends at T_{amb}= 912 K, P_{amb}=1 bar

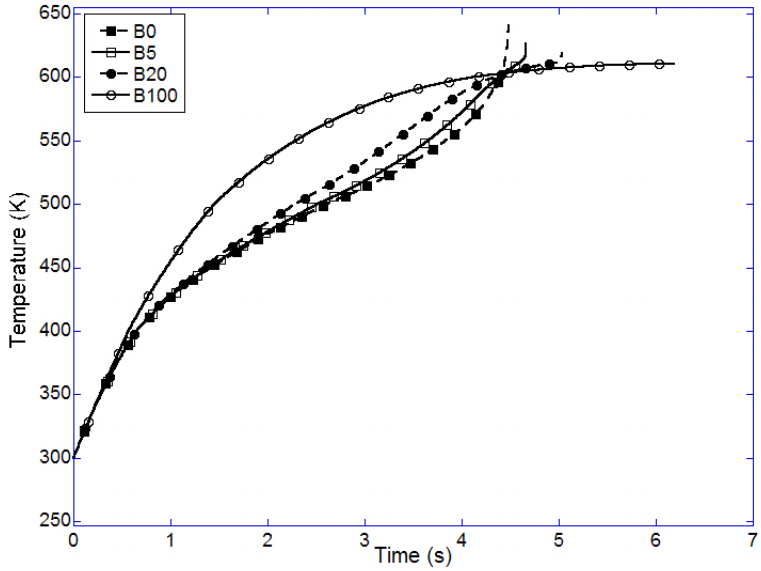

Figure 4.25 Drop temperature histories of diesel-biodiesel blends at T_{amb}= 912 K, P_{amb}=1 bar

Table 4.4 Drop lifetimes (second) for diesel-biodiesel blends at different ambient temperatures and initial compositions

T_{amb} (K)	B0	B5	B20	B100
1019	3.83	3.97	4.24	5.06
912	4.48	4.67	5.03	6.19
858	5.50	5.77	6.32	8.08

The histories of biodiesel volume fraction during the vaporization process for B5 and B20 are shown in Figure 4.26. These volume fraction history curves differ from those of n-heptane-n-decane drop shown in Figure 4.4 because the composition of diesel fuel, which is a complex multicomponent fuel itself, vary significantly during the vaporization process. For the most part of the vaporization process, the volume fraction of biodiesel increases. However, near the end of the vaporization process, the heavy diesel components still remain in the drop while a significant amount of biodiesel components have vaporized. The mean molecular weight of diesel fuel increases sharply at the end according to Figure 4.27. As a result, the volume fraction of biodiesel decreases before the entire drop completely disappears. Figure 4.28 shows the evolution of diesel fuel composition in the B20 drop during vaporization. It can be seen that the distribution curve of diesel fuel shifts to the high molecular weight region, resulting from the survival of the heavier components. In other words, lighter components vaporize earlier, and the remaining diesel fuel is heavier and less volatile.

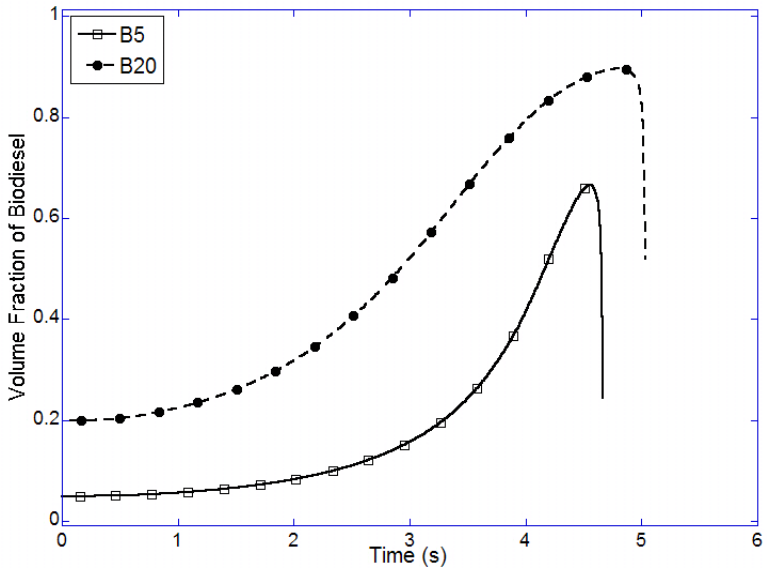

Figure 4.26 Histories of the volume fraction of biodiesel during the vaporization of diesel-biodiesel blends at T_{amb}= 912 K, P_{amb}=1 bar

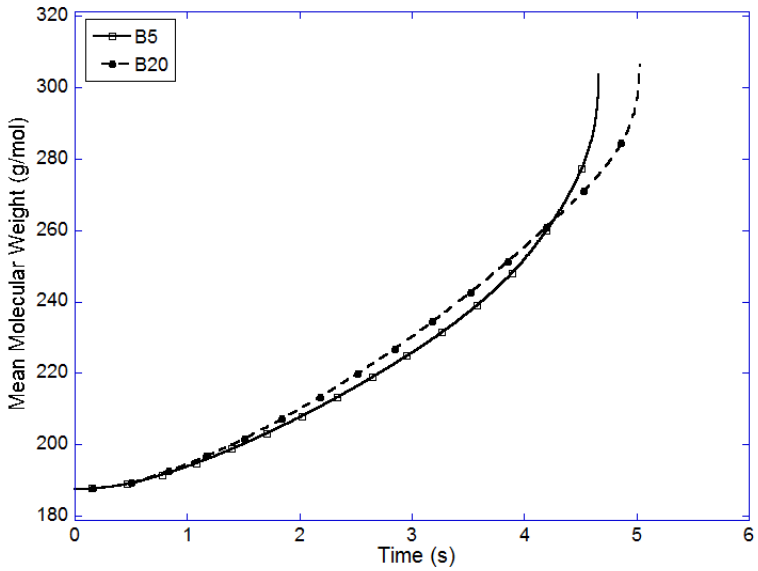

Figure 4.27 Histories of the mean molecular weight of diesel fuel during the vaporization of diesel-biodiesel blends at T_{amb}= 912 K, P_{amb}=1 bar

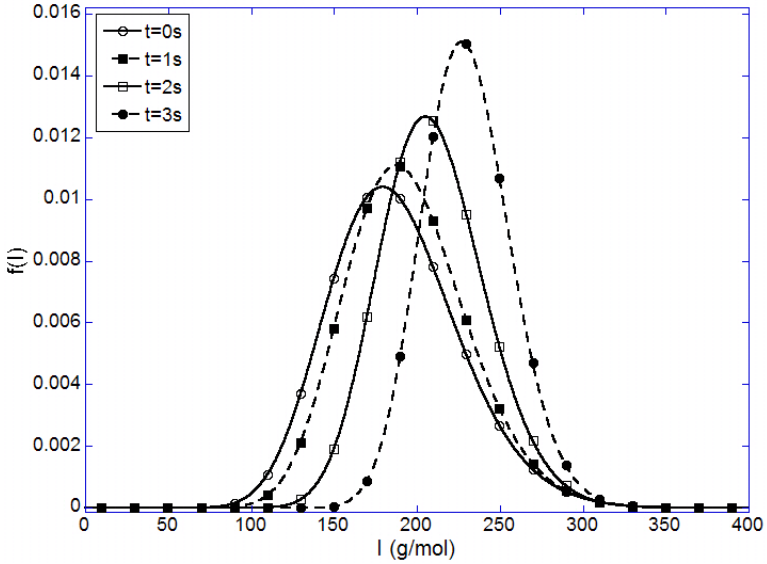

Figure 4.28 Distribution of diesel fuel composition at different times for B20 drop at T_{amb}= 912 K, P_{amb}=1 bar

The sequence of vaporization of both fuels in the blend can also be illustrated by the histories of accumulated vaporization mass shown in Figure 4.29 for B20. It can be seen that biodiesel component in the drop start to vaporize after about 2 seconds when a large amount of diesel fuel has become vapor. In internal combustion engines, the vaporization histories of different fuel components determine the vapor distribution before combustion. Less volatile fuel components will be dominant as the drop penetrates through the combustion chamber and may lead to emissions issues for the engine. It should be noted that the vaporization model need to be used together with a combustion model that can consider the different chemical kinetics of diesel fuel and biodiesel for engine spray combustion simulation. Nonetheless, the present vaporization model will be able to predict a more detailed fuel component distribution and improve the accuracy of the overall combustion simulation using practical fuel blends.

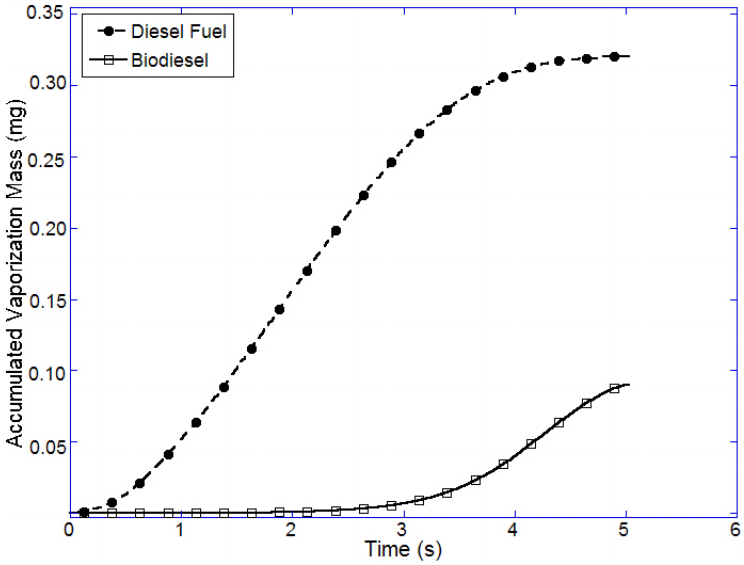

Figure 4.29 Histories of accumulated vaporization mass of diesel fuel and biodiesel for B20 drop at T_{amb}= 912K, P_{amb}=1 bar

To further study the effect of the compositions of different diesel-biodiesel blends on vapor distribution, the hybrid vaporization model was applied to diesel-biodiesel sprays with different initial compositions, i.e., B0, B20, and B100. Only non-combusting conditions are simulated here since the emphasis of this study is on vaporization modeling. The injected fuel mass for each fuel spray is 8 mg with an injection duration of 3 ms. Simulations were performed at the same ambient conditions as in the experiments by Pickett and Siebers (2004). The computational domain has a height of 10 cm and a diameter of 12.5 cm and is discretized with a two-dimensional mesh which has 32 cells in the radial direction and 50 cells in the axial direction. The histories of the total injected fuel and total vapor mass for each spray in the domain are shown in Figure 4.30. It can be seen that the vaporized fuel mass decreases if there is more biodiesel in the initial fuel blend. This trend can be visualized by comparing the mass fraction distributions of both diesel fuel and biodiesel vapors for different sprays. Figure 4.31 shows the vapor mass fraction distributions at 1.4 ms after the start of injection. It can be seen that the liquid penetration is shorter if there is more biodiesel initially. For the B20 spray, diesel fuel vapor exists in a large region similar to that of diesel fuel spray, while there is a small amount of biodiesel concentrating in a small region near the tip of the spray. Due to the low volatility, biodiesel spray produces much smaller amount of

vapor in comparison with diesel fuel spray, and the vapor concentrates in a smaller region distant from the injector.

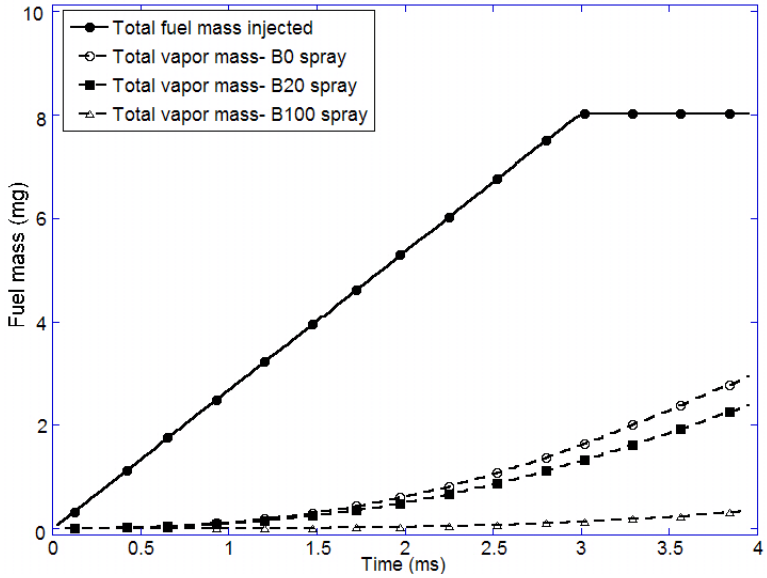

Figure 4.30 Histories of total fuel mass injected and vapor mass in the domain for B0, B20, and B100 sprays, T_{amb}=900 K, P_{amb}=37.58 bar

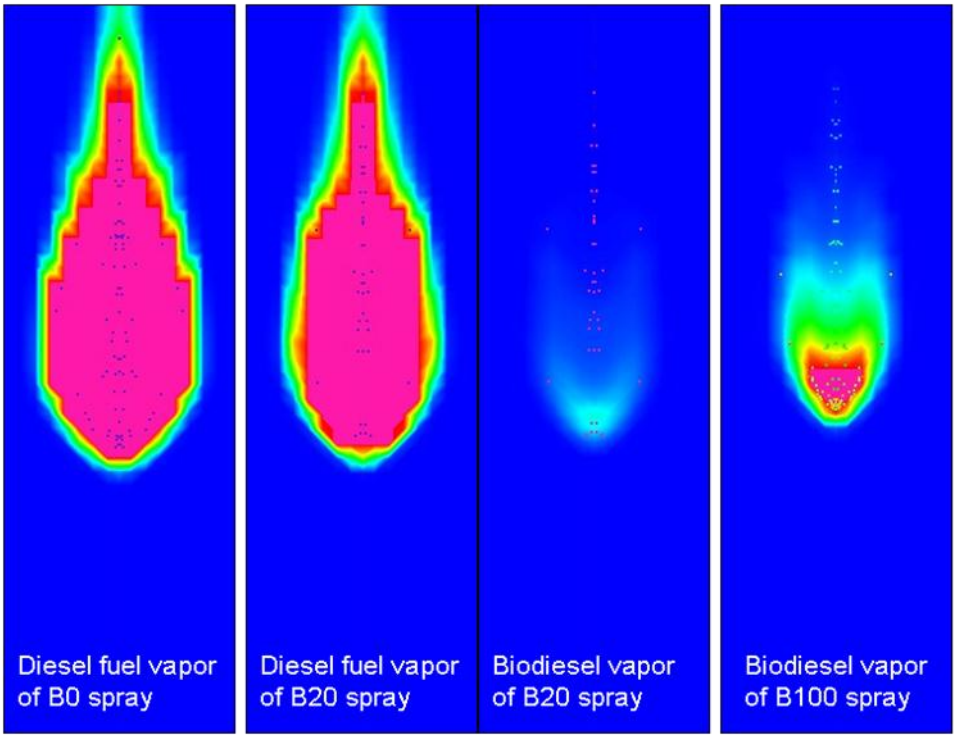

Figure 4.31 Vapor distributions of diesel fuel and biodiesel for B0, B20, and B100 sprays at t=1.4 ms, T_{amb}=900 K, P_{amb}=37.58 bar

4.6 Vaporization of Ethanol-Gasoline Blend

Ethanol is frequently used with gasoline in spark-ignition engines. The present vaporization model was also applied to simulate the vaporization of gasoline-ethanol drops with various initial blend ratios. While E10 and E85 are common in current applications, there is also an increasing interest in using E20 to displace more gasoline without the need to modify the existing engine fuel system. E20 means that there is 20% ethanol in the fuel blend on volume basis. In this study, fuel drops of E0, E10, E20, E85, and E100 are modeled. Ethanol in the drop was treated as a pure single-component fuel with well-defined physical properties, while gasoline composition was represented using gamma distribution (α=5.7, β=15, γ=0 in Eq. (3.1)). The hybrid modeling strategy of the fuel blend is shown in Figure 4.32.

The ambient pressure of the computational cases is 1 atm, and the ambient temperature is 450 K, which is relevant to the in-cylinder temperature of a direct-injection spark-ignition engine during fuel vaporization. Predicted drop size histories for different initial compositions are shown in Figure 4.33. It can be seen that the drop size curves reflect the effect of composition on the drop lifetime, i.e., the presence of ethanol increases the drop lifetime. Despite that ethanol has a lower molecular weight than gasoline, the latent heat for ethanol (1025 kJ/kg at 300 K) is significantly higher that gasoline (316.6 kJ/kg at 300 K) making the drop harder to vaporize as the volume fraction of ethanol increases. The vaporization histories of E10 and E20 are close to that of pure gasoline drop with slightly increased drop lifetime, and the lifetime of E85 drop is similar to that of pure ethanol drop.

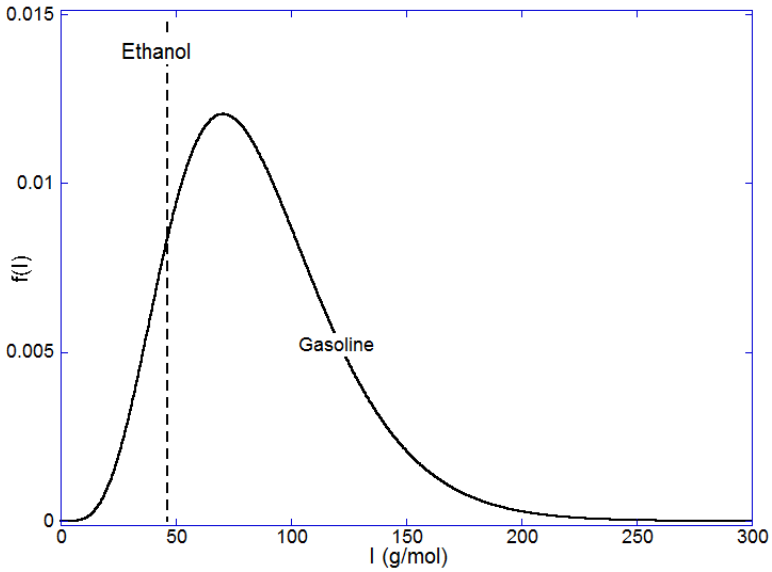

Figure 4.32 Molecular weight distribution of gasoline and the molecular weight of ethanol

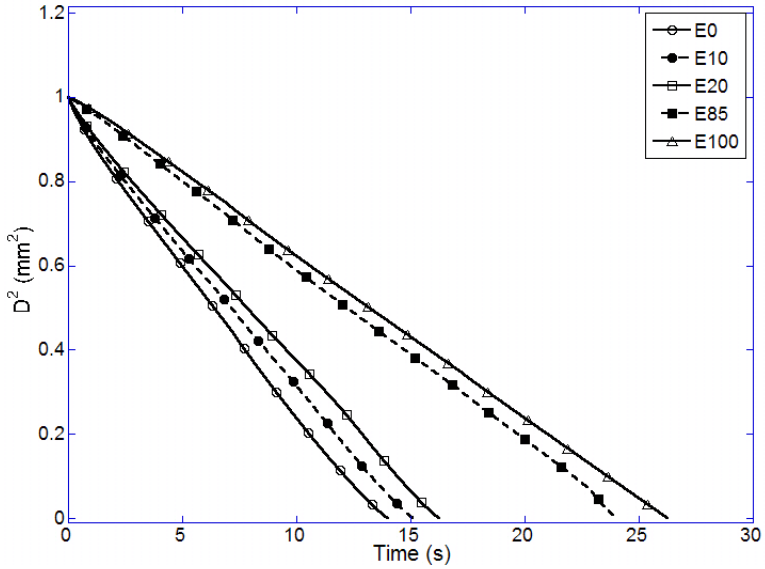

Figure 4.33 Vaporization histories of gasoline-ethanol blends at T_{amb}= 450 K, P_{amb}=1 atm

The volume fraction histories of ethanol in E10, E20, and E85 drops are shown in Figure 4.34. It can be seen that the volume fraction of ethanol increases at the early stage of the vaporization process. This phenomenon indicates that certain gasoline components are more volatile than ethanol and make the fuel vaporize faster than ethanol at the beginning. As the vaporization process progresses, the vaporization rate of ethanol increases, and the volume fraction of ethanol in the drop decreases rapidly. For example, as shown in Figure 4.34,

ethanol in the E20 drop has completely vaporized at 12 seconds, well before the remaining gasoline components completely vaporize at about 16 seconds. In other words, the E20 drop is reduced to a pure gasoline drop at the later stage of the vaporization process (i.e., from 12 to 16 seconds). Similar to the diesel-biodiesel mixture, the continuous thermodynamics model makes the mean molecular weight of gasoline increase and the fuel gradually becomes less volatile than ethanol. The remaining heavier components of gasoline dominate the vaporization at the final stage.

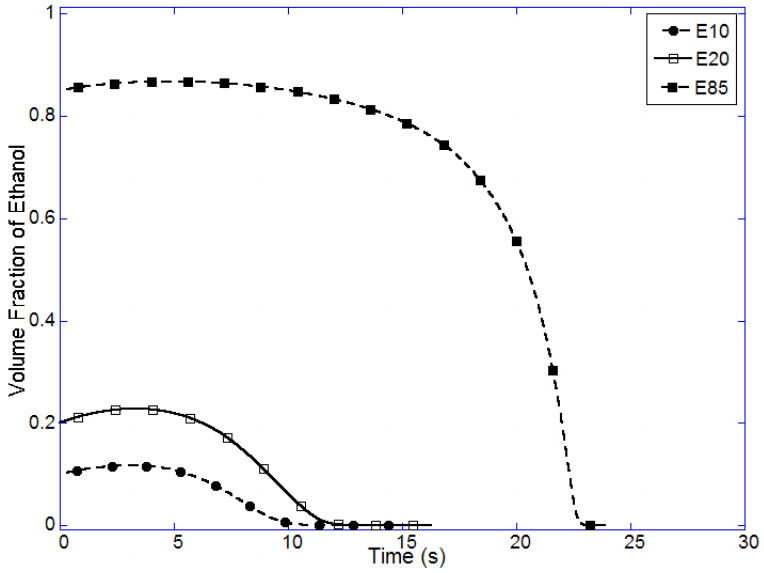

Figure 4.34 Histories of the volume fraction of ethanol during the vaporization of gasoline-ethanol blends at T_{amb}= 450 K, P_{amb}=1 atm

The histories of the accumulated vaporization mass for both ethanol and gasoline in E10 and E85 are shown in Figure 4.35. It can be seen that both fuels start to vaporize as soon as the drop is generated, unlike the cases of diesel-biodiesel blends in which biodiesel does not vaporize until a long period of time during the vaporization process (Figure 4.29). The curves for accumulated vaporization mass are close to each other showing similar mass vaporization rates of both fuels. Therefore, it is believed that the vapors of both fuels will concentrate in similar regions in spray applications.

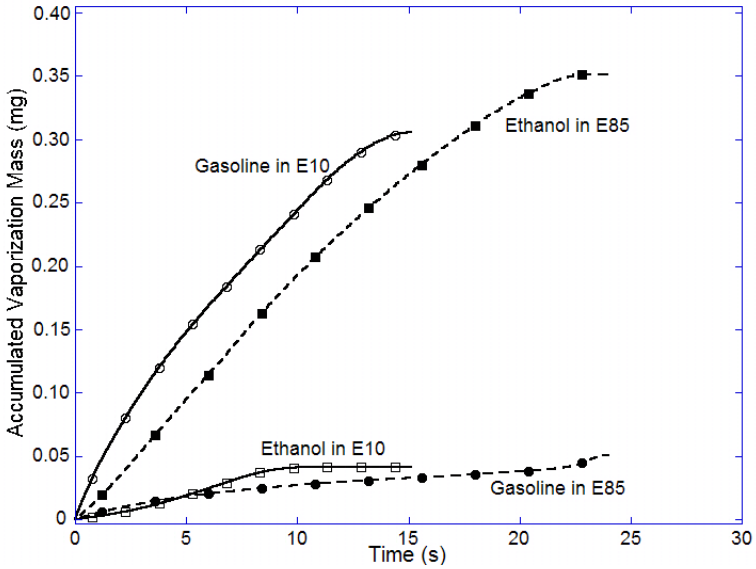

Figure 4.35 Histories of accumulated vaporization mass of gasoline and ethanol for E10 and E85 drops at T_{amb}= 450 K, P_{amb}=1 atm

CHAPTER 5 VAPORIZATION MODELING UNDER HIGH-PRESSURE CONDITIONS

In previous chapters, Raoult's law was used to as the phase equilibrium, which relates the mole fractions of a component in both the liquid and vapor phases, for drop vaporization simulation under low pressure conditions. However, in practical conditions, e.g., engine in-cylinder conditions, liquid drops vaporize in high-pressure environments. It can be shown that Raoult's law is the low pressure approximation of the general phase equilibrium that is valid for all conditions. Thus, under high-pressure conditions, using Raoult's law can lead to inaccuracy in drop vaporization modeling, and the general phase equilibrium needs to be implemented to relate the compositions of both phases at the interface. To improve the accuracy of multidimensional engine simulation, it is necessary to develop a high-pressure vaporization modeling approach to consider the effect of high ambient pressure on drop vaporization. In this chapter, the multicomponent vaporization models are coupled with general phase equilibrium to extend the model applicability to high-pressure conditions.

5.1 High-Pressure Phase Equilibrium

Using the equations derived in Sec. 3.3, the phase equilibrium of an n-heptane-nitrogen binary system can be calculated. Figure 5.1 plots the calculated mole fractions of n-heptane at phase interface with ambient pressure at different temperatures. The upper-right part of each curve with solid symbols is for the liquid phase, and the lower-left part with open symbols is for the vapor phase. For each temperature, both parts of the curves originate from the saturated pressure, where the mole fraction of n-heptane is equal to unity in both phases. As pressure increases, the liquid and the vapor sections of the curve start to deviate and finally meet at the critical mixing point. At the critical mixing point, the temperature, pressure, and composition of both phases are identical, and there is no phase difference in the system. Phase equilibrium no longer holds at or beyond the critical mixing point. It can be seen from Figure 5.1 that under higher pressure conditions, the amount of ambient gas that dissolves into the liquid phase cannot be ignored. Consequently, in contrast to the assumption of no ambient gas species dissolving in the liquid phase at low pressure conditions, the phase

equilibrium of high-pressure conditions requires that all of the species are present in both phases. Therefore, the composition of the liquid phase is changed.

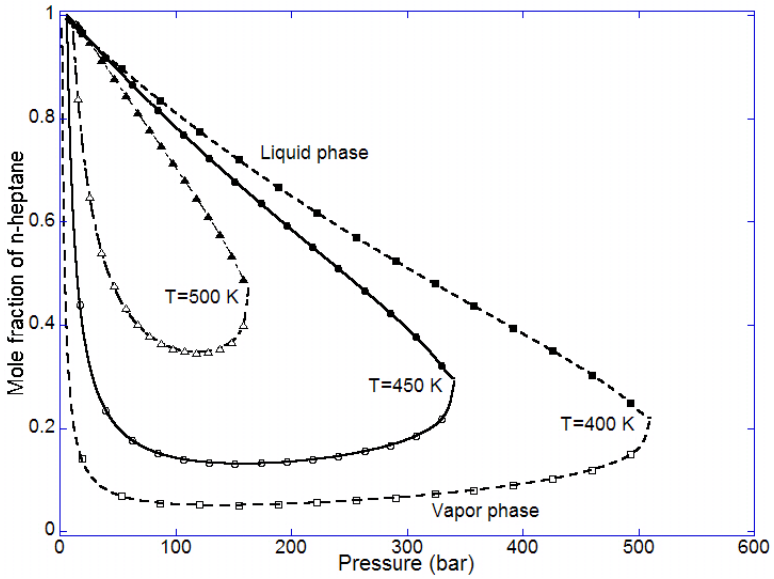

Figure 5.1 Phase equilibrium for n-heptane-nitrogen system at various temperatures and pressures

The phase equilibrium can also be expressed in a different way that the mole fractions are plotted with temperature at different pressures. In this study, to show the difference of phase equilibrium between supercritical and subcritical conditions, three different cases were calculated for P_r=0.5, 1, and 2 as shown in Figure 5.2, Figure 5.3, and Figure 5.4, respectively ($P_{c,\text{n-heptane}}$=27.4 bar). It can be seen that under subcritical (P_r<1) conditions, the mole fractions of n-heptane in both phased increased monotonously to unity with increasing temperature. However, under supercritical (P_r>1) conditions, the mole fraction of n-heptane in the liquid phase decreases slowly with increasing temperature and meets the increasing vapor phase mole fraction at a value lower than unity.

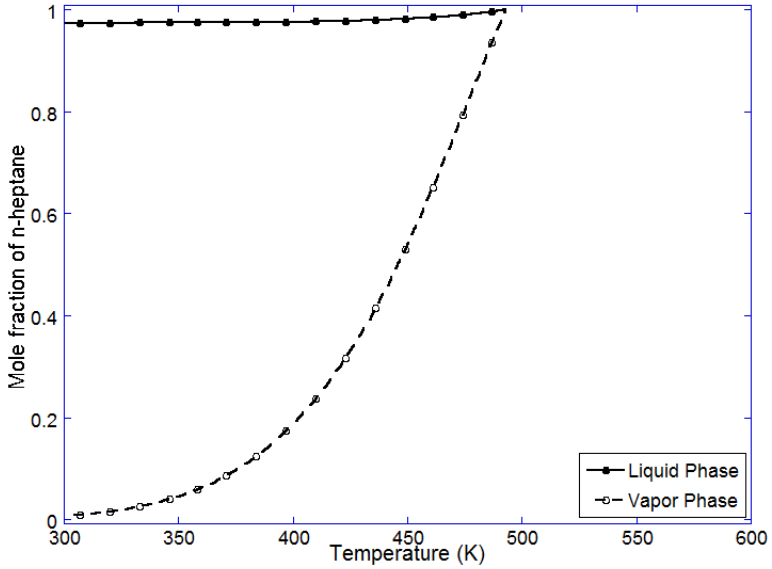

Figure 5.2 Phase equilibrium for the n-heptane-nitrogen system at various temperatures and P_{amb}=13.7 bar

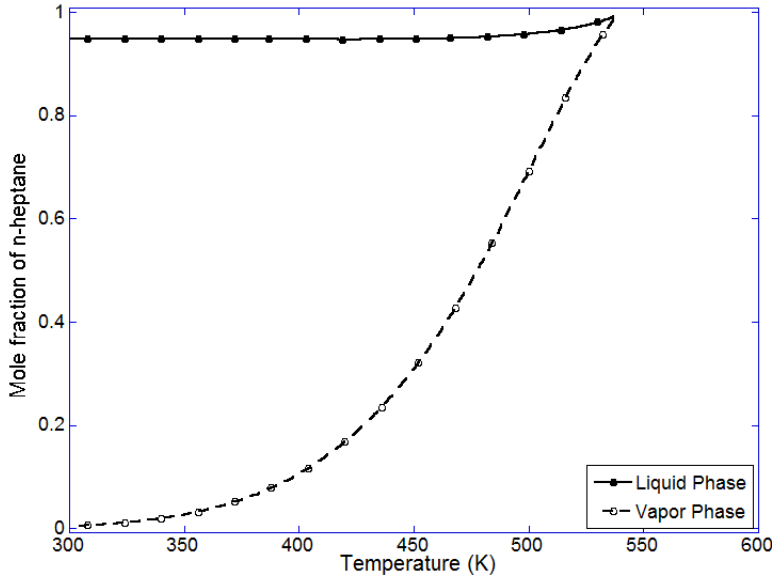

Figure 5.3 Phase equilibrium for the n-heptane-nitrogen system at various temperatures and P_{amb}=27.4 bar

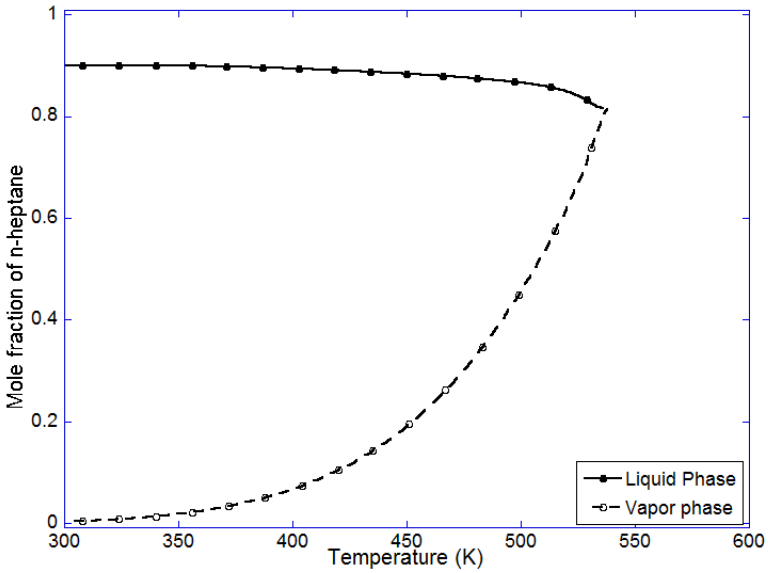

Figure 5.4 Phase equilibrium for the n-heptane-nitrogen system at various temperatures and P_{amb}=54.8 bar

Due to the fact that the binary diffusivity between the ambient gas species and the liquid component is very small in the liquid phase, the characteristic diffusion time ($t^*=R^2/D_{12}$) will be relatively large compared to the drop lifetime. Therefore, for simplicity, this study assumes that the ambient gas species will be restricted at the drop surface during vaporization, and the diffusive flux of the ambient gas species toward drop center is infinitesimal. On the other hand, in the vapor phase, since the characteristic diffusion time is much smaller than that of the liquid phase, it is reasonable to obtain a pseudo-steady solution of the species conservation equation. By applying the assumption that the diffusive flux of the ambient gas species into the liquid phase is zero, the solution of the pseudo-steady species conservation equation in the vapor phase determining the drop vaporization rate will be a same formula as Eq. (3.45) which relates the species vaporization rate with the mass fractions of the fuel vapor at the drop surface and infinity.

5.2 Model Validation

The high-pressure vaporization model described in Sec. 3.3 was first applied to the vaporization of n-heptane drops in a pure nitrogen environment at various ambient pressures and temperatures. Model predicted the drop vaporization histories were compared with experimental data by Nomura et al. (1996) for validation. The comparisons between

numerical results and experimental data are shown in Figure 5.5 to Figure 5.8. It can be seen that the numerical results in various ambient conditions agree well with the experimental data in both the shape of the drop size history and the total drop lifetime. The traditional low-pressure model based on the Raoult's law was also applied to the same conditions and compared with the high-pressure model results and experimental data in these figures. It can be seen that the simulation result using the Raoult's law at the low pressure (P_{amb}=0.5 MPa) shows acceptable agreement with the experiment data. However, as the ambient pressure increases, the error of using the Raoult's law increases. The application of the Raoult's law leads to much longer drop lifetime and will subsequently predict inaccurate distribution of fuel vapor in actual combustion devices under high-pressure conditions. Consequently, the application of high-pressure drop vaporization model in multidimensional engine simulation will be an important advancement in improving the modeling accuracy.

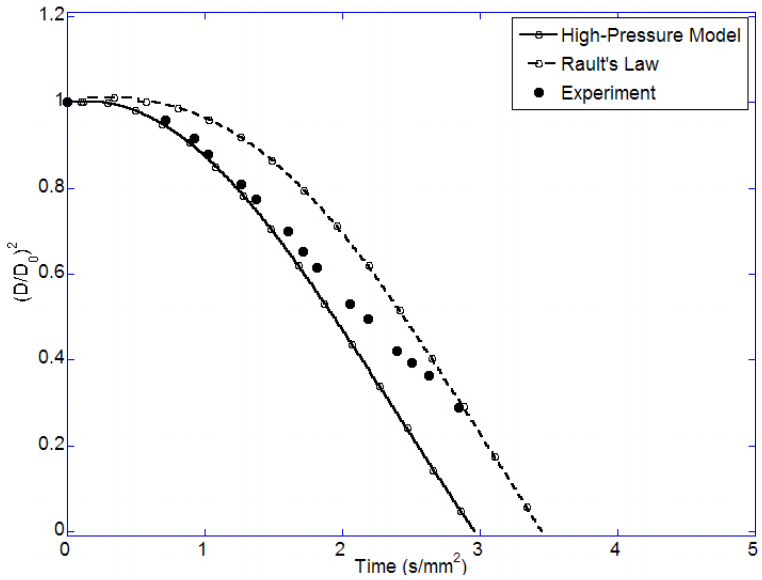

Figure 5.5 Vaporization history of a single n-heptane drop at P_{amb}=0.5 MPa, T_{amb}=655 K

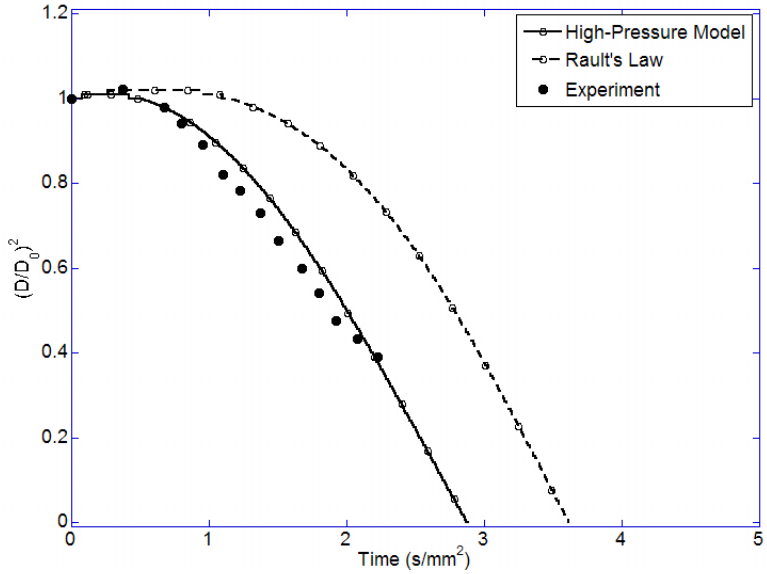

Figure 5.6 Vaporization history of a single n-heptane drop at P_{amb}=1.0 MPa, T_{amb}=669 K

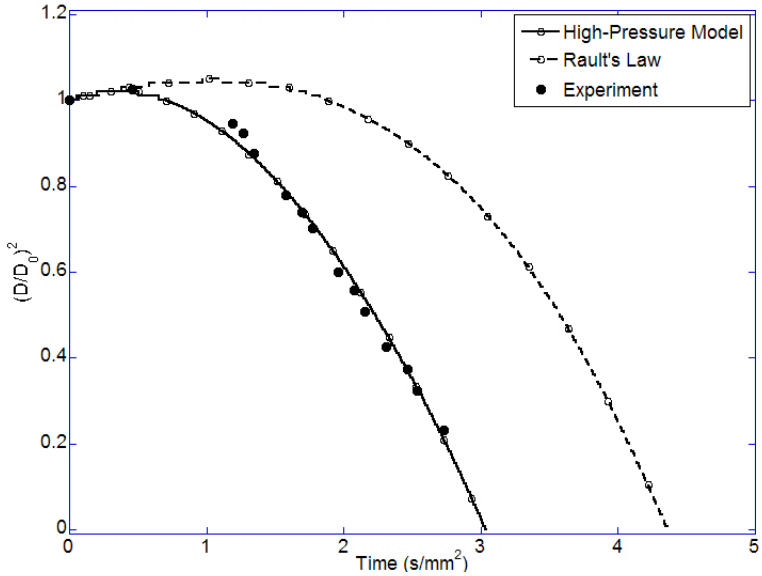

Figure 5.7 Vaporization history of a single n-heptane drop at P_{amb}=2.0 MPa, T_{amb}=656 K

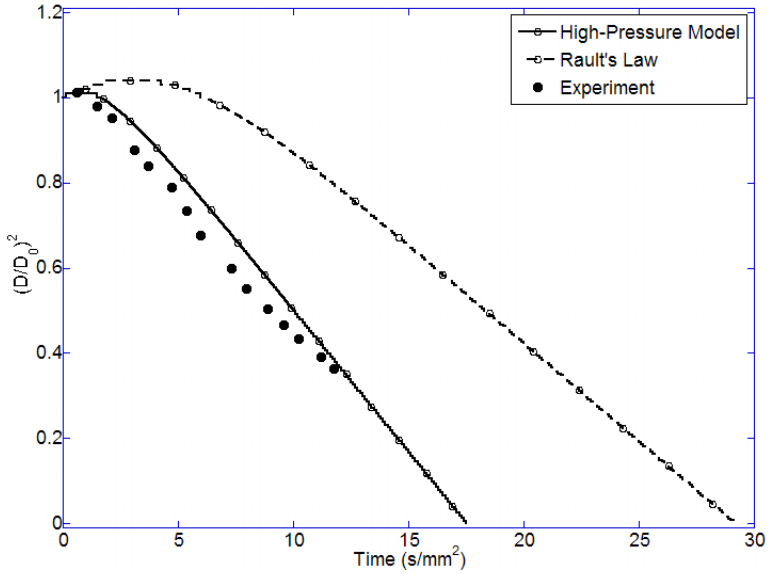

Figure 5.8 Vaporization history of a single n-heptane drop at P_{amb}=5.0 MPa, T_{amb}=453 K

5.3 Vaporization of Diesel Fuel and Biodiesel at High-Pressure Conditions

The vaporization modeling of diesel fuel drops under engine operating conditions is of primary interest since the fuel still prevails in fuelling compression-ignition engines. In this chapter, the composition of diesel fuel is also modeled using a gamma distribution based on continuous thermodynamics as shown in Sec. 3.1 except the phase equilibrium. For diesel fuel, the distribution parameters are α=23, β=8.15, and γ=0. The continuous thermodynamics model is coupled with the high-pressure phase equilibrium according to the discussion in Sec. 3.3. The correlations used to obtain fugacity coefficient as a function of molecular weight are shown in Eqs. (3.89), (3.90), and (3.91). Additional numerical iterations are needed for the implicit solution of the composition and fugacity coefficients, because of the fact that the fugacity coefficients in the vapor phase are functions of the mean molecular weight which, in the meantime, is also determined by the fugacity coefficients as shown in Eqs. (3.93), (3.94), and (3.95).

The vaporization of diesel fuel drops at ambient temperature 900 K and various ambient pressures within the range of engine in-cylinder conditions was simulated. In these cases, stagnant diesel drops with initial diameter of 0.1 mm and initial temperature of 300 K is exposed to a pure nitrogen environment. Histories of the drop surface temperature and the

square of the reduced drop diameter at different ambient pressures are shown in Figure 5.9. It can be seen that as ambient pressure increases, the heating period, which is characterized by the increasing drop size, is prolonged. On the other hand, if the pressure is higher, the vaporization rate (i.e., slope of the curve) following the heating period will increase, leading to shorter overall drop lifetime. For instance, the drop at 20 bar starts to vaporize later than 1 bar case. However, when the drop at 20 bar starts to vaporize, the vaporization rate is much higher than the 1 bar case. This phenomenon can be explained by the fact that at a higher ambient pressure, the drop surface temperature is higher, resulting in larger mass transfer number and then a higher vaporization rate. It can also be seen in Figure 5.9 that the drop surface temperature is significantly higher for conditions with higher pressure. One reason leading to the difference in drop surface temperature is the relationship between pressure and enthalpy of vaporization. Using Eq. (3.99), the enthalpy of vaporization of diesel fuel with the initial composition (α=23, β=8.15, γ=0) was plotted with temperature under different ambient pressures as shown in Figure 5.10. It can be seen that the enthalpy of vaporization decreases steadily to zero as the temperature increases to the value at the critical mixing point of a particular pressure. At a higher ambient pressure, the enthalpy of vaporization is lower, leading to higher drop heating rate according to the energy conservation equation (Eq. (2.26)).

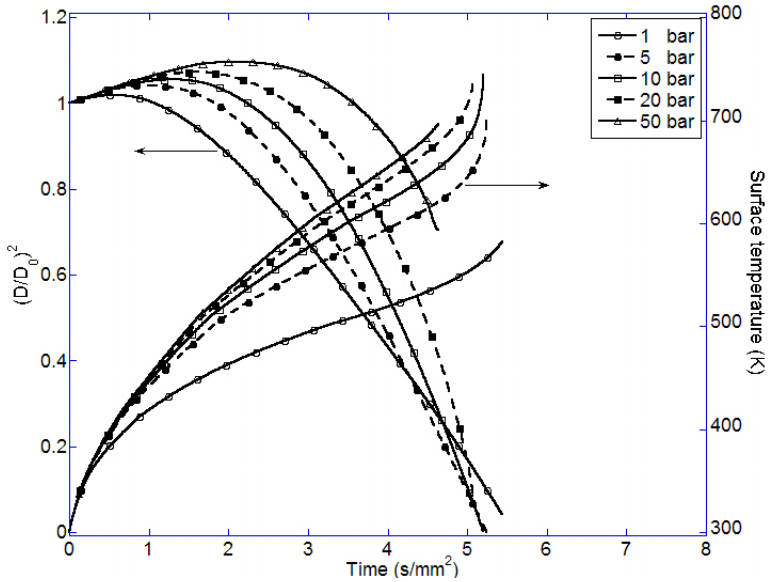

Figure 5.9 Drop size and surface temperature histories for diesel fuel at different ambient pressures, T_{amb}=900 K

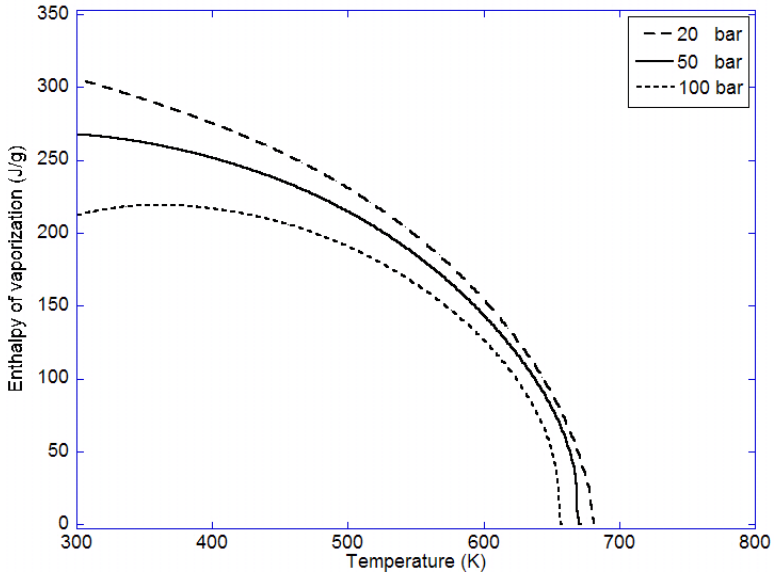

Figure 5.10 Enthalpy of vaporization as a function of temperatures for diesel fuel at various ambient pressures

On the other hand, ambient temperature also affects the way that the drop lifetime varies with ambient pressure. To investigate such effects of ambient temperature, calculations were also performed at 700 K ambient temperature, and results are shown in Figure 5.11. It can be seen that different from the results of the 900 K case, the drop lifetime at 700 K increases with increased ambient pressure. In fact, according to the phase equilibrium, high pressure directly reduces the mass transfer number and thus decreases the vaporization rate. This behavior counteracts the effect of increasing drop surface temperature that enhances the vapor mole fraction at drop surface according to Figure 5.2, Figure 5.3, and Figure 5.4. These two effects compete with each other and the net result varies. From this study, it is found that only if the ambient temperature is high enough, the drop surface temperature will increase significantly with increasing ambient pressure, leading to higher vaporization rate and shorter drop lifetime (e.g., 900 K for diesel fuel). It is anticipated that this threshold temperature will be different for different fuels.

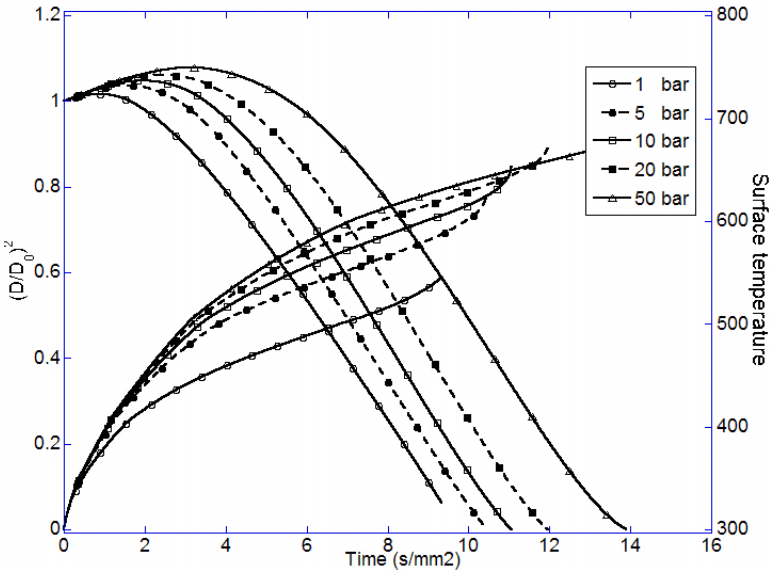

Figure 5.11 Drop size and surface temperature histories at different ambient pressures, T_{amb}=700 K

Figure 5.12 shows the evolutions of the mean molecular weights of diesel fuel in both phases at the phase interface, i.e. drop surface. It can be seen that the molecular weight of the fuel in the vapor phase is always smaller than that of the liquid phase. This phenomenon indicates that the vaporizing components are the relatively lighter components in the fuel. As a result of continuous vaporization, the mean molecular weight increases slowly at the beginning. As the lighter components continue to vaporize, the mean molecular weight increases rapidly at the end when the drop size is very small. For the cases of 20 and 50 bar, where vaporization ends at critical mixing point (see Figure 5.9), the molecular weights of the fuel in the liquid and vapor phases are equal at the critical mixing point. This is consistent with the essence of the critical mixing point that there is no difference in composition between the liquid phase and vapor phase.

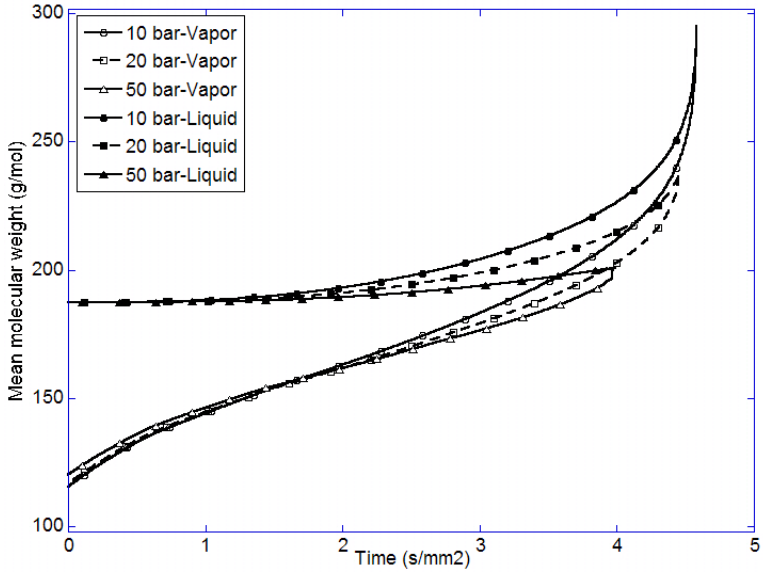

Figure 5.12 Histories of the mean molecular weight of diesel fuel in both liquid and vapor phases at the surface of the drop at various ambient pressures, T_{amb}=900 K

Biodiesel is a renewable fuel which can be produced from vegetable oils, animal fat, or other biomass feedstock. Due to its close physical and chemical characteristics to regular diesel fuel, it is a feasible alternative fuel for compression-ignition engines. The composition of biodiesel can be uncertain due to the variation in the feedstock. However, according to the discussion in Sec. 4.3, the major components of biodiesel are five methyl esters, namely, palmitic ($C_{16}H_{32}O_2$), stearic ($C_{18}H_{36}O_2$), oleic ($C_{18}H_{34}O_2$), linoleic ($C_{18}H_{32}O_2$), and linolenic ($C_{18}H_{30}O_2$). Therefore, this chapter also assumes that biodiesel is a mixture of the above five components. The composition of biodiesel, i.e., the mass fractions of these components, derived from typical feedstock can be found in Table 4.1. To perform the phase equilibrium calculation for biodiesel under high-pressure conditions, the mean values for *a* and *b* in the cubic equation of state can be obtained using the mixing rules shown in Eqs. (3.79) and (3.80) based on the composition of biodiesel and critical temperatures and pressures of its five major components.

The enthalpy of vaporization of biodiesel was also calculated according to Eq. (3.99) as shown in Figure 5.13. It can be seen that the enthalpy of vaporization of biodiesel varies in a similar way with temperature and pressure compared with that of diesel fuel shown in Figure 5.10. The overall enthalpy of vaporization of biodiesel is higher than that of diesel fuel at the

same conditions. The present model was used to simulate the vaporization of biodiesel drops under high-pressure and high-temperature conditions similar to those of diesel drop conditions. The drop size histories of biodiesel drops vaporizing at T_{amb}=900 K and various pressures are shown in Figure 5.14. It can be seen that biodiesel drops generally have longer lifetime than diesel drops in the same ambient conditions. The lifetime of the biodiesel drop varies in the same way as the diesel fuel drop when ambient pressure changes, i.e., higher pressure prolongs the heating period and reduces drop lifetime.

Moreover, in diesel engines, considering engine performance and emissions, the practical way of using biodiesel is to blend the fuel with diesel fuel at different volumetric ratios by their high miscibility. In this study, the vaporization of B20 drops, which are blended by 20% biodiesel and 80% diesel on volume basis, under different ambient pressures are simulated. The histories of drop size under different ambient pressures are shown in Figure 5.15. Results show that the vaporization histories of B20 drops are in between those of diesel fuel and biodiesel at the same ambient conditions. It is expected that the composition of B20 drop will keep changing during the vaporization process due to the difference in the vaporization behaviors of both fuels in the mixture. Figure 5.16 shows the evolution of the biodiesel volume fraction in the B20 drop. It can be seen that the volume fraction of biodiesel keeps increasing in all the cases until the end of the vaporization process, and for higher ambient pressure cases, the volume fraction of biodiesel increases at a slower rate. As shown in Figure 5.12, at the end of vaporization when the drop is very small, the mean molecular weight of diesel fuel increases sharply and becomes very large. These heavy diesel fuel components vaporize more slowly than biodiesel components. As a result, the volume fraction of biodiesel decreases at the end of the vaporization as shown in Figure 5.16.

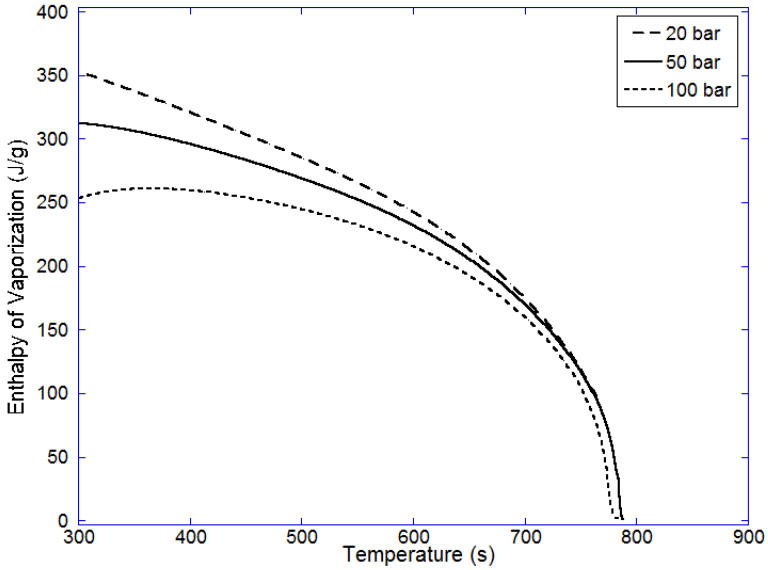

Figure 5.13 Enthalpy of vaporization as a function of temperatures for biodiesel at various ambient pressures

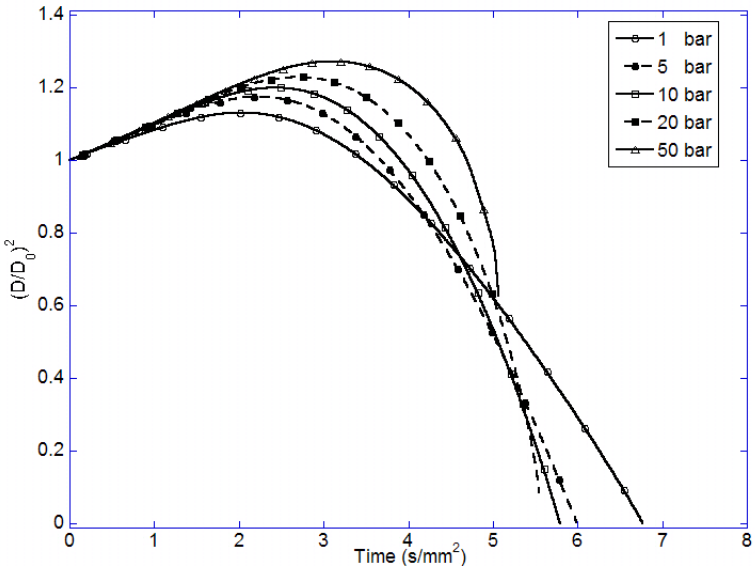

Figure 5.14 Drop size histories for biodiesel at different ambient pressures, T_{amb}=900 K

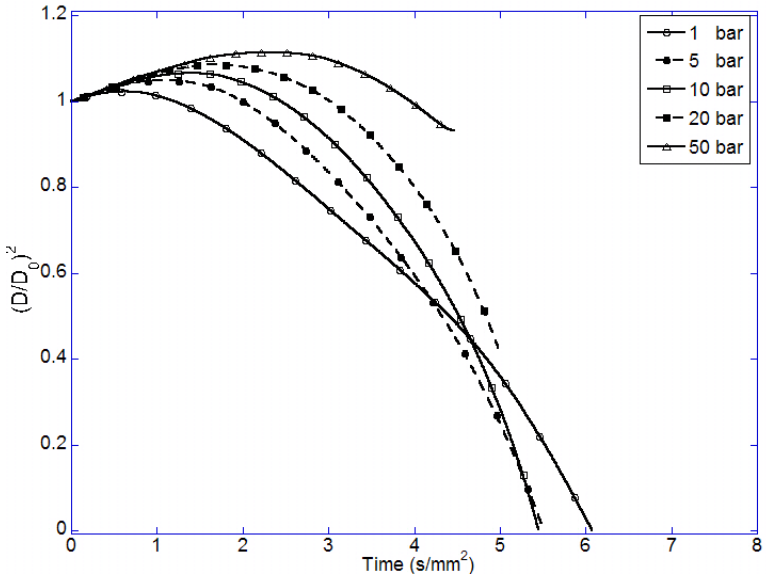

Figure 5.15 Drop size histories for B20 at different ambient pressures, T_{amb}=900 K

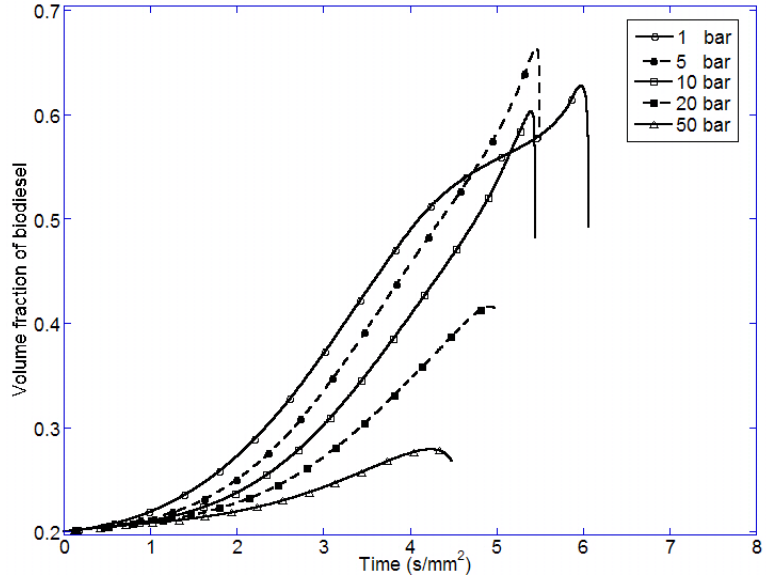

Figure 5.16 Histories of volume fraction of biodiesel for B20 at different ambient pressures, T_{amb}=900 K

To study the effect of the composition of diesel-biodiesel blend on vapor distribution under high-pressure conditions, the model was further applied to diesel-biodiesel sprays with different initial blending ratios, i.e., B0, B20, and B100, in a constant-volume combustion chamber of pure nitrogen at 38 bar and 900 K. Calculations were performed at the same ambient conditions as shown in Figure 4.30 simulating the experiments by Pickett and Siebers (2004). The CFD code is based on an updated KIVA-3V (Amsden, 1999) with

improvements in various physical models, e.g., turbulence and spray atomization (Li and Kong, 2008; Zhang and Kong, 2011). The computational domain has a height of 10 cm and a diameter of 12.5 cm and is discretized with a two-dimensional mesh which has 32 cells in the radial direction and 50 cells in the axial direction. Only non-combusting conditions are simulated here since the emphasis of this work is to study the vaporization behavior. For each spray, the injected fuel mass for each fuel spray is 8 mg with an injection duration of 3 ms. The total injected fuel mass and total vapor mass for each spray in the domain are plotted with time as shown in Figure 5.17. It can be seen that the vaporized fuel mass decreases as the initial volume fraction of biodiesel in the blend increases due to the slower vaporization rate of biodiesel components. The mass fraction distributions of both diesel fuel vapor and biodiesel vapor for different sprays at 1.4 ms after the start of injection are plotted in Figure 5.18. For the B20 spray, diesel fuel vapor exists in a large region similar to that in diesel fuel (B0) spray, while there is a small amount of biodiesel concentrating in a small region near the tip of the spray. Determined by the critical properties, biodiesel (B100) spray produces much smaller amount of vapor in comparison with diesel fuel spray, and the vapor concentrates in a small region at the spray tip distant from the injector.

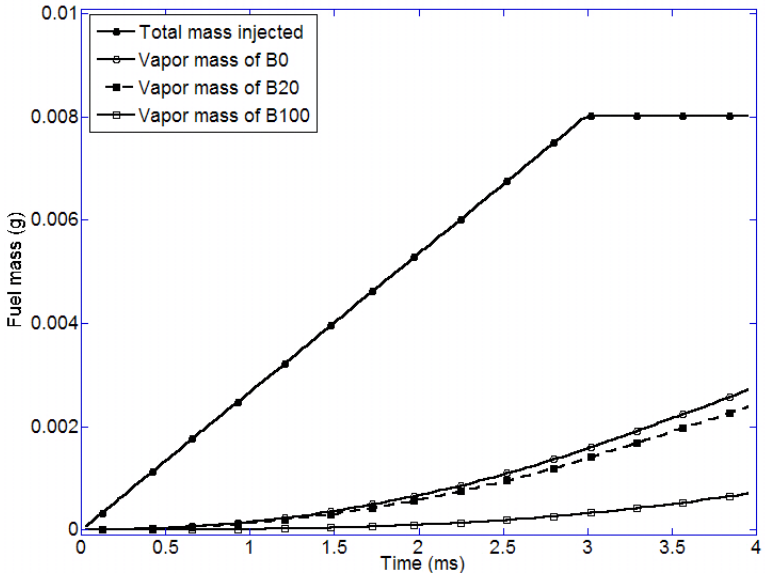

Figure 5.17 Histories of total injected fuel mass and vapor mass in the domain for sprays of B0, B20, and B100, P_{amb}=38 bar, T_{amb}=900 K

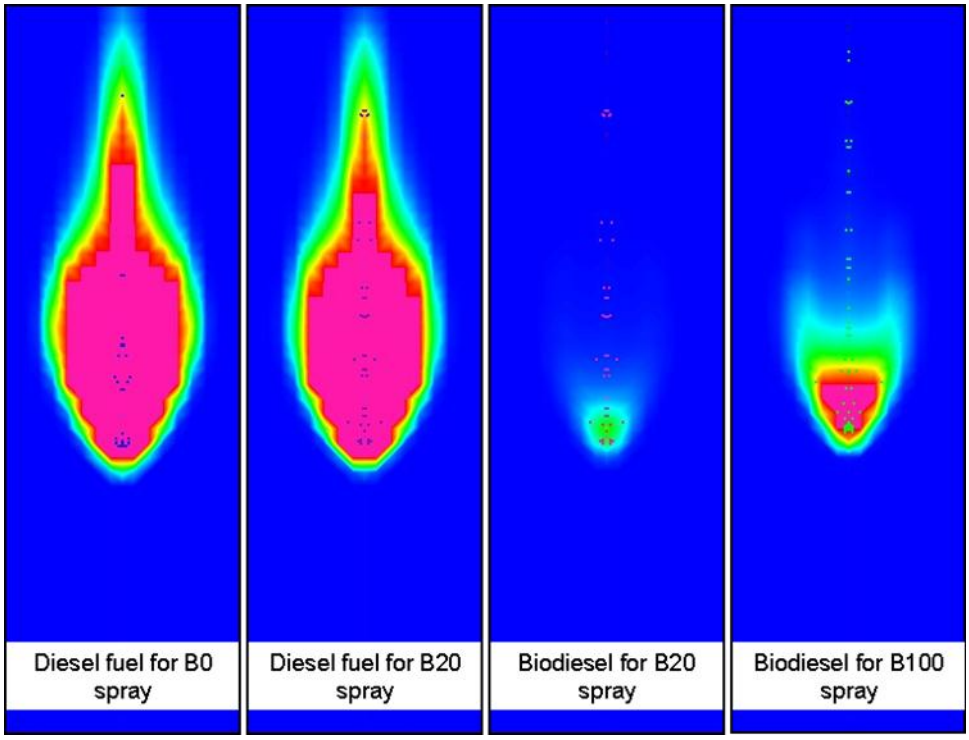

Figure 5.18 Diesel fuel and biodiesel vapor distributions for B0, B20, and B100 sprays at t=1.4 ms, T_{amb}=900 K, P=38 bar

CHAPTER 6 BIO-OIL VAPORIZATION MODELING

Bio-oil is a complex biorenewable fuel produced by fast pyrolysis of biomass. The fuel has various kinds of applications in industry. It can be either used in many combustion devices for heat and power generation, or gasified to produce synthesis gas, which in turn can be used to produce heat or transportation fuels. This chapter describes a complete vaporization modeling strategy for bio-oil based on the characteristics of its composition. After an analysis of the experimental data, a group of major components were selected to represent bio-oil produced from the pyrolysis of wood, and its vaporization was modeled using a discrete component approach. The critical and physical properties of bio-oil components were evaluated. The vaporization model was implemented into KIVA and used to investigate the vaporization behaviors of bio-oil drops and spray. The mixtures of bio-doil with other practical fuels, e.g., diesel fuel, biodiesel, and ethanol was also investigated.

6.1 Bio-oil Composition

It is known from experiments that bio-oil can contain more than 300 components (Mohan, 2006). Different from petroleum fuels which are mainly composed of hydrocarbon species, the components of bio-oil vary significantly due to feedstock and production processes. Using the GC/MS technique, Branca et al. (2003) experimentally quantified 40 components of bio-oil produced from fast pyrolysis of wood and classified the components into water, carbohydrates (including hydroxyacetaldehyde, acetic acid, hydropxypropanone, levoglucosan, and other minor species), furans, phenols, guaiacols, and syringols. The 40 components correspond to 62-65% of the total liquid. Other components are not detectable by the GC/MS technique and are nonvolatile components. It is not appropriate to use the continuous thermodynamics technique to model the vaporization of bio-oil, because it is not reasonable to simply relate the physical properties of the components with their molecular weight. Therefore, in this study, a discrete component approach was used to model the vaporization of bio-oil by selecting some representative components from each category. It should be noted that there are many unknown components in bio-oil and a proper scaling based on the known components is needed to reasonably represent the overall composition.

After an analysis of the composition of bio-oil produced from the pyrolysis of wood, a group of ten major components including water were selected to model bio-oil. The selected major components and their mass fractions based on the bio-oil products of three different companies are listed in the first column of Table 6.1. The components listed in the table are the dominant components identified from the original compositions quantified by Branca et al. (2003). The acid compounds, i.e., propionic acid and acetic acid can account for the low pH values of bio-oil. Levoglucosan is the major product of cellulose degradation, and phenol, syringol, and isoeugenol are the products of lignin pyrolysis. Consequently, it is believed that the components listed in Table 6.1 can adequately represent bio-oil produced from wood pyrolysis. Mass fractions 1, 2, and 3 are obtained from the products of Dynamotive, BTG, and Ensyn, respectively. Even though phenol and syringol have very low mass fractions in the three products in the table, they may have larger concentrations in the bio-oil produced from other resources due to the uncertainty in feedstock. Therefore, both components are included in the list of major components. Note that water is a special component in the fuel as it will strongly affect the drop breakup but not take part in fuel combustion. To best represent the original fuel composition, mass fractions of water in Table 6.1 are kept the consistent as originally reported by experiments. The mass fractions of the other nine components are scaled up in order to stand for the rest of the components, and the final compositions of bio-oil are listed in Table 6.1.

Table 6.1 Bio-oil compositions

Components	Mass fraction 1 (%)	Mass Fraction 2 (%)	Mass Fraction 3 (%)
Water	21.10	30.40	20.30
Hydroxyacetaldehyde	21.77	25.61	18.84
Acetic acid	9.48	12.25	24.18
Hydroxypropanone	15.06	10.84	8.32
Levoglucosan	17.27	11.41	15.71
Propionic acid	1.25	1.08	3.34
(5H)-furan-2-one	2.37	2.06	2.56
Isoeugenol	10.79	5.44	2.51
Phenol	0.37	0.29	1.15
Syringol	0.54	0.62	3.09

Since a discrete component approach was used to model the vaporization of bio-oil, the physical properties such as vapor pressure of bio-oil components must be estimated beforehand. To use the correlations described in Sec. 3.2, Ambrose and Joback's atom group contribution methods are used to estimate the critical temperatures and pressures of bio-oil components based on their molecular structures, and the results are listed in Table 6.2. The normal boiling points listed in this table are from available data source and are used as an important parameter in both methods. Since Ambrose's method has the definition of for the benzene group, it is best suited for isoeugenol, Phenol, and Syringol which have benzene in their molecular structures. For other components, Joback's method, which is more concise and convenient, is used.

Table 6.2 Properties of the major components of bio-oil

Components	Formula	MW(g/mol)	T_b (K)	T_c (K)	P_c (bar)
Water‡	H_2O	18.02	373	647	221
Hydroxyacetaldehyde‡	$C_2H_4O_2$	60.05	404	582	64.6
Acetic acid‡	$C_2H_4O_2$	60.05	391	588	57.3
Hydroxypropanone‡	$C_3H_6O_2$	74.08	418	595	54.8
Levoglucosan‡	$C_6H_{10}O_5$	162.14	578	733	57.0
Propionic acid‡	$C_3H_6O_2$	74.08	414	609	49.8
(5H)-furan-2-one‡	$C_4H_4O_2$	84.07	476	741	56.8
isoeugenol†	$C_{10}H_{12}O_2$	164.21	540	753	32.8
Phenol†	C_6H_6O	94.11	460	702	61.4
Syringol†	$C_8H_{10}O_3$	154.16	534	767	40.5

† Ambrose's method, ‡ Joback's method;

6.2 Predicted Bio-oil Properties

The vapor pressures of bio-oil components for temperatures in the range of 300~580 K were calculated using Pitzer's expansion (Eq. (3.48)) and plotted in Figure 6.1. It can be seen that water has the highest vapor pressure among all the components and Levoglucosan has the lowest vapor pressure. Since it is expected that components with higher vapor pressure vaporize earlier, Figure 6.1 shows a general indication about the vaporization order of the components. Figure 6.2 plots the latent heat of bio-oil components calculated using Fish and Lielmezs' method (Eq. (3.52)) with temperatures in the range of 300~580 K. It can be seen that the latent heat of water is much higher than other components, while other components

have close values of latent heat. Therefore, it is expected that the high water content will strongly affect the vaporization behavior of bio-oil. Different from the observations for biodiesel in Figure 4.15 and Figure 4.16, the physical properties of bio-oil components are not close to each other. Therefore, only a discrete component approach is acceptable, and the fuel cannot be modeled as a single-component fuel using mixing rules.

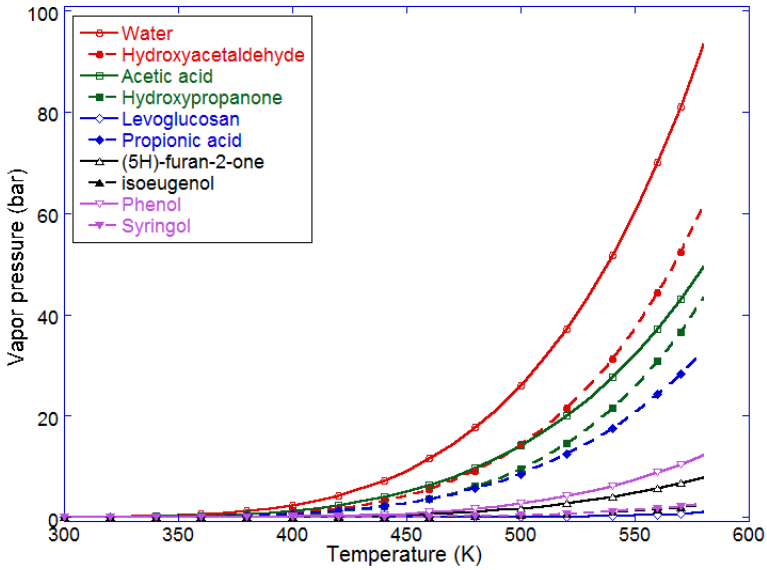

Figure 6.1 Predicted vapor pressure of bio-oil components in the temperature range of 300~580 K

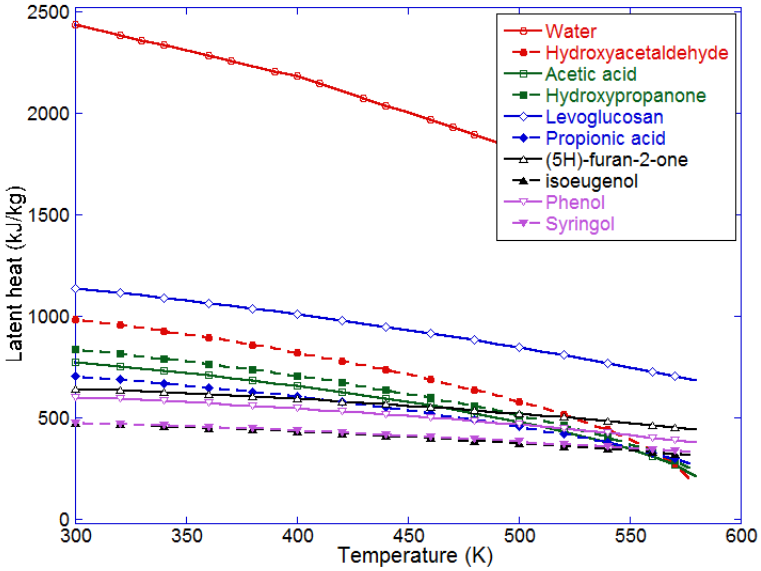

Figure 6.2 Predicted latent heat of bio-oil components in the temperature range of 300~580 K

6.3 Vaporization of Bio-oil and Its Mixtures with Other Fuels

Using the discrete component approach described in Sec. 3.2, the vaporization of a single stagnant bio-oil drop was simulated. In this study, a bio-oil drop with the modeled composition based on Mass Fraction 1 in Table 6.1 was generated and suspended in a constant-volume chamber, where the ambient temperature is 800 K and ambient pressure is 1 atm. The initial diameter of the drop is 0.1 mm. Figure 6.3 shows the predicted histories of drop size and temperature. It can be seen that the drop vaporization history does not show a straight line during vaporization. This phenomenon differs from that of single-component fuels due to the continuous change of bio-oil composition during the vaporization process. Figure 6.4 shows the histories of vaporization rate fraction (ε) which is defined in Eq. (2.18). Higher values of vaporization rate fraction indicate higher relative mass vaporization rates among all of the components. It can be seen that hydroxypropanone has the highest vaporization rate fraction as soon as the vaporization process starts and drops down to zero due to its reducing mass in the liquid phase. The vaporization rate fraction of levoglucosan remains very low for about half the vaporization process and reaches to unity at the end of the vaporization process. Other components show similar behaviors that the vaporization rate fraction increases at the beginning and finally drop down to zero later.

Figure 6.5 shows the histories of the volume fractions of bio-oil components in the liquid phase. It can be seen that the volume fractions of most of the components increase at the beginning of the vaporization process, reach to a maximum point, and decrease to zero at a later time except hydroxypropanone which has decreasing volume fraction as soon as the drop is exposed to the environment. Results also show that levoglucosan is the least volatile component, and its fraction keeps increasing and reaches to unity. In other words, at the end of the vaporization process, bio-oil becomes pure levoglucosan. The observation from Figure 6.5 agrees with that from Figure 6.4. Both figures indicate that levolucosan almost dominates the second half of the bio-oil vaporization process. Figure 6.6 shows the history of the mean molecular weight of bio-oil in the liquid phase. It can be seen that in general the mean molecular weight shows an increasing trend. This phenomenon also indicates that lighter components vaporize earlier, and heavier components are always left in the drop during vaporization.

The present vaporization model for bio-oil was applied for a bio-oil spray in the constant-volume combustion chamber same as the ones described in Sec. 4.5 and Sec. 5.3. There was 8 mg bio-oil fuel injected into the chamber in an duration of 3 ms. The ambient temperature is 900 K, and the ambient pressure is 37.58 bar in the chamber. Computational fluid dynamics computation was done by KIVA with the bio-oil vaporization model in a computational domain which has a height of 10 cm and a diameter of 12.5 cm. The mass fraction distributions of five of the bio-oil components at 1.4 ms after the start of injection are plotted as shown in Figure 6.7. The vapor distributions of other components of bio-oil are not shown because their mass fractions are relative small and are not visible in the current scale. The distribution of liquid fuel drops in the chamber at 1.4 ms is also plotted for reference.

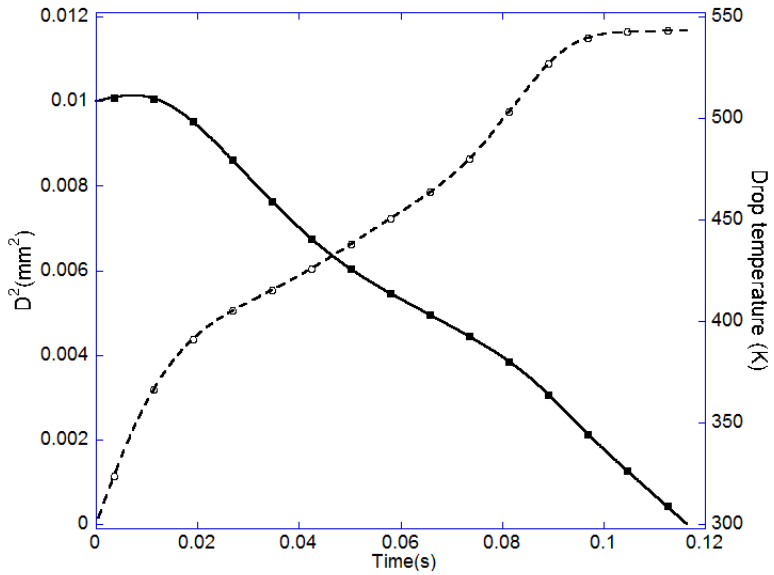

Figure 6.3 Histories of drop size and temperature of bio-oil drop at 800 K and 1 atm

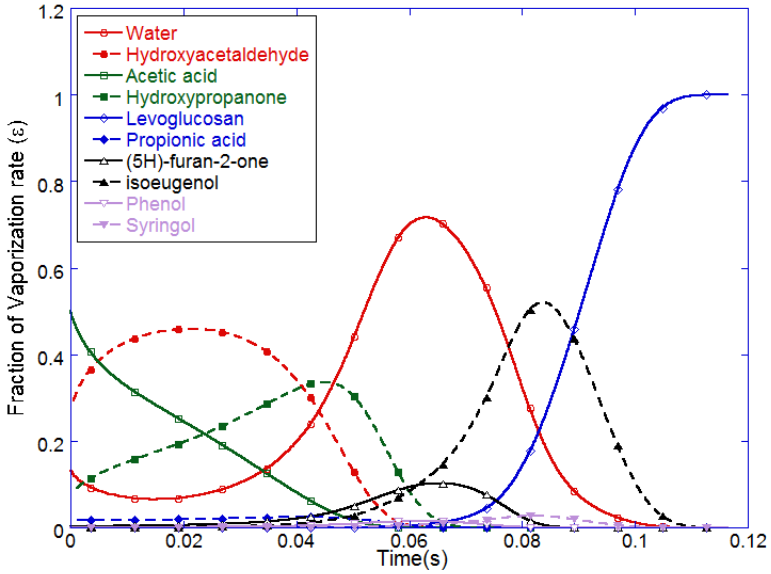

Figure 6.4 Histories of vaporization rate fraction (ε) of bio-oil components

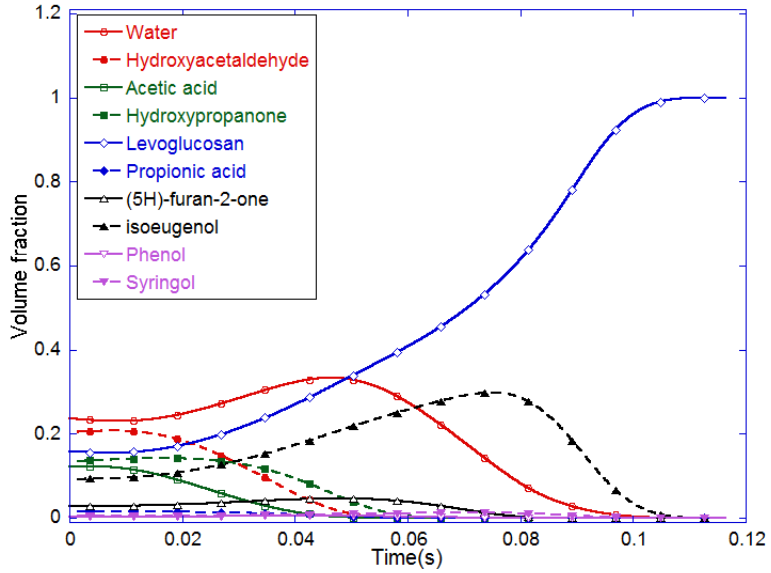

Figure 6.5 Histories of the volume fractions of all of the bio-oil components

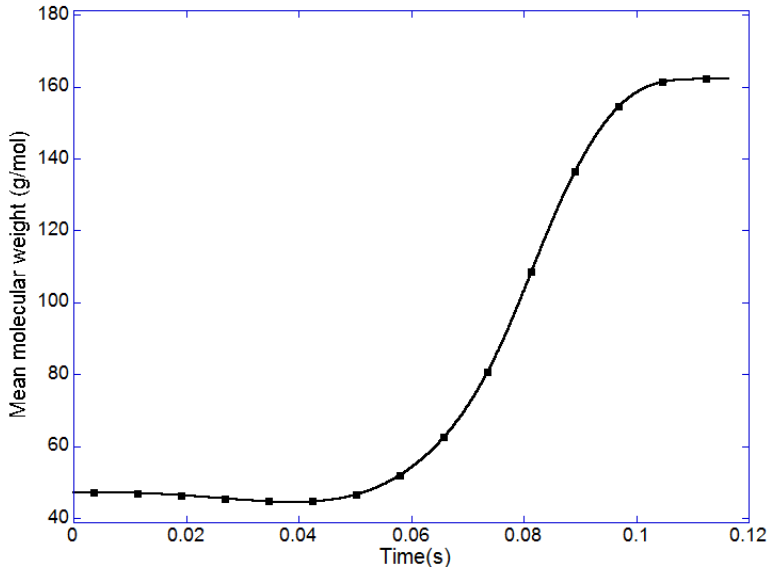

Figure 6.6 History of the mean molecular weight of bio-oil in the liquid phase

It can be seen that hydroxyacetaldehyde, hydroxypropanone, and acetic acid produce the most vapor in the computational domain. Water and propionic acid have much less vapor concentrating in a small region near the spray tip. This observation is in consistence with the histories of vaporization rate fractions as shown in Figure 6.4. Note that Figure 6.7 shows the vapor distributions at the early stage of the spray. Later in the spray vaporization process, less volatile components of bio-oil, such as levoglucosan will produce more vapors, and their vapors will concentrate in a region distant from the injector.

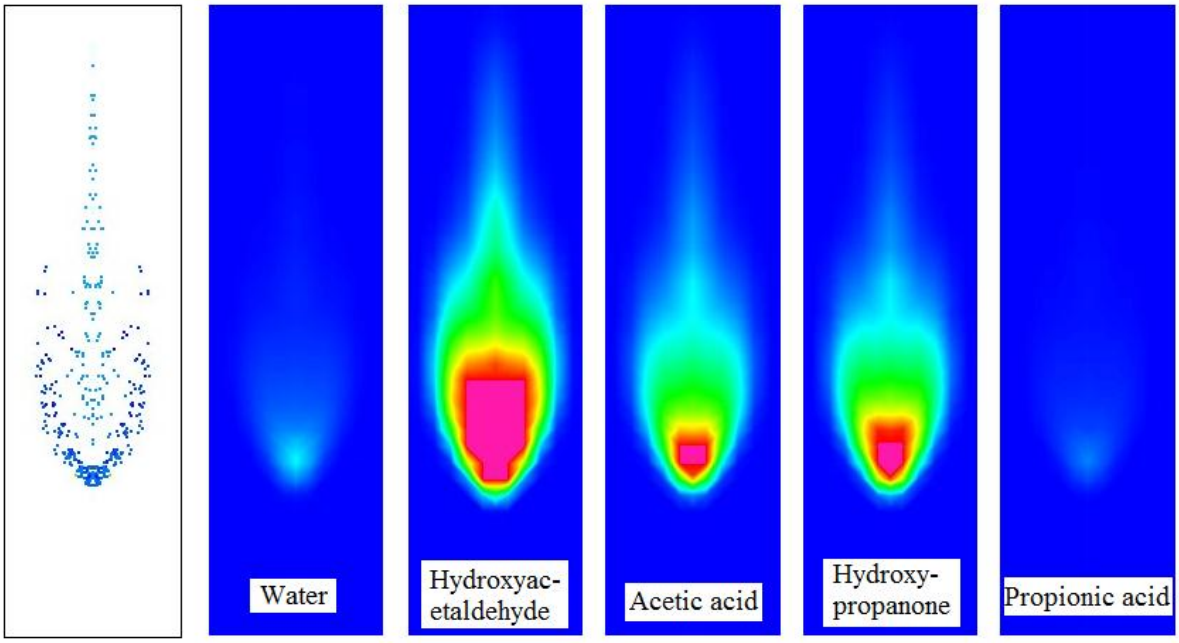

Figure 6.7 Predicted vapor distributions of bio-oil components at 1.4 ms, T_{amb}=900 K, P_{amb}=37.58 bar

Similar to the application of biodiesel, the more practical way of using bio-oil is to blend the fuel with conventional fuels. In this study, the vaporization behavior of the mixture of bio-oil and diesel fuel was first studied. The liquid drop being studied consists of 20% bio-oil and 80% diesel fuel on volume basis and the ambient conditions are 800 K and 1 bar. The vaporization of the drop was simulated and compared with the vaporization histories of pure bio-oil and diesel fuel as shown in Figure 6.8. The vaporization of diesel fuel is modeled using continuous thermodynamics as described in Sec. 3.1. Results show that bio-oil drop has lifetime about three times longer than diesel fuel drop. The volume fraction of bio-oil in the mixture is shown in Figure 6.9. It can be seen that the volume fraction of bio-oil decreases at the beginning (due to the vaporization of its lighter components), increases after about 0.02 seconds (due to the vaporization of light diesel components), and finally decreases sharply to zero (due to vaporization of its remaining components). This peculiar phenomenon is due to the variations of the compositions of both fuels during the vaporization process. Both multicomponent fuels in the blend become less volatile due to the higher concentration of the heavy components. The variation of volume fraction is determined by the relative volatilities of both fuels. Figure 6.10 shows the history of the mean molecular weight of diesel fuel in

the mixture. At the end of the vaporization process, the mean molecular weight of diesel fuel increases sharply making the fuel less volatile than bio-oil components. This is the reason of the sharp drop of bio-oil volume fraction. This phenomenon is the effect of the continuous thermodynamics calculation at the end of vaporization when the drop size is small.

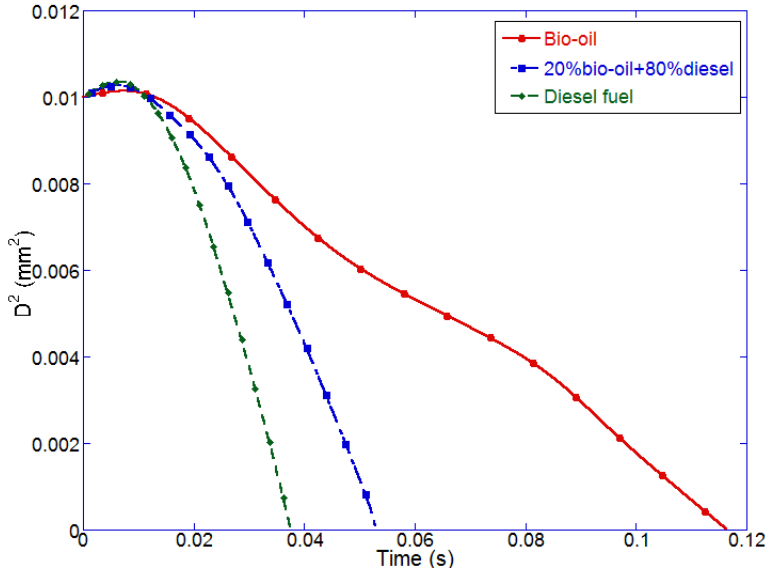

Figure 6.8 Vaporization histories of three different drops

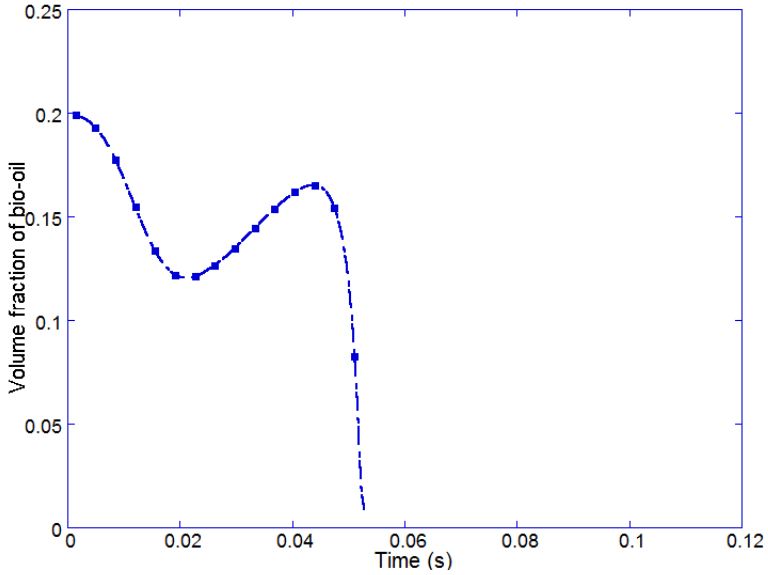

Figure 6.9 History of the volume fraction of bio-oil in the mixture of diesel/bio-oil drop

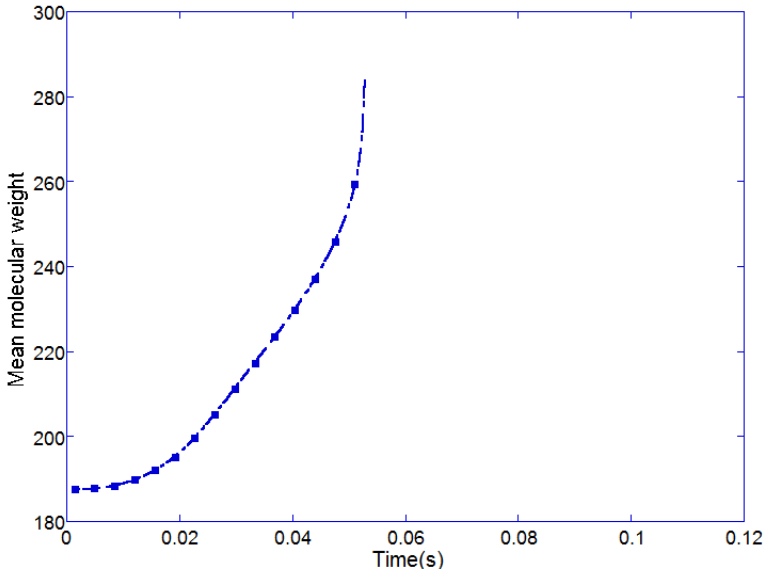

Figure 6.10 History of the mean molecular weight of diesel fuel in the diesel/bio-oil mixture

Bio-oil can also be mixed with ethanol and used in spark ignition engines. In this study, similar to the bio-oil-diesel mixture, bio-oil is blended with ethanol at a volume ratio of 1:4. The vaporization of the fuel mixture at 550K and 1 bar is simulated and compared with the vaporization of bio-oil and ethanol drops at the same ambient conditions. The histories of drop size in Figure 6.11 show that bio-oil has a drop lifetime about 4 times longer than ethanol. The mixture of bio-oil and ethanol shows similar vaporization history with ethanol before 0.1s, and has similar vaporization rate, i.e., the slope of the curve, with the bio-oil drop after 0.1s. Figure 6.12 shows the history of bio-oil volume fraction which keeps increasing in the bio-oil-ethanol mixture. The volume fraction history agrees with the drop size history indicating that only bio-oil components are left after 0.1s.

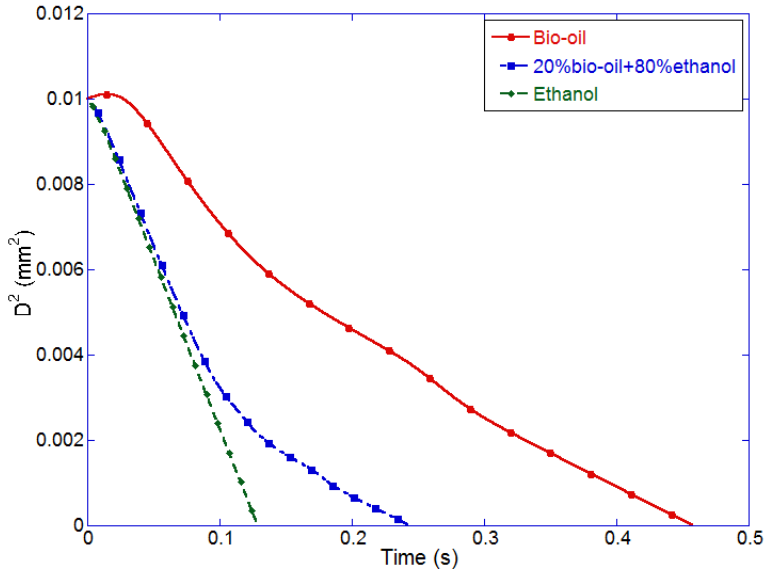

Figure 6.11 Vaporization histories of various bio-oil and ethanol drops

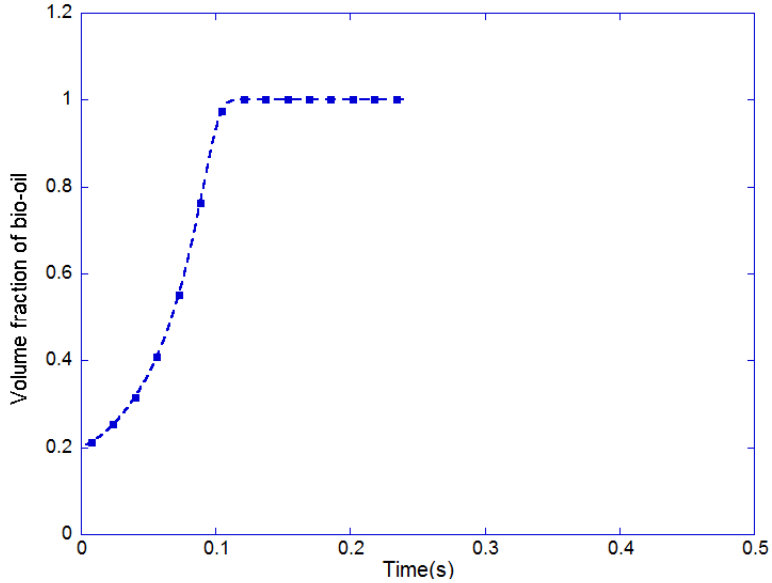

Figure 6.12 History of the volume fraction of bio-oil in the mixture of bio-oil and ethanol

Another practical way of bio-oil application is to blend the fuel with biodiesel. In this study, the vaporization of the mixture of bio-oil and biodiesel at the volume ratio of 1:4 was also simulated. Vaporizations of biodiesel and bio-oil drops were also simulated for comparison. Biodiesel was modeled as the ideal mixture of the five major components using the biodiesel vaporization model described in Sections 3.2 and 4.3. The histories of drop size and bio-oil volume fraction are shown in Figure 6.13 and Figure 6.14, respectively. It can be

seen that even though bio-oil has much longer drop lifetime than biodiesel, the volume fraction of bio-oil keeps decreasing during the entire vaporization process. This is different from the observations in the above two sections. The reason is that most of the components of bio-oil are more volatile than biodiesel and thus vaporize earlier causing the volume fraction of bio-oil to decrease. But the heavy components of bio-oil such as levoglucosan dominate bio-oil at the late stage making the drop life time much longer than biodiesel.

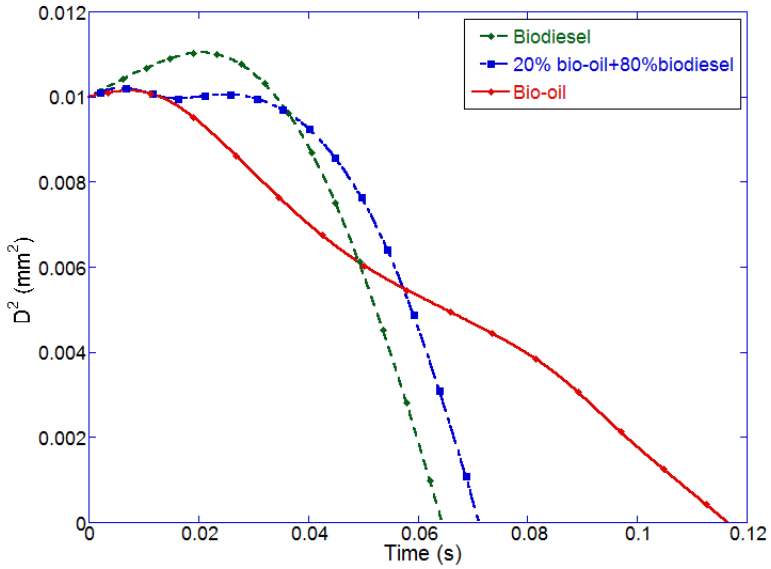

Figure 6.13 Vaporization histories of various bio-oil and diesel drops

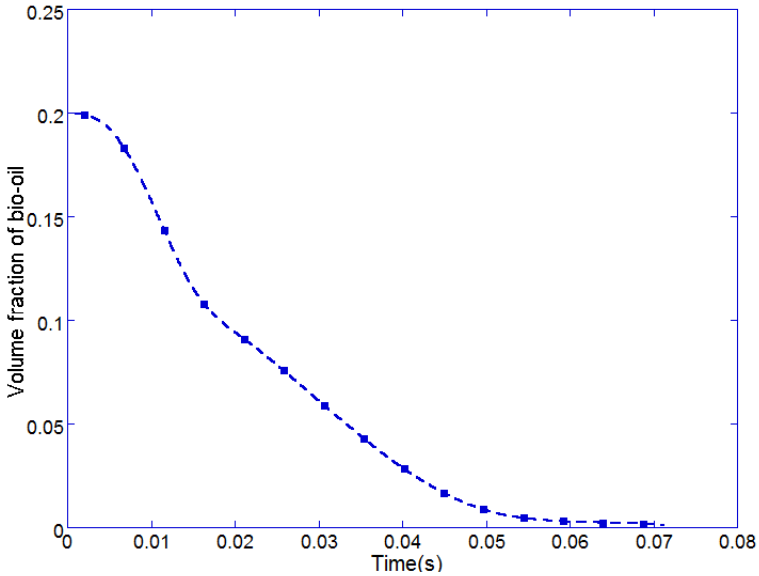

Figure 6.14 History of the volume fraction of bio-oil in the mixture of bio-oil and biodiesel

CHAPTER 7 CONCLUSIONS AND RECOMMENDATIONS

7.1 Conclusions

The present study is focused on the multicomponent drop vaporization modeling using different approaches depending on the compositions of the practical fuels. Continuous thermodynamics approach was applied to model the vaporization of petroleum fuels such as gasoline and diesel fuel which are composed of 200 ~ 300 hydrocarbon species. Gamma distribution, which is a probability distribution function, was used to model the molecular weight distribution of such fuels and therefore consider the multicomponent nature of petroleum fuels. The vaporization of single petroleum fuel drops was simulated, and histories of the drop size reduction and mean molecular weight variation during vaporization were presented. Results show that for both diesel fuel and gasoline drops, the mean molecular weight of the drop continues to increase as soon as the drop vaporization starts and become very high at the end of the vaporization process. The curves of molecular weight distribution continuously shift to the high end due to the earlier vaporization of relatively lighter components and the increasing concentration of heavier components.

Detailed chemistry model was integrated with the continuous thermodynamics vaporization model in KIVA and used for diesel combustion simulation. Predicted flame structures and soot distributions were compared with experimental results, and good levels of agreement were obtained. This good agreement shows that the present multicomponent vaporization model can provide a reasonable prediction of the fuel vapor distribution and can be used to accurately simulate the vaporization process in conditions where fuel component effects are important.

To study the vaporization behavior of petroleum-biofuel blends, which are practical ways of using biofuels in engines, the vaporization of the blends of fuels with distinct physical properties and compositions was modeled. For the blends of petroleum fuels and biofuels, a hybrid approach, which uses continuous thermodynamics for petroleum fuels and discrete components for biofuels, was developed. For diesel-biodiesel blends at various volume ratios, simulation results show that the model predicts an increase in the drop lifetime if there is more biodiesel in the fuel blend. The pure biodiesel drop has a significantly longer

heating time than other blends due to its low vaporization rate. The vaporization rates, i.e., the slope of the D^2 curve, of various fuel blends appear to be similar once the drop reaches a certain high temperature. During the vaporization process, the lighter components of diesel fuel vaporize earlier and therefore the volume fraction of biodiesel increases from the beginning until the late stage of the vaporization process. Biodiesel components do not vaporize until the drops reach a certain high enough temperature. As the vaporization process continues, biodiesel and most of the diesel components have vaporized, and only the heavy components of diesel fuel are left in the drop. Consequently, the volume fraction of biodiesel drops significantly at the end of the drop lifetime.

Vaporization behaviors of gasoline-ethanol drops were also studied using the same hybrid approach. Results indicate that the drop with a higher ethanol concentration will have longer lifetime due to the relatively higher latent heat of ethanol. During the vaporization process, lighter components of gasoline have a higher vaporization rate than ethanol although both fuels in the mixture start to vaporize once the drop is generated, different from diesel-biodiesel drops. As the vaporization continues, ethanol vaporizes at a higher rate than the heavier components of gasoline and the drop will reduce to a pure gasoline drop at the late stage of the vaporization process. A general conclusion can be made from the results of fuel blends at different ratios, namely, E10 and E20 drops can be approximated by a regular gasoline drop, and E85 can be approximated by a pure ethanol drop in terms of drop lifetime and vaporization history. Nonetheless, the details of the vaporization history are slightly different for the fuel blends.

To extend the vaporization simulation of multicomponent fuel drops to engine operating conditions characterized by high pressure and high temperature, Raoult's law, which is the phase equilibrium only true at low-pressure conditions, was replaced by general phase equilibrium in vaporization calculation. The phase equilibrium calculation under high-pressure conditions is based on the equality of fugacity for fuel components and ambient gas species in both phases. For petroleum fuels, continuous thermodynamics was coupled with the high-pressure phase equilibrium by correlating the parameters of Peng-Robinson equation of state and then fugacity coefficient with the molecular weights of the continuously distributed components. Based on gamma distribution, equations for the molecular weight

distribution of the fuel components in the vapor phase at drop surface were derived. In addition, methods of estimating physical properties such as density, diffusivity, and enthalpy of vaporization under high-pressure conditions were also provided.

The present high-pressure multicomponent vaporization model was validated using the experimental data of n-heptane drops at different ambient conditions. The predicted histories of drop size during vaporization agree well with the experimental data. The model was further applied to predict the vaporization of diesel fuel drop under ambient conditions with different temperatures and pressures. Results of the 900 K ambient temperature cases show that the drop lifetime decreases with increasing ambient pressure. However, at the 700 K ambient temperature, the drop lifetime increases with increased ambient pressure, opposite to the observation from the 900 K cases. This phenomenon reveals that the effect of ambient pressure on the drop lifetime can be dependent on ambient temperature. It is also found that two competing factors, namely, reduced mass transfer number (decreasing vaporization rate) and reduced enthalpy of vaporization (increasing drop heating rate) at higher pressure conditions determines the way in which the drop lifetime changes with ambient pressure. In any case, model results show that the mean molecular weight of the vapor is smaller than that of the liquid and both mean molecular weights keep increasing during the process, indicating that lighter components vaporize earlier than heavier components.

Moreover, the vaporization behaviors of biodiesel and its mixture with diesel fuel under high-pressure conditions were also studied. Biodiesel was modeled as the mixture of five dominant components with compositions determined by the feedstock. The parameters of Peng-Robinson equation of state for biodiesel were obtained using the mixing rule based on the mole fractions of its five components. Vaporization results of biodiesel drops show a similar trend with diesel fuel drops in the variation of drop lifetime with increasing ambient pressure. Vaporization of the fuel mixture spray was also simulated, and results show that at certain point in time, the vapor of biodiesel only concentrates in a small region near the tip of the spray, while diesel fuel vapor exists in a much wider region around the entire liquid spray.

The vaporization of bio-oil, which is an emerging biofuel in engines, was also simulated. In this study, bio-oil was modeled as the mixture of ten major components based on an

analysis of the compositions of bio-oil produced from different resources. A discrete component approach was used to model the vaporization of bio-oil based on the major components selected. The critical properties of the bio-oil components are estimated with normal boiling point according to the atom group contribution methods. Using the estimated critical properties, the physical properties required for vaporization calculation were also estimated using available correlations. The model was used to simulate the vaporization of bio-oil and its mixtures with different practical fuels. Vaporization results of the bio-oil drop show a continuous variation of the volume fractions of the components of bio-oil during the vaporization process. Levoglucosan is the least volatile component and its volume fraction increases monotonically to unity during the vaporization. The volume fractions of other components increase at the beginning and finally decrease to zero during the vaporization process. In addition, bio-oil can also be mixed with diesel fuel, biodiesel, and ethanol in practical applications. Vaporization modeling results of the mixtures show that bio-oil drops have much longer drop lifetime than other fuels or its mixtures with other fuels. The variation of bio-oil volume fraction in the fuel mixture is determined by the relative volatilities of the other fuel compared with bio-oil.

7.2 Recommendations

The present study is focused on the vaporization modeling in multidimensional engine simulation using KIVA code. In addition to accuracy, computational efficiency and stability should be taken into account as well. Therefore, pseudo-steady solution of the species equation in the vapor phase was used in this study. However, to perform a more detailed analysis on drop vaporization especially under high-pressure conditions, the transient governing equations shown in Sec. 2.1 can be solved numerically with the general phase equilibrium as the boundary conditions. Computational meshes can be generated in both the liquid and vapor phases, and the grid should be able to move according to the reducing drop size during vaporization.

One of the advantages of the multicomponent vaporization models is to produce the distributions of the fuel component vapors in the computational domain. Multicomponent models have the potential to improve the engine simulation accuracy by integrating with

detailed chemical kinetics to simulate the combustion of the fuel components. Research in integrating multicomponent vaporization modeling with combustion simulation using detained chemistry is recommended for the future study.

On the other hand, micro-explosion may happen during the vaporization of bio-oil drops due to the high water content. If the drop is heated to a temperature higher than the normal boiling point of water, nucleation and gasification may happen inside the drop and generate gas bubbles. The bubbles may have increasing size due to the continuous ambient heating and finally break up the drop. Therefore, micro-explosion can break up a large drop into smaller drops and be beneficial for the subsequent vaporization. Therefore, research on the micro-explosion phenomenon is interesting and can help better understand the bio-oil spray behaviors in an engine combustion chamber.

BIBLIOGRAPHY

Abraham, J., Magi, V., 1998. A Model for Multicomponent Droplet Vaporization in Sprays. SAE Technical Paper, No. 980511.

Agarwal, A. K., Das, L. M., 2001. Biodiesel Development and Characterization for Use as a Fuel in Compression Ignition Engines. Journal of Engineering for Gas Turbines and Power, 123: 440-447.

Aggarwal, S. K., Mongia, H. C., 2002. Multicomponent and High-Pressure Effects on Droplet Vaporization, ASME Journal of Engineering for Gas Turbines and Power, 124:248-255.

Amsden, A. A., 1999. KIVA-3V, Release 2 Improvements to KIVA-3, LAMS Report.

Arias-Zugasti, M., Rosner, D. E., 2003. Multicomponent Fuel Droplet Vaporization and Combustion Using Spectral Theory for a Continuous Mixture. Combustion and Flame, 135: 271-284.

Barata, J., 2008. Modelling of Biofuel Droplets Dispersion and Evaporation. Renewable Energy, 33: 769-779.

Branca, C., Giudicianni, P., Di Blasi, C., 2003. GC/MS Characterization of Liquids Generated from Low-Temperature Pyrolysis of Wood. Industrial & Engineering Chemistry Research, 42: 3190-3202.

Brenn, G., 2005. Concentration Fields in Evaporating Droplets. International Journal of Heat and Mass Transfer, 48: 395-402.

Chiaramonti, D., Oasmaa, A., and Solantausta, Y., 2007. Power Generation Using Fast Pyrolysis Liquids from Biomass. Renewable and Sustainable Energy Reviews, 46: 177-188.

Chio, C. Y., Bower, G. R., Reitz, R. D., 1997. Effect of Biodiesel Blended Fuels and Multiple Injections. SAE Technical Paper, No. 970218.

Cooper F., 1977. Heat Transfer from a Sphere to an Infinite Medium. International Journal of Heat and Mass Transfer, 20: 991-993.

Curtis, E. W., Farrell, P. V., 1992. A Numerical Study of High-Pressure Droplet Vaporization. Combustion and Flame, 90: 85-102.

Cussler, E. L., 1997. Diffusion Mass Transfer in Fluid Systems 2nd Edition, Cambridge University Press.

Czernik, S., Bridgwater, A. V., 2004. Overview of Applications of Biomass Fast Pyrolysis Oil. Energy & Fuels, 18: 590-598.

Dec. J. E., 1997. A Conceptual Model of DI Diesel Combustion Based on Laser Sheet Imaging. SAE Technical Paper, No. 970873.

Evans, R. J., Milne, T. A., 1987. Molecular Characterization of the Pyrolysis of Biomass. 1. Fundamentals. Energy & Fuels, 1: 123-137.

Flynn, P.F., Durrett, R.P., Hunter, G.L., Zur Loye, A, Akinyemi, O.C., Dec, J.E., Westbrook, C.K., 1999. Diesel Combustion: An Integrated View Combining Laser Diagnostics, Chemical Kinetics, and Empirical Validation. SAE Technical Paper, No. 1999-01-0509.

Gökalp, I., Chauveau, C., Berrekam, H., Ramos-Arroyo, N., 1994. Vaporization of Miscible Binary Fuel Droplets under Laminar and Turbulent Convective Conditions. Atomization and Spray, 4: 661-676.

Goos, A. W., 1954. In Wise, L. E., Jahn, E. C., editors, Wood Chemistry, 2nd Edition. Washington, DC: ACS Monograph 97, American Chemical Society; 2: 826.

Hallett, W., 2000. A Simple Model for the Vaporization of Droplets with Large Numbers of Components. Combustion and Flame, 121: 334-344.

Harstad, K. G., Bellan, J., 2004. Modeling Evaporation of Jet A, JP-7, and RP-1 Drops at 1 to 15 bars. Combustion and Flame, 137: 163-177.

Hasse, C. and Peters, N., 2004. A Two Mixture Fraction Flamelet Model Applied to Split Injections in a DI Diesel Engine. Proceedings of the Combustion Institute, 30: 2755-2761.

Hsieh, K, Shuen, J., 1991. Droplet Vaporization in High-Pressure Environments I: Near Critical Conditions. Combustion Science and Technology, 76: 111-132.

Jay, D. C., Rantanen, O. A., Sipila, K. H., Nylund, N.-O., 1995. Wood Pyrolysis Oil for Diesel Engines. Technical Conference, Milwaukee, Wisconsin.

Jia, H., Gogos, G., 1993. High Pressure Droplet Vaporiation; Effects of Liquid-Phase Gas Solubility. International Journal of Heat and Mass Transfer, 36: 4419-4431.

Kong, S.-C., Kimber, A., 2008. Effects of Biodiesel Blends on the Performance of Large Diesel Engines. SAE Technical Paper, No. 2008-01-1389.

Kong, S.-C., Sun, Y., Reiz, R. D., 2007. Modeling Diesel Spray Flame Liftoff, Sooting Tendency and NOx Emissions Using Detailed Chemistry with Phenomenological Soot Model. Journal of Engineering for Gas Turbine and Power, 129: 245-251.

Lapuerta, M., Armas, O, Rodriguez-Fernandez, J. 2008. Effect of Biodiesel Fuels on Diesel Engine Emissions. Progress in Energy and Combustion Science, 34: 198-223.

Law, C. K., Law, H. K., 1982. A D2-Law for Multicomponent Droplet Vaporization and Combustion. AIAA Journal, 20: 522-527.

Li, Y. and Kong, S.-C. 2008. Diesel Combustion Modelling Using LES Turbulence Model with Detailed Chemistry. Combustion Theory and Modeling, 12: 205-219.

Lippert, A. M., Reitz, R. D., 1997. Modeling of Multicomponent Fuels Using Continuous Distributions with Application to Droplet Evaporation and Sprays. SAE Technical Paper, No. 972882.

McCrady, J. P., Stringer, V. L., Hansen, A. C., Lee, C. F., 2007. Computational Analysis of Biodiesel Combustion in a Low-Temperature Combustion Engine Using Well-Defined Fuel Properties. SAE Technical Paper, 2007-07-0617.

Megaridis, C. M., Sirignano, W. A., 1990. Numerical Modeling of a Vaporization Multicomponent Droplets. Proceedings of the Combustion Institute, 23: 1413-1421.

Mohan, D., Pittman Jr., C. U., Steele, P. H., 2006. Pyrolysis of Wood/Biomass for Bio-oil: A Critical Review. Energy & Fuels, 20: 848-889.

Morin, C., Chauveau, C., Gökalp, I., 2000. Droplet Vaporization Characteristics of Vegetable Oil Derived Biofuels at High Temperatures. Experimental Thermal and Fluid Sciences, 21: 41-50.

Morin, C., Chauveau, C., Gökalp, I., Cathonnet, M., 2004. Vaporization and Oxidation of Liquid Fuel Droplets at High Temperature and High Pressure: Application to N-Alkanes and Vegetable Oil Methyl Esters. Combustion Science and Technology, 176: 499-529.

Musculus, M. P., Dec, J. E., Tree, D. R., 2002. Effects of Fuel Parameters and Diffusion Flame Liftoff on Soot Formation in a Heavy-Duty DI Diesel Engine. SAE Technical Paper, 2002-01-0889.

Nomura, H., Ujjie, Y., Rath, H., Sato, J., Kono, M., 1996. Experimental Study on High-Pressure Droplet Evaporation Using Microgravity Conditions. 26th Symposium (International) on Combustion/The Combustion Institute, 1267-1273.

Osamaa A., Kytö, M., Sipilä K., 2001. Pyrolysis oil combustion tests in an industrial boiler. In: Bridgwater A. V., editor. Progress in thermal chemical biomass conversion, Malden: Blackwell Science Inc, 1468-1481.

Patel, A., Kong, S.-C., Reitz, R. D., 2004. Development and Validation of a Reduced Reaction Mechanism for HCCI Engine Simulations. SAE Technical Paper, No. 2004-01-0558.

Pickett, L. M., Siebers, D. L., 2004. Non-Sooting, Low Flame Temperature Mixing-Controlled DI Diesel Combustion. SAE Technical Paper, No. 2004-01-1399.

Prausnitz, J. M., Lichtenthaler, R. N., Azevedo, E. G., 1986. Molecular Thermodynamics of Fluid-Phase Equilibria, 2nd Edition. Prentice Hall, Inc.

Ra, Y., Reitz, R. D., 2004. A Model for Droplet Vaporization for Use in Gasoline and HCCI Engine Applications. ASME Journal of Engineering for Gas Turbines and Power, 126: 1-7.

Ra, Y., Reitz, R. D., 2009. A Vaporization Model for Discrete Multicomponent Fuel Sprays. International Journal of Multiphase Flow, 35: 101-117.

Ra, Y., Reitz, R. D., McFarlane, J., Daw, C. S., 2007. Effects of Fuel Physical Properties on Diesel Engine Combustion Using Diesel and Bio-diesel Fuels. SAE Technical Paper, No. 2008-01-1379.

Ramadhas, A. S., Muraleedharan, C., Jayaraj, S., 2005. Performance and Emission Evaluation of a Diesel Engine Fueled with Methyl Esters of Rubber Seed Oil. Renewable Energy, 36: 1789-1800.

Ramos, M., Fernandez, C., Casas, A., Rodriguez, L., Perez, A., 2009. Influence of Fatty Acid Composition of Raw Materials on Biodiesel Properties. Bioresource Technology, 100: 261-268.

Reid, R. C., Prausnitz, J. M., Poling, B. E., 1987. The Properties of Gases & Liquids, 4th Edition. McGraw-Hill, Inc.

Sazhin, S. S., 2006. Advanced Models of Fuel Drop Heating and Evaporation. Progress in Energy and Combustion Science, 32: 162-214.

Shaddix, C. R., Tennision, P. J., 1998. Effects of Char Content and Simple Additives on Biomass Pyrolysis Oil Droplet Combustion. Twenty-Seventh Symposium (International) on Combustion/The Combustion Institute, 1907-1914.

Shihadeh, A., Hochgreb, S., 2000. Diesel Engine Combustion of Pyrolysis Oils. Energy & Fuels, 14: 260-274.

Sirignano, W. A., 1999. Fluid Dynamics and Transport of Droplets and Sprays, Cambridge University Press.

Solantausta, Y., Nylynd, N.-O., Westerholm, M., Koljonen, T., Oasmaa, A., 1993. Wood Pyrolysis Liquid as Fuel in a Diesel Power Plant. Bioresource Technology, 46: 177-188.

Solantausta, Y., Nylynd, N.-O., Oasmaa, A., Westerholm, M., Sipila, K., 1995. Preliminary Tests with Wood-Derived Pyrolysis Liquid as Fuel in a Stationary Diesel Engine. Biomass Pyrolysis Liquid Properties and Combustion Meeting, Estes Park, Colorado, USA, 355-361.

Takahashi, S., 1974. Preparation of a Generalized Chart for the Diffusion Coefficients of Gases at High Pressures. Journal of Chemical Engineering of Japan, 6: 417-420.

Tamin, J., Hallett, W. L. H., 1995. A Continuous Thermodynamics Model for Multicomponnet Droplet Vaporization. Chemical Engineering Science, 50: 2933-2942.

Thomson, G. H., Brobst, K. R., Hankison, R. W., 1982. An Improved Correlation for Densities of Compressed Liquids and Liquid Mixtures. AIChE Journal, 28: 671-676.

Tone, A. Y., Sirignano, W. A., 1986. Multicomponent Droplet Vaporization in a High Temperature Gas. Combustion and Flame, 66: 221-235.

Torres, D. J., O'Rouke, P, J, Amsden, A. A., 2003. Efficient Multicomponent Fuel Algorithm. Combustion Theory and Modeling, 7: 67-86.

Wang, D., Lee, C. F., 2005. Continuous Multicomponent Fuel Film Vaporization Model for Multidimensional Engine Modeling. SAE Technical Paper, No. 2005-01-0209.

Wang, D., Lee, C. F., Zeng, Y, 2003. Modeling of Air Fuel Mixing in a Stratified Gasoline Direct Injection Engine Using Multicomponent Fuel Representation. SAE Technical Paper No. 2003-01-0067.

Wornat, M. J., Porter, B. G., Yang, N. Y. C., 1994. Single Droplet Combustion of Biomass Pyrolysis Oils. Energy & Fuels, 8: 1131-1142.

Wu, F., Wang, J., Chen, W., 2009. A Study on Emission Performance of a Diesel Engine Fueled with Five Typical Methyl Ester Biodiesels. Atmospheric Environment, 43: 1481-1485.

Yuan, W., Hansen, A. C., Zhang, Q., 2003. Predicting the Physical Properties of Biodiesel for Combustion Modeling. Transactions of the ASAE, 46: 1487-1493.

Zeng, Y., Lee, C. F., 2000. Multicomponent-Fuel Film-Vaporization Model for Multidimensional Computations. Journal of Propulsion and Power, 16: 964-973.

Zeng, Y., Lee, C. F. Lee, 2002. A Model for Multicomponent Spray Vaporization in a High-Pressure and High-Temperature Environment. Journal of Engineering for Gas Turbines and Power, 124: 717-724.

Zhang, L., Kong, S.-C., 2009. Modeling of Multicomponent Fuel Vaporization and Combustion for Gasoline and Diesel Sprays. Chemical Engineering Science, 64: 3688-3696.

Zhang, L., Kong, S.-C., 2010. Vaporization Modeling of Petroleum-Biofuel Drops using a Hybrid Multicomponent Approach. Combustion and Flame, 157: 2165-2174.

Zhang, L. Kong, S.-C., 2011. High-Pressure Vaporization Modeling of Multi-Component Petroleum-Biofuel Mixtures under Engine Conditions. Combustion and Flame, doi:10.1016/ j.combustflame.2011.01.00.

Zhang, Y. Z., Kung, E. H. and Haworth, D. C., 2004. A PDF Method for Multidimensional Modeling of HCCI Engine Combustion: Effects of Turbulence/Chemistry Interactions on Ignition Timing and Emissions. Proceedings of the Combustion Institute, 30: 2763-2772.

Zhu, G., Aggarwal, S. K., 2000. Transient Supercritical Droplet Evaporation with Emphasis on The Effects of Equation of State. International Journal of Heat and Mass Transfer, 43: 1157-1171.

Zhu, G., Reitz, R. D., 2002. A Model for High-Pressure Vaporization of Droplets of Complex Liquid Mixtures Using Continuous Thermodynamics. International Journal of Heat and Mass Transfer, 45: 495-507.